

TOPICAL REVIEW • OPEN ACCESS

## Progress on nuclear reaction rates affecting the stellar production of $^{26}\text{Al}$

To cite this article: A M Laird *et al* 2023 *J. Phys. G: Nucl. Part. Phys.* **50** 033002








View the [article online](#) for updates and enhancements.

You may also like

- [THE EFFECTS OF THERMONUCLEAR REACTION RATE VARIATIONS ON  \$^{26}\text{Al}\$  PRODUCTION IN MASSIVE STARS: A SENSITIVITY STUDY](#)  
Christian Iliadis, Art Champagne, Alessandro Chieffi *et al.*
- [Gamma-Ray Emission of  \$^{60}\text{Fe}\$  and  \$^{26}\text{Al}\$  Radioactivity in Our Galaxy](#)  
W. Wang, T. Siegert, Z. G. Dai *et al.*
- [COLLATERAL EFFECTS ON SOLAR NEBULA OXYGEN ISOTOPES DUE TO INJECTION OF  \$^{26}\text{Al}\$  BY A NEARBY SUPERNOVA](#)  
Carola I. Ellinger, Patrick A. Young and Steven J. Desch

## Topical Review

# Progress on nuclear reaction rates affecting the stellar production of $^{26}\text{Al}$

A M Laird<sup>1,\*</sup> , M Lugaro<sup>2,3,4</sup>, A Kankainen<sup>5</sup> , P Adsley<sup>6,7</sup> ,  
D W Bardayan<sup>8</sup>, H E Brinkman<sup>2,9</sup>, B Côté<sup>2,3,10,11</sup>,  
C M Deibel<sup>12</sup>, R Diehl<sup>13</sup> , F Hammache<sup>14</sup>,  
J W den Hartogh<sup>2,11</sup>, J José<sup>15</sup>, D Kurtulgil<sup>16</sup>,  
C Lederer-Woods<sup>17</sup>, G Lotay<sup>18</sup>, G Meynet<sup>19</sup>, S Palmerini<sup>20,21</sup>,  
M Pignatari<sup>2,8,11,22</sup>, R Reifarh<sup>16</sup>, N de Séréville<sup>14</sup>,  
A Sieverding<sup>23,24</sup> , R J Stancliffe<sup>11,22,25</sup> ,  
T C L Trueman<sup>2,22</sup>, T Lawson<sup>2,22</sup>, J S Vink<sup>26</sup>,  
C Massimi<sup>27</sup>  and A Mengoni<sup>28</sup>

<sup>1</sup> Department of Physics, University of York, Heslington, York, YO10 5DD, United Kingdom

<sup>2</sup> Konkoly Observatory, Research Centre for Astronomy and Earth Sciences, Eötvös Loránd Research Network (ELKH), Konkoly Thege Miklós út 15-17, H-1121 Budapest, Hungary

<sup>3</sup> ELTE Eötvös Loránd University, Institute of Physics, Budapest 1117, Pázmány Péter sétány 1/A, Hungary

<sup>4</sup> School of Physics and Astronomy, Monash University, VIC 3800, Australia

<sup>5</sup> Department of Physics, University of Jyväskylä, P.O. Box 35 (YFL), FI-40014 University of Jyväskylä, Finland

<sup>6</sup> School of Physics, University of the Witwatersrand, Johannesburg 2050, South Africa

<sup>7</sup> iThemba Laboratory for Accelerator Based Sciences, Somerset West 7129, South Africa

<sup>8</sup> Physics Department, University of Notre Dame, Notre Dame, IN-46556, United States of America

<sup>9</sup> Graduate School of Physics, University of Szeged, Dom tér 9, Szeged, 6720 Hungary

<sup>10</sup> Joint Institute for Nuclear Astrophysics, Center for the Evolution of the Elements, Michigan State University, 640 South Shaw Lane, East Lansing, MI 48824, United States of America

<sup>11</sup> NuGrid Collaboration, [nugridstars.org](http://nugridstars.org)

<sup>12</sup> Department of Physics and Astronomy, Louisiana State University, Baton Rouge, LA 70803, United States of America

<sup>13</sup> Max Planck Institut für extraterrestrische Physik, D-85748 Garching, Germany

<sup>14</sup> Université Paris-Saclay, CNRS/IN2P3, IJCLab, F-91405 Orsay, France

<sup>15</sup> Department of Physics, Technical University of Catalonia (UPC), Barcelona, Spain

<sup>16</sup> Goethe-Universität Frankfurt, D-60323 Frankfurt am Main, Germany

<sup>17</sup> School of Physics and Astronomy, University of Edinburgh, Edinburgh EH9 3FD, United Kingdom

<sup>18</sup> Department of Physics, University of Surrey, Guildford GU2 7XH, United Kingdom

<sup>19</sup> Department of Astronomy, University of Geneva, Switzerland

<sup>20</sup> Department of Physics and Geology, University of Perugia, via A. Pascoli, I-06125 Perugia, Italy

<sup>21</sup> I.N.F.N. sezione di Perugia, via A. Pascoli, I-06125 Perugia, Italy

<sup>22</sup> E. A. Milne Centre for Astrophysics, Department of Physics and Mathematics, University of Hull, HU6 7RX, United Kingdom

<sup>23</sup> School of Physics and Astronomy, University of Minnesota, Minneapolis, MN-55455, United States of America

<sup>24</sup> Physics Division, Oak Ridge National Laboratory, Oak Ridge, TN 37831, United States of America

<sup>25</sup> H. H. Wills Physics Laboratory, University of Bristol, Tyndall Avenue, Bristol BS8 1TL, United Kingdom

<sup>26</sup> Armagh Observatory and Planetarium, College Hill, Armagh BT61 9DG, United Kingdom

<sup>27</sup> Department of Physics and Astronomy—University of Bologna and INFN, Bologna, I-40146, Italy

<sup>28</sup> ENEA Bologna and INFN sezione di Bologna, V.le Berti Pichat, 6 I-40146, Italy

E-mail: [alison.laird@york.ac.uk](mailto:alison.laird@york.ac.uk), [maria.lugaro@csfk.org](mailto:maria.lugaro@csfk.org) and [anu.kankainen@jyu.fi](mailto:anu.kankainen@jyu.fi)

Received 26 November 2021, revised 14 September 2022

Accepted for publication 24 October 2022

Published 28 February 2023



CrossMark

### Abstract

The radioisotope  $^{26}\text{Al}$  is a key observable for nucleosynthesis in the Galaxy and the environment of the early Solar System. To properly interpret the large variety of astronomical and meteoritic data, it is crucial to understand both the nuclear reactions involved in the production of  $^{26}\text{Al}$  in the relevant stellar sites and the physics of such sites. These range from the winds of low- and intermediate-mass asymptotic giant branch stars; to massive and very massive stars, both their Wolf–Rayet winds and their final core-collapse supernovae (CCSN); and the ejecta from novae, the explosions that occur on the surface of a white dwarf accreting material from a stellar companion. Several reactions affect the production of  $^{26}\text{Al}$  in these astrophysical objects, including (but not limited to)  $^{25}\text{Mg}(p, \gamma)^{26}\text{Al}$ ,  $^{26}\text{Al}(p, \gamma)^{27}\text{Si}$ , and  $^{26}\text{Al}(n, p/\alpha)$ . Extensive experimental effort has been spent during recent years to improve our understanding of such key reactions. Here we present a summary of the astrophysical motivation for the study of  $^{26}\text{Al}$ , a review of its production in the different stellar sites, and a timely evaluation of the currently available nuclear data. We also provide recommendations for the nuclear input into stellar models and suggest relevant, future experimental work.

Keywords: nucleosynthesis, radioisotope, nuclear reaction rate

(Some figures may appear in colour only in the online journal)

\* Author to whom correspondence should be addressed.



Original content from this work may be used under the terms of the [Creative Commons Attribution 4.0 licence](https://creativecommons.org/licenses/by/4.0/). Any further distribution of this work must maintain attribution to the author(s) and the title of the work, journal citation and DOI.

## 1. Introduction

The radioactive nucleus  $^{26}\text{Al}^{29}$  has gained significant attention in the past decades within several fields of astronomy and planetary science. Its half-life is 0.717(24) Myr [1], which corresponds to a mean lifetime of 1.035 Myr. This value allows the  $^{26}\text{Al}$  produced in stars and supernovae, to live, on the one hand, long enough to allow us to trace its abundance back to its creation events, on the other hand, short enough to provide us snapshots of the Galaxy at very specific times, such as today and when the Solar System formed, 4.6 Gyr ago [2]. The fact that its decay produces high-energy  $\gamma$  photons at 1.8 MeV ensures that this radioactive process is observationally accessible via the  $\gamma$ -ray spectrometry performed by satellite observatories (section 1.1). Furthermore, the high-energy  $\gamma$  photons emitted by the decay of  $^{26}\text{Al}$  produce a significant amount of heat within rocks that incorporate  $^{26}\text{Al}$  at their formation. This is relevant for the first planetesimals that formed in the early Solar System, and potentially for extrasolar planetary systems (section 1.3). Interestingly, we have the samples and the laboratory tools to be able to detect and measure the abundance of  $^{26}\text{Al}$  both ‘alive’ today in the Galactic interstellar medium, as it was potentially deposited inside Earth samples by nearby stellar sources within the past few Myr (section 1.2 [3]), as well as ‘extinct’, i.e. already fully decayed into  $^{26}\text{Mg}$ . In fact, from the measured  $^{26}\text{Mg}/^{24}\text{Mg}$  ratio and its correlation with the  $^{27}\text{Al}/^{24}\text{Mg}$  ratio inside a mineral sample, we can infer the amount of  $^{26}\text{Al}$  that was initially present in solid samples that formed at the time when the Sun was formed 4.6 Gyr ago (section 1.3). We can even measure the initial abundance of  $^{26}\text{Al}$  in stardust recovered in meteorites and produced around stars and supernovae that exploded before the formation of the Sun, between roughly 5 and 7 Gyr ago (section 1.4).

Due to these rich and far-reaching implications, the production and distribution of  $^{26}\text{Al}$  in the Galaxy has become the topic of many investigations (see, e.g. reviews by [4–6]). At the core of all such investigations are the nuclear reactions that produce and destroy  $^{26}\text{Al}$  inside stellar objects, from giant stars to novae and supernovae. Large uncertainties, for example, in the processes of mixing in stars and supernovae, and transport of radionuclides in the interstellar medium hamper the interpretation of the observational constraints. Nevertheless, we need to produce stellar yields that do not include significant nuclear physics uncertainties. This requirement is timely because models of supernovae, the Galaxy, and molecular clouds are improving rapidly and the description of various physics processes is becoming more detailed than ever. If the stellar yields are systematically incorrect, due to inaccurate reaction rates, then even the most sophisticated stellar and galactic models will provide us with the incorrect answers. Furthermore, in the case of stardust grains (presented in section 1.4), an almost direct signature of nuclear reactions is recorded in the grains and therefore reaction rates are essential to make any meaningful comparison between models and observations (see, e.g. [7]).

The aim of this review is to provide an updated, broad overview of the production and destruction of  $^{26}\text{Al}$  in different stellar objects and of the status of the reactions involved, in order to support stellar modellers with stronger and clearer information about the nuclear physics inputs to include in their calculations. Using stellar yields from these models we can then interpret observational data, either directly (as in the case of stardust grains, section 1.4) or by feeding the yields into models of the Galaxy, of the interstellar medium, and of Giant

<sup>29</sup> All throughout the paper the notation  $^{26}\text{Al}$  indicates the ground state of  $^{26}\text{Al}$ ; when relevant the notations  $^{26}\text{Al}_g$  and  $^{26}\text{Al}_m$  are used, respectively, to refer to the ground and isomeric states, while  $^{26}\text{Al}_t$  refers to the total  $^{26}\text{Al}$ . The focus of this paper is the stellar production and ejection of the ground state of  $^{26}\text{Al}$  only because the half-life of the isomer of 6 s is too short to allow this nucleus to survive and be ejected by any stellar source.

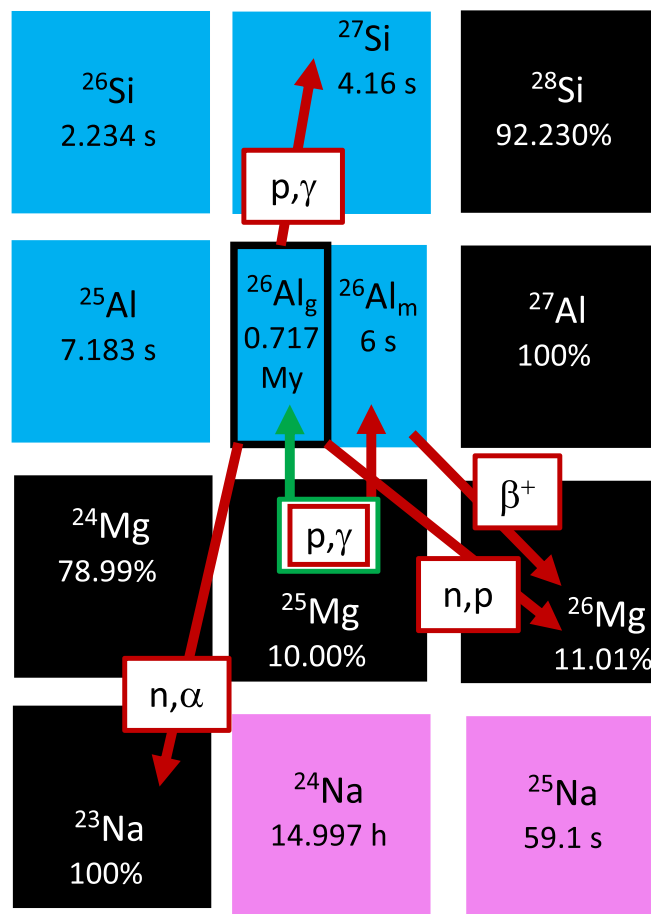


**Figure 1.** Section of the nuclide chart illustrating the main nuclear reactions favouring (green arrow) or inhibiting (red arrows) the production of  $^{26}\text{Al}$  in stellar objects. For clarity, we do not show the decay of the ground state of  $^{26}\text{Al}$  into  $^{26}\text{Mg}$ .

Molecular clouds. These allow us to use the abundance of  $^{26}\text{Al}$  as a tracer to address currently debated topics, from the physics of the interstellar medium to the circumstances of birth of the Sun.

Figure 1 shows the main nuclear reactions that directly affect the production and destruction of  $^{26}\text{Al}$ , which include both proton and neutron captures. These are relevant for most of the astrophysical sites responsible for the production of  $^{26}\text{Al}$  in the Galaxy and will be covered in detail here. There are many more reactions that affect the production and destruction of  $^{26}\text{Al}$  indirectly. For example, neutron source reactions such as the  $^{22}\text{Ne}(\alpha, n)^{25}\text{Mg}$  reaction [8] can affect the destruction of  $^{26}\text{Al}$  via neutron reactions in low-mass (section 2.1) and massive stars (section 2.2.2), while the bypass reaction  $^{25}\text{Al}(p, \gamma)^{26}\text{Si}$  affects the production of  $^{26}\text{Al}$  in novae (see section 2.3). Iliadis *et al* [9] also listed the  $^{25}\text{Mg}(\alpha, n)^{28}\text{Si}$ ,  $^{24}\text{Mg}(n, \gamma)^{25}\text{Mg}$ , and  $^{23}\text{Na}(\alpha, p)^{26}\text{Mg}$  reactions as relevant, some of these will be discussed in section 3.5. In particular, the specific case of nucleosynthesis in core-collapse supernovae (CCSNe) (section 2.2.2) involves several different types of burning episodes and

related reactions. A fully comprehensive analysis needs to be performed within the context of stellar physics uncertainties and is beyond the scope of this work.

In the sections below, we present an overview of the observational opportunities and implications related to  $^{26}\text{Al}$ , from  $\gamma$ -ray observations and Earth samples, to meteoritic stardust, and the early Solar System, and we finish the Introduction with some general considerations about the evolution of  $^{26}\text{Al}$  in the Galaxy. Section 2 describes more specifically the production of  $^{26}\text{Al}$  in different astrophysical sites, from asymptotic giant branch (AGB) stars (i.e. stars with initial masses roughly less than  $10 M_{\odot}$ ), to massive stars (i.e. with initial masses roughly above  $10 M_{\odot}$  and their CCSNe, and novae (i.e. accreting white dwarfs). For further reading on the topic of observations and models we refer to the review from an ISSI workshop series by Diehl *et al* [10]. Section 3 covers the reaction rates responsible for the production and destruction of  $^{26}\text{Al}$  in stars, from those directly involved with  $^{26}\text{Al}$ , to a selection of the most important indirectly related. Section 5 summarises the information presented here and proposes the future work needed to overcome the current major problems and uncertainties in the investigation of the production of  $^{26}\text{Al}$  in stars.

### 1.1. Live $^{26}\text{Al}$ from $\gamma$ -ray observations

The observation of cosmic radioisotopes relies on radioactive decay occurring outside the radioisotope stellar production sites, therefore, they are not distorted from absorption of photons by gas, which occur within the high density stellar matter. Hence, such astronomical data from radioactive decay convey direct information about nuclear reactions within cosmic sites that is otherwise hidden from direct observation (with the exception of neutrinos, which are, however, not observable from distant sites). Commonly available astronomical abundance data from atomic-line spectroscopy are also interpreted in terms of cosmic nucleosynthesis; this is, however, quite indirect information, in particular because the density and ionization state of atoms at the surface of stars is controlled not only by nuclear reactions but also by atomic processes that strongly affect the abundances. Therefore, the characteristic  $\gamma$ -ray lines measured from radioactive decay provide more direct astronomical data. The detection of the characteristic  $\gamma$  rays from  $^{26}\text{Al}$  decay is the first direct, convincing proof that nucleosynthesis is going on within the current Galaxy<sup>30</sup>, because  $^{26}\text{Al}$  has a characteristic decay time of a million years, much shorter than the age of the Galaxy of more than 10 billion years. Therefore,  $^{26}\text{Al}$   $\gamma$  rays can be used to study recent nucleosynthesis sources and the transport of ejected material into the interstellar medium.

Direct observations of  $^{26}\text{Al}$  decay in interstellar space through its characteristic  $\gamma$ -rays with energy 1808.65 keV had been motivated by theorists [12], and was first achieved by the HEAO-C satellite in 1978/1979 observing the central regions of our Milky Way Galaxy [13]. The NASA Compton Gamma-Ray Observatory (1991–2000) with the COMPTEL instrument provided a sky image of the  $^{26}\text{Al}$   $\gamma$ -ray line, which showed a structured  $^{26}\text{Al}$  emission, extended along the plane of the Galaxy [14–16] (figure 2). This image was obtained from measurements taken over years 1991–2000 throughout the sky. It uses a maximum-entropy regularization together with the likelihood of the image's projected data fitting the measurement, and varies the image iteratively until a best image is found to fit the measured events. Such *forward convolution* analysis is required, as the direct inversion of measured data is not possible; the signal of the  $^{26}\text{Al}$  sky is translated into the data space of measured events by the instrument response function, which includes Compton scattering (as a

<sup>30</sup> The detection of the atomic lines of the radioactive elements technetium (Tc) in S-type stars by Merrill [11] represents clear evidence for currently active nucleosynthesis.

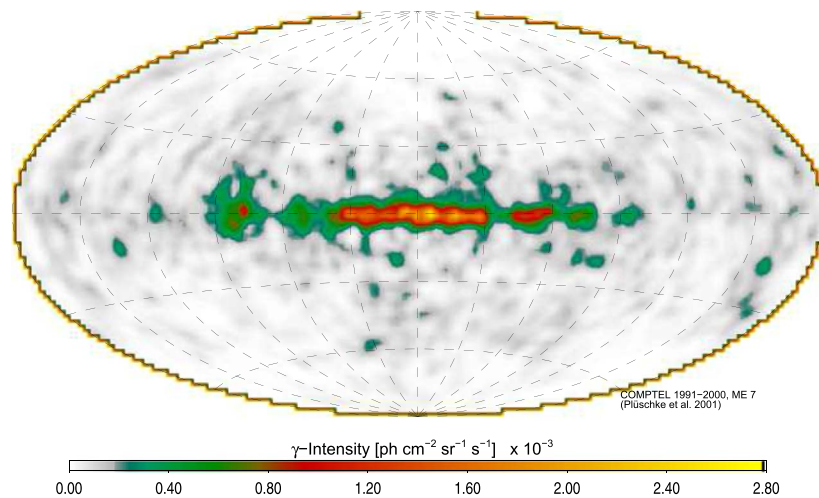


**Figure 2.** The  $^{26}\text{Al}$  sky as imaged with data from the COMPTEL telescope on NASA's Compton Gamma-Ray Observatory [14]. Reproduced with permission from [12].

probabilistic process), and is singular (hence cannot be inverted). The high instrumental background needs careful modelling, and Poissonian statistics must be properly included, hence the maximum-likelihood method is used (see [17, 18] for details on COMPTEL data analysis). The reliability of such  $\gamma$ -ray imaging has been consolidated in many studies (see, e.g. [19]). The  $^{26}\text{Al}$   $\gamma$ -ray image and the structures it showed was found to be in broad agreement with earlier expectations of  $^{26}\text{Al}$  being produced throughout the Galaxy mostly from massive stars and their CCSNe since young stars are typically located on the plane of the Galaxy, and these young stars are preferentially massive.

In 2002, the continuing INTEGRAL mission of the European Space Agency (ESA) started, with its high-resolution  $\gamma$ -ray spectrometer SPI, deepening the astronomical harvests of  $^{26}\text{Al}$  emission (figure 3). Note that the COMPTEL scintillation detectors had an instrumental resolution of  $\sim 200$  keV, compared to  $\sim 3$  keV for the SPI Ge detectors. This led to deeper, Galaxy-wide investigations of  $^{26}\text{Al}$  [20], as recently reviewed [21]. Furthermore, INTEGRAL allowed to spatially resolve specific and well-constrained massive star groups (OB associations), and therefore to test our understanding of massive star groups and how they shape the star-forming interstellar medium (see [22] for a review of astrophysical issues and lessons). Important herein are the Cygnus, the Orion [23] and the Scorpius–Centaurus [24] stellar groups. Altogether, astronomical  $^{26}\text{Al}$  observations have led to both the tracing of the path of nucleosynthesis ejecta after they leave their sources and eventually end up in next generation stars, and the investigation of the cosmic production sites, i.e. stars and supernovae. For the latter objective, it is essential to have the best-possible knowledge of the physics of the stellar sites and of the nuclear reactions involving  $^{26}\text{Al}$ , as discussed here.

### 1.2. Live $^{26}\text{Al}$ in terrestrial archives

Ice cores, deep-sea sediments, and deep-sea FeMn crust material are favourable locations to search for live radionuclides on Earth produced by nearby (in time and space) stellar nucleosynthetic events. These materials have very low growth rates, of the order of mm to cm per thousands to millions of years, and therefore they can provide time-resolved information over time scales of million years. However, because the number of radioactive atoms to be

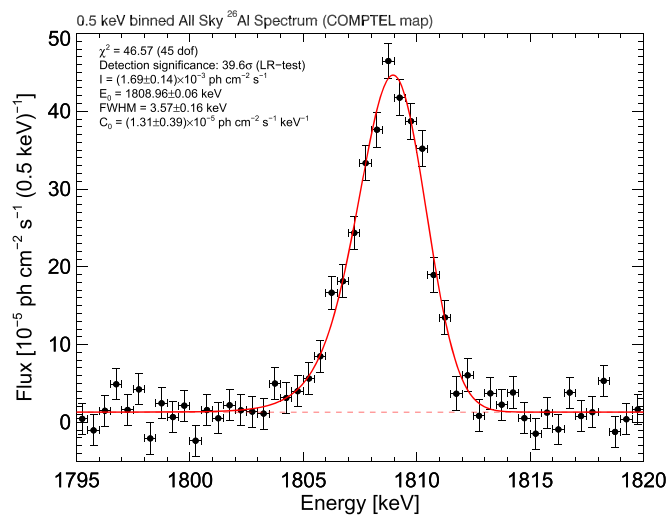


**Figure 3.** The  $^{26}\text{Al}$  line as seen with INTEGRAL high-resolution spectrometer SPI integrated on 13 years of measurements [25]. Reproduced with permission from [20].

counted is tiny (e.g.  $^{26}\text{Al}$  is typically 12 to 16 orders-of-magnitude lower in abundance than the stable terrestrial  $^{27}\text{Al}$ ), only accelerator mass spectrometry (AMS) [3] has so far reached the sensitivity required for such studies. AMS directly counts the radionuclide of interest one by one by means of a particle detector after the sample material is dissolved and the radionuclide of interest is chemically separated from the bulk material. Thanks to this methodology it has been possible to detect on Earth  $^{60}\text{Fe}$  from one or several nearby CCSNe that occurred roughly 2–8 Myr ago [26–28], where  $^{60}\text{Fe}$  is another radioisotope with a half-life  $T_{1/2} = 2.62$  Myr produced by massive stars and their supernovae, also observable via  $\gamma$ -ray satellites [29].

Detection of  $^{60}\text{Fe}$  of stellar origin is possible because its terrestrial production is negligible. In contrast,  $^{26}\text{Al}$  is produced not only in stars but also in the terrestrial atmosphere through cosmic-ray induced nuclear spallation reactions on abundant stable isotopes, such as  $^{27}\text{Al}(p, p-n)$ ,  $^{26}\text{Mg}(p, n)$ ,  $^{28}\text{Si}(p, ^3\text{He})$ , and  $^{24}\text{Mg}(^3\text{He}, p)$ . Furthermore, production inside the terrestrial archives themselves and influx of interplanetary dust grains may add spurious amounts of cosmic-ray produced  $^{26}\text{Al}$ . Stellar  $^{26}\text{Al}$  may be of the order of only a few percent, up to roughly 10%, relative to its terrestrial component [3]. Therefore, to identify a stellar  $^{26}\text{Al}$  signal above the terrestrial background requires an extremely sensitive and efficient detection technique. Feige *et al* [3] searched for presence of stellar  $^{26}\text{Al}$  in an extensive set of deep-sea sediment samples that covered a time-period between 1.7 and 3.2 Myr ago and found an exponential decline of  $^{26}\text{Al}$  with the age of the samples that can be explained by radioactive decay of terrestrial  $^{26}\text{Al}$ . This indicates no significant  $^{26}\text{Al}$  above the terrestrial signal. Nevertheless, owing to the large number of samples analyzed, these data allowed the deduction of an upper limit for the stellar  $^{26}\text{Al}$ .

This upper limit is crucial when taken together with the previously derived stellar  $^{60}\text{Fe}$ , as the live  $^{26}\text{Al}$  and  $^{60}\text{Fe}$  radioisotopes found on Earth originated from nucleosynthesis in massive stars and, in particular, constrain models of the nearby CCSN that occurred 2 Myr ago. These are the same sources that dominate both the current abundances of live  $^{26}\text{Al}$  and  $^{60}\text{Fe}$  in the Galaxy and their extinct abundances in the early Solar System—since massive stars are present in star-forming regions (sections 1.1 and 1.3). Therefore, comparison between three different types of constraints can provide us with significant information on



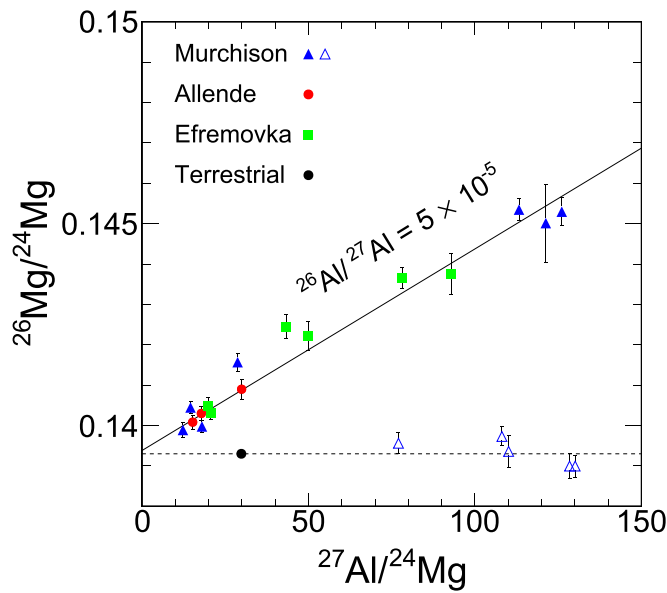


**Figure 4.** Isochrone (solid line) obtained from the pioneering analytical work of [33], and later confirmed by [34]. The slope of this line allowed to obtain for the first time the canonical early Solar System  $^{26}\text{Al}/^{27}\text{Al}$  ratio of  $\approx 5 \times 10^{-5}$  from specific CAI inclusions from different meteorites (Allende, Efremovka, and Murchison, different symbols). The  $^{26}\text{Mg}/^{24}\text{Mg}$  ratio measured in the different minerals that make up the inclusions clearly correlates with the  $^{27}\text{Al}/^{24}\text{Mg}$  ratio of each mineral. This proves that the excess  $^{26}\text{Mg}$  was built inside each mineral from the  $^{26}\text{Al}$  decay after, rather than before, the mineral formed. In the same words of the title of [33]:  $^{26}\text{Al}$  is a ‘fuel’ and not a ‘fossil’ in the early Solar System, i.e. it was present ‘live’, not already decayed. Note that there are also some samples that show no evidence of  $^{26}\text{Al}$  instead (open symbols). Data from [35], and references therein.

both massive star nucleosynthesis and the environment of the formation of the the Sun. The Earth samples produced a lower limit  $^{60}\text{Fe}/^{26}\text{Al}$  between 0.1 and 0.33, which is close to the value obtained from Galaxy-wide gamma-ray spectrometry with INTEGRAL of 0.2–0.4 [29]. However, it is well above the  $^{60}\text{Fe}/^{26}\text{Al}$  ratio derived for the early Solar System of 0.002. This calls for a different origin of  $^{26}\text{Al}$  in the early Solar System, relative to the current live  $^{26}\text{Al}$  in the Galaxy and in Earth archives. The problem is further compounded by theoretical CCSN yields, which currently overproduce  $^{60}\text{Fe}$  relative to  $^{26}\text{Al}$ , even compared to the spectroscopic  $\gamma$ -ray observations [30–32].

### 1.3. Extinct $^{26}\text{Al}$ in the early Solar System

Analysis of the isotopic composition of Mg in Ca–Al-rich inclusions (CAIs) from primitive meteorites, the oldest solid objects to have formed within the Solar System, demonstrates that  $^{26}\text{Al}$  was present in the early Solar System with  $^{26}\text{Al}/^{27}\text{Al} \approx 5 \times 10^{-5}$ . The isochrone method with which this is achieved is explained using figure 4, which presents the first observational evidence of the presence of  $^{26}\text{Al}$ . Several different minerals were analysed within the same sample (of same color in the plot), and for each of these minerals the ratios  $^{27}\text{Al}/^{24}\text{Mg}$  and  $^{26}\text{Mg}/^{24}\text{Mg}$  were measured and plotted against each other as in the figure.  $^{27}\text{Al}$  is the only stable isotope of Al, and  $^{24}\text{Mg}$  the most abundant stable isotope of Mg. Therefore, the

$^{27}\text{Al}/^{24}\text{Mg}$  ratio is a good measure of how much total Al and Mg are present inside each mineral<sup>31</sup>. Because  $^{26}\text{Mg}$  is the daughter nucleus of  $^{26}\text{Al}$ , the  $^{26}\text{Mg}/^{24}\text{Mg}$  ratio can trace the potential initial presence of  $^{26}\text{Al}$ : i.e.  $^{26}\text{Mg}/^{24}\text{Mg} = ^{26}\text{Mg}^*/^{24}\text{Mg} + ^{26}\text{Mg}^{\text{initial}}/^{24}\text{Mg}$ , where  $^{26}\text{Mg}^*$  is the radiogenic abundance from the decay of  $^{26}\text{Al}$ , and  $^{26}\text{Mg}^{\text{initial}}$  its initial abundance in the material from which the mineral comes from, which is a constant. The discovery of the presence of  $^{26}\text{Al}$  is based on the fact that the  $^{26}\text{Mg}/^{24}\text{Mg}$  ratios measured in different types of Mg-rich (i.e. low Al/Mg) and Al-rich (i.e. high Al/Mg) show a linear correlation with Al/Mg. The only way to explain such linear correlation is that the excess of  $^{26}\text{Mg}$  was initially due to an excess of  $^{26}\text{Al}$ . The slope of the line provide us with the initial  $^{26}\text{Al}/^{27}\text{Al}$  ratio, given that the first term in the equation above can be written as  $^{26}\text{Al}/^{27}\text{Al} \times ^{27}\text{Al}/^{24}\text{Mg}$  (figure 4).

The presence of  $^{26}\text{Al}$  in the early Solar System was actually predicted in the 1950s before its discovery, because an early heating source was needed to melt the interiors of the first planetesimals that formed within the first Myr [36]. This heat was driven by the  $\gamma$ -ray photons generated when  $^{26}\text{Al}$  decays to  $^{26}\text{Mg}$  inside a rocky body, the same photons that are observed via the INTEGRAL satellite when  $^{26}\text{Al}$  decays in the interstellar medium (figure 3). One of the consequences of such heat is that the ice inside those planetesimals that formed beyond the ice line (initially made of roughly 50% ice) melted and the water was lost. The timescale of this water loss was shorter than the accretion timescale of planetesimals into terrestrial planets. As sketched in figure 5 from [37], if  $^{26}\text{Al}$  is present in planetesimals, water-poor planets, such as the Earth, which is only a few percent water, result and are known to be habitable world. If  $^{26}\text{Al}$  is not present in significant quantity, instead, water-rich, ocean planets are predicted, which are potentially more difficult to harbour life. Therefore, the presence of  $^{26}\text{Al}$  in star-forming regions can strongly affect the habitability of the planetary systems formed in such regions. Understanding the production of  $^{26}\text{Al}$  in stars is therefore crucial to understand the water context of extrasolar terrestrial planets. However, the origin of  $^{26}\text{Al}$  in the early Solar System is still unclear and strongly debated with several separate stellar origin scenarios proposed<sup>32</sup>, each of which have different probabilities to occur in star-forming regions [6].

For example, Cameron and Truran [39] were the first to propose a simultaneous enrichment plus triggered collapse scenario, in which a nearby CCSN ejects freshly synthesised material into a dense molecular cloud core thereby triggering its collapse to form the solar nebula (see e.g. [40–42]). Alternate mechanisms for the injection of  $^{26}\text{Al}$ -rich material from a CCSN have been proposed, including, for example, pollution of the already formed disk [43–45]. Other scenarios postulate that the gas that later collapsed to form the protosolar molecular cloud was pre-enriched in  $^{26}\text{Al}$  by an earlier generation of massive stars either within the star-forming region or the galactic interstellar medium itself [46–51]. The winds of stars of mass  $> 30 M_{\odot}$  could also produce enough  $^{26}\text{Al}$  to be a candidate source [52, 53]. Brinkman *et al* [54] showed that lower mass stars could also achieve high yields if they are part of a binary system (section 2.2.1). Another possible origin is an AGB star [55], however, this source seems unlikely because these stars cannot produce the required  $^{26}\text{Al}$  abundance without also overproducing several radionuclides heavier than iron [35]. Furthermore, low-mass stars formed in the same molecular cloud as the Sun take a long time to reach the AGB phase ( $\sim 1$  Gyr), by which time the molecular cloud is since long dispersed. Finally, that a

<sup>31</sup> Isotopic ratios of the same elements are not expected to vary significantly even in different types of minerals since both isotopes have similar chemical properties that will keep their ratio constant. This is of course not true for ratios between different elements, such as the  $^{27}\text{Al}/^{24}\text{Mg}$  ratio.

<sup>32</sup> In addition, there is a scenario that hypothesised that  $^{26}\text{Al}$  was produced locally by spallation reactions induced by solar accelerated particles from the young Sun [38].

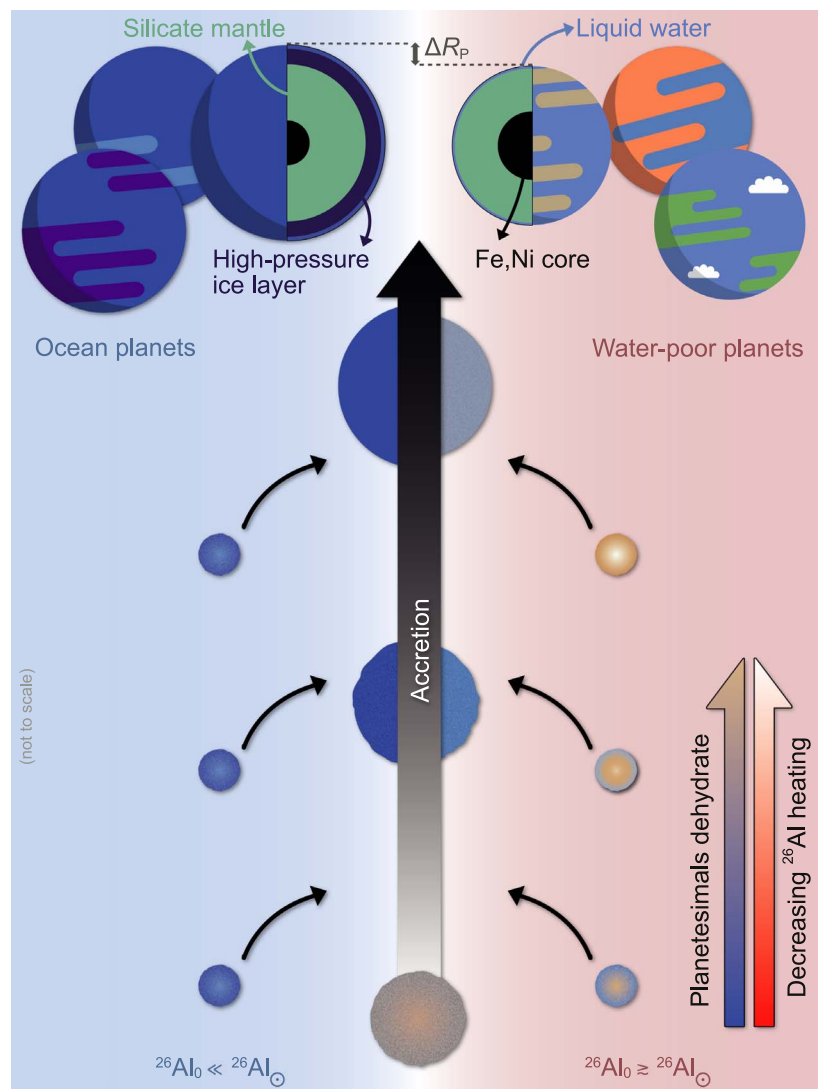


**Figure 5.** Qualitative sketch of the effect of the  $^{26}\text{Al}$  radioactive fuel in the early Solar System, within the framework where water is carried to terrestrial planets from planetesimals that formed beyond the snow line. The left and right sides show the build up of terrestrial planets in potential  $^{26}\text{Al}$ -poor and  $^{26}\text{Al}$ -rich (like the Solar System) planetary systems, respectively. The middle grey arrow indicate the process of the accretion of planetesimal (the first sizable rocks with radius of the order of 50 km) that lead to the formation of rocky planets like the Earth. The blue and red arrows on the bottom right indicate the evolution of the planetesimal water content and of the abundance of live  $^{26}\text{Al}$ , respectively, for the case of  $^{26}\text{Al}$ -rich systems. The difference in the planets radius ( $\Delta R_p$ ) between the two cases indicated at the top of the figure is a measurable quantity for extrasolar planets. Reprinted by permission from Springer Nature: Springer Nature Astronomy, ‘A water budget dichotomy of rocky protoplanets from  $^{26}\text{Al}$ -heating’, Lichtenberg, T; Golabek, GJ; Burn, R; Meyer, MR; Alibert, Y; Gerya, TV; Mordasini, C, 3, 307–313, 2019. Reproduced from [38], with permission from Springer Nature.

molecular cloud would be visited by an AGB star formed elsewhere has been shown observationally to be very unlikely [56].

In summary, investigation of the production of  $^{26}\text{Al}$  by nuclear reactions in massive stars, and its ejection from massive stars, both during the wind phases and the following CCSN explosion, is relevant to understand the evolution and properties of planetesimals and planets both within solar and extrasolar systems.

#### 1.4. Extinct $^{26}\text{Al}$ in stardust grains

Stardust grains are recovered from meteorites and carry the pure signature of the nucleosynthesis that occurred in their parent stars, therefore, they are effectively tiny specks of stars [57, 58]. Evidence that  $^{26}\text{Al}$  was incorporated into stardust grains that formed around stars and supernovae is inferred from the Mg composition of the grains, and in particular from the excess in the daughter nucleus  $^{26}\text{Mg}$ , relative to the other stable Mg isotopes. Most of the grains originated from AGB stars, with some (a few percent) of grains also showing the signature of an origin from CCSNe and novae. Therefore, even if AGB stars and novae are not the major producers of  $^{26}\text{Al}$  in the Galaxy, relative to massive stars, it is necessary to investigate their  $^{26}\text{Al}$  production to interpret the presence of  $^{26}\text{Al}$  in stardust grains, at the time of their formation.

Many recovered and analysed stardust minerals are rich in Al and poor in Mg, so that the signature of  $^{26}\text{Al}$  is evident and measurable. These include silicon carbide (SiC) and graphite, which are carbon (C)-rich grains that form in a gas when  $\text{C} > \text{O}$ , and corundum ( $\text{Al}_2\text{O}_3$ ) and hibonite ( $\text{CaAl}_{12}\text{O}_{19}$ ), which are oxygen (O)-rich grains that form when  $\text{C} < \text{O}$ . If there are only just traces of Mg originally in the grains, then the full initial abundance of  $^{26}\text{Al}$  at the time of the grain formation can be recovered as the whole abundance of  $^{26}\text{Mg}$ . In other words, the abundance of  $^{26}\text{Al}$  is derived directly from the abundance of  $^{26}\text{Mg}$  because Mg is not a main component of the material: the Mg abundance is orders-of-magnitude smaller than that of Al in, e.g. aluminium oxides and silicon carbide grains (see, e.g. figure 2 of [59]), therefore, stable  $^{26}\text{Mg}$  is an orders-of-magnitude less significant contributor to the atoms at mass 26.<sup>33</sup> Gropman *et al* [60] significantly improved the derivation of the initial  $^{26}\text{Al}$  abundance by using the isochrone method for stardust grains as done for Solar System materials (section 1.3). This method produces more accurate results, generally showing higher ratios than previously estimated due to a better estimate of contamination.

Overall, C-rich stardust grains believed to have originated from CCSNe show very high abundances of  $^{26}\text{Al}$ , with inferred  $^{26}\text{Al}/^{27}\text{Al}$  ratios in the range 0.1–1, higher than standard theoretical predictions in the  $\text{C} > \text{O}$  regions of the ejecta. These ratios can be used to constrain the nucleosynthesis models, and they require an extra production mechanism for  $^{26}\text{Al}$  to be at work in the C-rich regions of CCSNe beyond those described in section 2.2.2. This mechanism may be related to ingestion of hydrogen into the He-burning shell and the subsequent explosive nucleosynthesis [62]. The grains that are known to have originated in AGB stars show somewhat lower  $^{26}\text{Al}$  abundances than grains from CCSNe, with  $^{26}\text{Al}/^{27}\text{Al}$  ratios in the range  $10^{-3}$  to  $10^{-2}$ . Also these grains can be used to constrain AGB nucleosynthesis models [7, 63, 64]. For example, oxide grains belonging to a specific group (Group 2) show strong depletion in  $^{18}\text{O}/^{16}\text{O}$  and have also relatively high  $^{26}\text{Al}/^{27}\text{Al}$  ratios. Both features are a product of efficient hydrogen burning, possibly connected to hot bottom burning (HBB) in

<sup>33</sup> Note that in the case of stardust spinel ( $\text{MgAl}_2\text{O}_4$ ), instead, the initial abundance of  $^{26}\text{Al}$  needs to be disentangled from the initial abundance of  $^{26}\text{Mg}$ . This is complicated by the fact that in single stardust spinel grains the proportion of Mg to Al may vary from the stoichiometric value of 1:2, and such variation needs to be taken into account when attempting to derive the initial  $^{26}\text{Al}/^{27}\text{Al}$  ratio [61].

massive AGB stars [7] or extra-mixing in low-mass AGB stars [65] (see section 2.1). Finally, some grains have been potentially interpreted as nova condensates and their relatively high  $^{26}\text{Al}/^{27}\text{Al}$  ratios, up to 0.3–0.5, have been used as one of the main indications of such signature origin [66, 67] (see section 2.3 for more details).

### 1.5. Evolution of $^{26}\text{Al}$ in the Galaxy

The evolution of the average abundance of a radioactive nucleus such as  $^{26}\text{Al}$  in the galactic interstellar medium is generally controlled by the establishment of a steady-state equilibrium between its ejection by stellar sources and its radioactive decay. When such equilibrium is established, the number of  $^{26}\text{Al}$  nuclei  $N_{26}$  no longer changes with time  $t$ :  $dN_{26}/dt = 0$ . The  $dN_{26}/dt = 0$  rate is made of two terms: one is a positive production term given by the stellar production rate per unit time, defined as  $dP_{26}/dt$ ; the other is a negative destruction term, wrought by the decay and equal to  $N_{26} \times \lambda_{26} = N_{26}/\tau_{26}$ , where  $\lambda_{26}$  is the decay rate of  $^{26}\text{Al}$ , and  $\tau_{26}$  its mean lifetime. If the total abundance change is zero, then the two terms are equal and the equilibrium abundance  $N_{26}$  is equal to  $(dP_{26}/dt)\tau_{26}$ . This formula, together with the stellar production rates predicted for the main stellar producers of  $^{26}\text{Al}$  in the Galaxy (see section 2), enables us to quickly compare the predicted  $^{26}\text{Al}$  abundance in the Galaxy to that inferred from  $\gamma$ -ray observations, which represents the sum of the contribution of all nearby young stellar populations currently ejecting this radioisotope.

However, this simple steady-state formula is not enough to interpret the data accurately. Theoretical models must also account for the star formation rate of the Milky Way today; the initial mass function, in order to model stellar populations; and the fact that stellar yields may vary with stellar mass and metallicity, as well as potentially their binary status. Furthermore, stellar enrichment within the interstellar medium is not continuous but represented by events discrete in time and space, therefore, it cannot be accurately described by a continuous  $dP_{26}/dt$  production rate. Local enhancements or reductions in the  $^{26}\text{Al}$  abundance due to spatial and temporal inhomogeneities must also be considered in numerical simulations [68, 69]. This is a challenging task because the evolution of  $^{26}\text{Al}$  depends both on the time interval between the formation of the progenitor star that led to the enrichment event, a parameter that is currently poorly constrained, as well as their spatial distribution. Comparing 3D hydrodynamic simulated distributions of  $^{26}\text{Al}$  to the observed 1.8 MeV emission line flux maps of figure 2 [70, 71] has provided constraints on the Galaxy-wide distribution of  $^{26}\text{Al}$ , and showed that our observer position may be highly biased by the local environment and the stars that populated it. Furthermore, dedicated models [72, 73] are needed when considering specific star-forming regions and the ‘super-bubbles’ generated by the energy from massive stars within them.

Interpreting the abundances of  $^{26}\text{Al}$  derived from meteoritic data also requires the use of chemical evolution models, in this case specifically because the initial  $^{26}\text{Al}$  abundance in the mineral can be measured only relative to that of the stable  $^{27}\text{Al}$ . For the early Solar System, while the abundance of  $^{26}\text{Al}$  reflects the local star formation rate at the time of the formation of the Sun, the abundance of the stable isotope  $^{27}\text{Al}$  encodes the complete past enrichment history of the Galaxy and can only be predicted using galaxy models that properly integrate the galactic star formation history with stellar yields [74–77]. These predictions are, however, affected by many uncertainties such as the total stellar mass formed prior to the formation of the Solar System, the amount of stable  $^{27}\text{Al}$  locked in stellar remnants (white dwarfs, black holes, neutron stars), and large-scale outflows that remove some of the  $^{27}\text{Al}$  content from the Galaxy [76, 77].

All the uncertainties described above can be significantly reduced by considering the  $^{60}\text{Fe}/^{26}\text{Al}$  ratio, since  $^{60}\text{Fe}$  is a radioisotope with a similar half-life (2.62 Myr) and, like  $^{26}\text{Al}$ , can be measured via  $\gamma$ -rays and meteoritic analysis, and is also produced mostly by massive stars. Therefore, its ratio relative to  $^{26}\text{Al}$  solves some of the problems listed above, i.e. a chemical evolution simulation that follows the complete history of the Galaxy is not necessary to give us a direct insight into the stellar sources of these radioisotope. The steady-state equilibrium number ratio of the two radioisotope is  $N_{60}/N_{26} = (dP_{60}/dP_{26})(\tau_{60}/\tau_{26})$ , and the number ratio of the two radioisotope derived from the flux ( $F$ ) ratio observed via  $\gamma$ -rays is  $N_{60}/N_{26} = (F_{60}/F_{26})(\tau_{60}/\tau_{26})$ <sup>34</sup>. Therefore, the  $^{60}\text{Fe}/^{26}\text{Al}$  production ratio in massive stars (by number) can be directly compared to the observed flux ratio [29]. The result is that current models overproduce  $^{60}\text{Fe}$  relative to  $^{26}\text{Al}$  compared to the spectroscopic  $\gamma$ -ray observations by a factor of 3–10 [30–32], and there are inconsistencies not only between models and observations, but also between observations of different types (see end of section 1.2). Moreover, in reality, local inhomogeneities can also affect the  $^{60}\text{Fe}/^{26}\text{Al}$  ratio, even if these two radioisotope came from exactly the same sources, since they decay with different half-lives. Considering temporal heterogeneities within a statistical framework results in an increase of roughly 10% in the  $^{60}\text{Fe}/^{26}\text{Al}$  ratio relative to that calculated using the basic steady-state formula [78], but even larger fluctuations are found in more sophisticated models of the interstellar medium [51] and of giant molecular clouds [79].

Finally, we stress that the fundamental input for any numerical predictions of the evolution of  $^{26}\text{Al}$  in the Galaxy—whether associated with chemical evolution models, interstellar medium simulations, or single-source enrichment models are the adopted stellar yields discussed below and e.g. in [9, 80–83]. In fact, the quantitative predictive capabilities of even the most sophisticated simulations are still limited by the large uncertainties affecting nucleosynthesis and stellar evolution calculations. In the following section, we describe in more detail the production of  $^{26}\text{Al}$  in different types of astronomical objects, from low to high mass stars and binary interaction objects, and the associated uncertainties. Lower mass stars during their AGB phase (section 2.1) are specifically relevant to understand the origin of  $^{26}\text{Al}$  in the majority of meteoritic stardust grains. Massive stars and their CCSNe (section 2.2) are the dominant producers of  $^{26}\text{Al}$  in the Galaxy and in star-forming regions, which are relevant for the early Solar System. Novae are also relevant as potential contributors to galactic  $^{26}\text{Al}$ , as well as sources of rare stardust grains; they will be discussed in section 2.3.

## 2. Stellar production sites

### 2.1. Asymptotic giant branch (AGB) stars: extra-mixing and HBB

Stars with initial mass in the range 1–8  $M_{\odot}$  end their lives as AGB stars. Their structure consists of a degenerate carbon–oxygen core, above which sit a helium-burning shell and a hydrogen-burning shell separated by an He-rich region called the ‘intershell’. Surrounding this central region of the star is an extended, hydrogen-rich, convective envelope. The configuration of thin helium and hydrogen burning shells is unstable, leading to periodic runaway helium-burning episodes, known as thermal pulses. During these thermal pulses, convection mixes the ashes of helium-burning in the intershell region. As a thermal pulse subsides, the star undergoes a structural readjustment that allows the convective envelope to deepen, penetrating the intershell and dragging freshly synthesised material to the surface. This is known as the third dredge-up and it may happen after each thermal pulse. Depending on the

<sup>34</sup> Since the flux corresponds to  $dN/dt$  and the decay equation is  $dN/dt = -N/\tau$ .

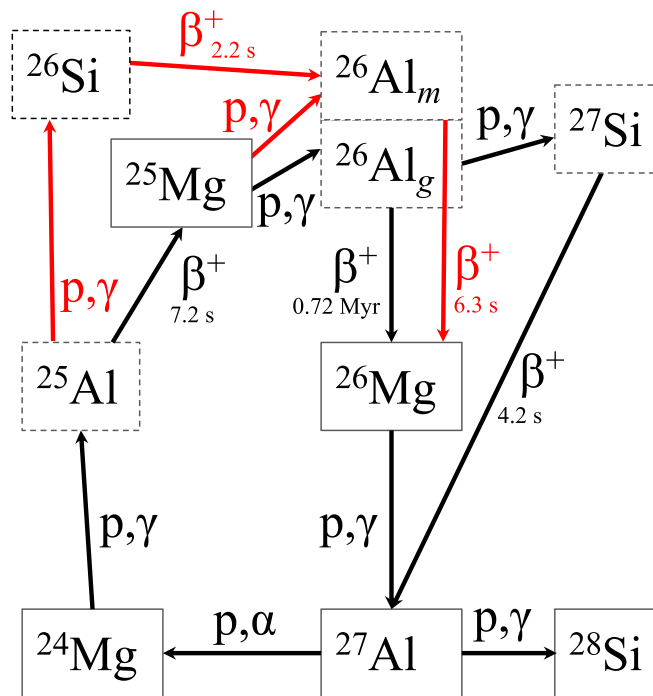


**Figure 6.** Main proton-capture reactions and  $\beta^+$  decays (with half-lives indicated) involved in the MgAl cycles. The solid- and dashed-line boxes represent stable and unstable nuclei, respectively. The red arrows show the reactions and  $\beta^+$  decays that result in the by-passing of the production of the ground state of  $^{26}\text{Al}$ , due to the production of the isomeric state instead. In particular the by-pass via  $^{26}\text{Si}$  can be activated at high temperatures (200–400 MK) during the nova nucleosynthesis described in section 2.3, while the by-pass via  $^{26}\text{Mg}$  is also activated at the relatively low temperatures of AGB stars (from roughly 60 to 100 MK).

strength of the stellar winds (which strip mass from the surface) and the mass of the envelope, an AGB star may undergo a few to many tens of such thermal pulses before the entire envelope is removed and the star transitions to the post-AGB phase. For detailed reviews of AGB stars and their evolution, we refer the reader to Herwig [84] and Karakas and Lattanzio [85].

The production of  $^{26}\text{Al}$  in AGB stars has been studied by many authors [35, 63, 86, 87]. Both the hydrogen-burning and the helium-burning shells are relevant to synthesis of  $^{26}\text{Al}$ . In the latter, the initial abundances of the two heavy magnesium isotopes,  $^{25}\text{Mg}$  and  $^{26}\text{Mg}$ , are enhanced via  $\alpha$ -captures onto  $^{22}\text{Ne}$ , and then dredged-up into the stellar envelope. Directly at the base of the envelope, or in the radiative region just below it, depending on the initial stellar mass, shell hydrogen burning converts  $^{25}\text{Mg}$  into  $^{26}\text{Al}$  via proton captures as part of the Mg–Al chain shown in figure 6.

Above initial masses around  $4 M_{\odot}$ , the exact value depending on the metallicity and the choice of the convective model, the base of the stellar convective envelope is deep enough that it lies within the upper regions of the hydrogen-burning shell. Convection therefore cycles material from the entire envelope of the star through the hydrogen burning shell, in a process referred to as HBB. The combined action of the third dredge-up adding freshly synthesised  $^{25}\text{Mg}$  to the envelope, and the HBB processing this material via the Mg–Al chain

makes massive AGB stars substantial producers of  $^{26}\text{Al}$  [87, 88]. This is in agreement with the high  $^{26}\text{Al}/^{27}\text{Al}$  ratios in Group 2 oxide grains, and make massive AGB stars that experience HBB a candidate source of these grains [7], together with the Cool Bottom Process in low-mass stars are discussed below. The effect of reaction rate uncertainties on HBB in massive AGB stars has been carefully examined by Izzard *et al* (2007) [89], who concluded that uncertainties in the  $^{25}\text{Mg}(p, \gamma)^{26}\text{Al}$  and  $^{26}\text{Al}(p, \gamma)^{27}\text{Si}$  rates lead to an uncertainty in the  $^{26}\text{Al}$  yields from a factor of few at solar metallicity to up to two orders-of-magnitude at lower metallicities. The so-called super-AGB stars also evolve to the AGB but experience carbon burning in the core after the helium-burning has taken place. This results in ONe- rather than CO-rich cores<sup>35</sup>. The initial masses of these stars are in the range 8–10  $M_{\odot}$ , depending on metallicity. In these super-AGB stars the base of the convective envelopes is very hot (up to 100 MK) and therefore HBB is very efficient leading to significant production of  $^{26}\text{Al}$ . Nevertheless, the overall super-AGB contribution to the estimated galactic content of roughly 2.8  $M_{\odot}$  does not exceed 0.3  $M_{\odot}$ , i.e. 10% of the total [90].

In canonical low-mass AGB models, where only convective mixing is taken into account, the hydrogen-burning shell is separated from the convective envelope by a radiative ‘buffer’ region where no mixing occurs. Therefore, the  $^{26}\text{Al}$  produced by H burning in the top layers of the H-burning ashes<sup>36</sup> is ingested inside the thermal pulse, where it can be destroyed by neutron-captures with neutrons generated by the  $^{22}\text{Ne}(\alpha, n)^{25}\text{Mg}$  reaction. What is left is then carried to the stellar surface via the third dredge-up. By this mechanism, the surfaces of low-mass AGB stars are predicted to have  $^{26}\text{Al}/^{27}\text{Al}$  of the order of a few  $10^{-3}$ , in qualitative agreement with those observed in the SiC grains that originated in these stars [63].

The main stellar model uncertainties associated with AGB stars that impact the production of  $^{26}\text{Al}$  are the efficiency of the third dredge-up, the choice of mass-loss rate, and the convective mixing model. The efficiency of the third dredge-up is affected by the method employed to find the convective boundary, e.g. [91]. More efficient third dredge-up in massive AGB stars, for example, carries more  $^{25}\text{Mg}$  from the intershell into the envelope, which is then processed into  $^{26}\text{Al}$  via HBB. The mass-loss rate influences the duration of the AGB phase, with stronger mass loss leading to fewer thermal pulses and less nucleosynthesis [92]. The choice of the convective model affects the temperature structure of the stellar envelope and therefore the temperature at which HBB can take place. More efficient convection leads to higher HBB temperatures, favouring  $^{26}\text{Al}$  production [93, 94]. It can also lead to higher stellar luminosities, which may accelerate mass loss [93].

Another main uncertainty is related to the possible occurrence of non-convective mixing in AGB stars with initial mass below 2–3  $M_{\odot}$ . This mixing may allow the crossing of the radiative buffer region and carry ashes from the hydrogen-burning shell into the convective envelope during the periods in-between thermal pulses (referred to as interpulse periods) and boost the production of  $^{26}\text{Al}$ . Wasserburg *et al* [95] first suggested a non-convective mixing process, which they called Cool Bottom Process (CBP, in contrast to HBB in the most massive stars) as an explanation for some CNO isotope anomalies observed in low-mass AGB stars and stardust grains of AGB origin. In the CBP model, it is assumed that material is carried from the lower edge of the convective envelope down to the innermost layers of the hydrogen shell where it experiences proton-capture reactions and then returns it to the convective zone.

<sup>35</sup> These cores are the progenitor of the ONe white dwarfs onto which accretion results in novae producing  $^{26}\text{Al}$ , see section 2.3.

<sup>36</sup> In the bottom layers of the H-ashes  $^{26}\text{Al}$  is destroyed by neutron-captures, with neutrons generated by the  $^{13}\text{C}(\alpha, n)^{16}\text{O}$  reaction.



The work of [96] showed that the surface of AGB stars with mass  $\leq 2 M_{\odot}$  and close to solar metallicity can be enriched in  $^{26}\text{Al}$  up to  $^{26}\text{Al}/^{27}\text{Al} = 0.1$ . However, they did not provide any hypothesis on the physical mechanism driving the mixing, and treated the depth and the mixing rates as free parameters.

Furthermore, to reach  $^{26}\text{Al}/^{27}\text{Al} = 0.1$  in the stellar envelope the CBP model of the quoted authors must push the carried materials down to the deepest layers of the H-shell, where the temperature is greater than  $5.5 \times 10^7$  K, before returning to the stellar envelope. The so-induced circulation of hot (still burning) matter can strongly affect the stellar energy balance, with relevant luminosity feedback.

In the last two decades many studies have been carried out on non-convective mixing phenomena of low-mass red giants and numerous hypotheses have been formulated on their cause: from stellar rotation [97], to thermohaline mixing [98], and gravity waves [99], stellar magnetic fields [100], and their combined effect [101, 102]. In the case of  $^{26}\text{Al}$  the problem remains that to synthesize this radioisotope in significant amounts via extra-mixing, material must experience relatively high temperatures, and most of the proposed mixing models listed above do not predict  $^{26}\text{Al}$  production. For example, the average molecular weight inversion due to the  $^3\text{He}(^3\text{He}, \text{pp})^4\text{He}$  reaction, which triggers the thermohaline mixing, occurs in the H shell where the temperature is  $\sim 3.5 \times 10^7$  K, too low to efficiently activate the  $^{25}\text{Mg}(p, \gamma)^{26}\text{Al}$  reaction [64, 103]. Only the extra-mixing induced by the effects of the stellar magnetic field proposed in [104] is currently able to produce the  $^{26}\text{Al}/^{27}\text{Al}$  ratios of up to a few  $10^{-1}$  measured in oxide stardust grains of Group 2, also showing strong deficits in  $^{18}\text{O}$ , an isotope efficiently destroyed by H burning [105].

Magnetic-induced mixing in very low-mass ( $\leq 1.5 M_{\odot}$ ) AGB stars can predict high  $^{26}\text{Al}/^{27}\text{Al}$  because it operates via small bubbles of magnetized material, which rise from the H-burning shell to the base of the convective envelope [65], instead of moving material from top to bottom as in the classic CBP model. With state-of-the-art methods, the magnetic extra-mixing predictions of the Al isotopic ratios in low-mass AGB stars do not appear to be significantly affected by reaction rate uncertainties. For example, when using the rates by [106] and [107] for the  $(p, \gamma)$  captures on  $^{25}\text{Mg}$  and  $^{26}\text{Al}^g$ , respectively, instead of those reported by [108] the changes in the resulting  $^{26}\text{Al}/^{27}\text{Al}$  isotopic ratio is smaller than the variations due to the stellar model parameters (such as the stellar mass, the mass loss, and the mixing depth). However, the magnetically induced extra-mixing is relatively fast and the transported material has no time to be affected by proton captures along the path from above the H-burning shell to the envelope (as instead it might happen in the classic CBP). Therefore, any change induced by the mixing in the stellar surface composition reflects the abundances in the H-burning shell. As a consequence any uncertainty or change in the nuclear physics input that affects the  $^{26}\text{Al}/^{27}\text{Al}$  distribution in the shell will also affect the one in the stellar envelope (see the brief analysis by [109]).

## 2.2. Massive star as the main source of $^{26}\text{Al}$ in the Galaxy

From the map of the  $\gamma$ -ray observations from the  $^{26}\text{Al}$  decay (see, e.g. figure 2), it is clear that most  $^{26}\text{Al}$  is confined to the galactic plane and to some specific clumps (see, e.g. figure 16 of [110] and [111–113]). These clumps coincide with known groups of massive stars (i.e. with initial mass  $> 10 M_{\odot}$ <sup>37</sup>), usually referred to as ‘OB associations’, due to the fact that these massive stars are blue/blue-white stars with surface temperatures roughly above 20 000 K

<sup>37</sup> These stars typically end their lives in a CCSN explosion, as opposed to the low- and intermediate-mass stars discussed in the previous section that become AGB stars at the end of their evolution and shed material via stellar winds.

belonging to the spectroscopic O and B classes [114, 115]. The  $^{26}\text{Al}$   $\gamma$ -ray map therefore indicates that most of the  $^{26}\text{Al}$  in our Galaxy is produced by massive stars [19, 116, 117]. Theoretical models in fact predict that massive stars eject large abundances of  $^{26}\text{Al}$ , both through stellar winds and CCSN explosions. Like in most of other stellar sources,  $^{26}\text{Al}$  is mainly made via the  $^{25}\text{Mg}(p, \gamma)^{26}\text{Al}$  reaction, while there are two main destruction channels: proton and neutron capture reactions, depending on the burning phase. Here, we focus first in section 2.2.1 on the winds from both single massive stars and massive stars that have a companion in a close binary system. We also discuss very massive stars (VMS), i.e. with masses above  $100 M_{\odot}$  [118]. Second, in section 2.2.2 we discuss in detail the contribution to  $^{26}\text{Al}$  coming from the CCSN explosive ejecta.

Overall, for stars of masses below roughly  $40 M_{\odot}$ , the contribution of the explosive ejecta is typically dominant relative to that of the winds. For example, when looking at table 3 of Limongi and Chieffi [119], both contributions to  $^{26}\text{Al}$ , from the hydrostatic and explosive phases (see section 2.2.2), are ejected during the explosion. In stars of higher masses, instead the winds are stronger (see section 2.2.1) and therefore their contribution to the total amount ejected increases to become similar to that ejected during the explosion. Neutrino processes are not usually included in the CCSN models, but can contribute a relatively minor component of  $^{26}\text{Al}$ , as we present at the end of section 2.2.2. It should be kept in mind that, as discussed in detail below, these different contributions are strongly model-dependent. Stellar rotation and binarity, mixing in the hydrostatic and explosive phases of the stellar evolution, CCSN properties, such as the mass of the remnant and the energy of the explosion, as well as the choice of the reaction rates can all affect the different contributions to the total  $^{26}\text{Al}$  yield from massive stars of different masses.

*2.2.1. Massive star winds in single and binary systems.* The  $^{26}\text{Al}$  that is expelled from a massive star by winds is produced by hydrogen burning both in the core and, later, in a shell via proton-captures on  $^{25}\text{Mg}$ . This  $^{26}\text{Al}$  can be ejected by stellar winds when layers that once belonged to the H-burning core are exposed at the surface (in the case of Wolf-Rayet (WR) stars) or in the non-WR regime if some mixing mechanism allows the  $^{26}\text{Al}$  produced in H-burning regions to diffuse into the stellar envelope up to the surface. Convection, rotational mixing in the radiative zones of the star and mass losses are key processes that may enrich the surface in  $^{26}\text{Al}$ . For all massive stars, after the main sequence, the convective envelope penetrates into the layers where  $^{26}\text{Al}$  has been produced and transports this radioisotope to the stellar surface. The strong winds following the main sequence expel these layers from the stars, carrying the  $^{26}\text{Al}$  into the surrounding interstellar medium (ISM). For WR stars, the stellar winds already start during hydrogen burning and are so strong that the entire hydrogen-rich envelope is removed, all the way down to the top of the layer processed by the CNO-cycle (also known as the helium core), and this eventually includes the hydrogen-burning shell. The deeper layers exposed this way contain more  $^{26}\text{Al}$ , leading to increased wind yields for these stars. After core hydrogen burning,  $^{26}\text{Al}$  is quickly destroyed in the core during helium-burning by neutron capture reactions, specifically the (n, p) and (n,  $\alpha$ ) channels. However, because the convective helium-burning core is smaller than the original convective hydrogen-burning core, enough  $^{26}\text{Al}$  survives to be expelled from the star into the ISM.

At solar metallicity,  $Z = 0.014$ , all single massive stars above  $30 M_{\odot}$  experience phases of strong mass loss during their lifetimes. The amount of  $^{26}\text{Al}$  ejected by the winds of massive stars, considering the currently recommended mass loss rate prescriptions (see [120] for the hot phase, [121, 122] for the cool phase, and [123] or [124] for the WR phase), depends in a sensitive way on the initial metallicity. At very low metallicity the amount of  $^{26}\text{Al}$  ejected is much smaller than at solar metallicity because the winds are expected to be much weaker, and

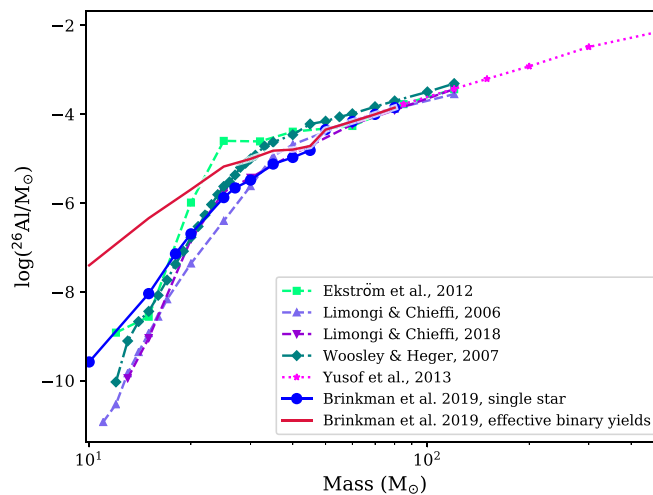


**Figure 7.** The  $^{26}\text{Al}$  yields (in the form of total mass of  $^{26}\text{Al}$  ejected by the winds in units of solar masses) as function of the initial stellar mass from various studies reported in the literature for non-rotating single stars at solar metallicity [81, 125–128]. The red line gives the effective binary yields, i.e. the average increase of the yields of the primary star when considering a flat distribution for the binary periods and non-conservative mass-transfer, which assumes that all the mass transferred to the secondary star is subsequently ejected by the system and therefore results in an upper limit for the yields. The dotted pink line gives the VMS yields deduced from the models by [129] (figure based on figure 3 from [130]).

therefore the mass loss is smaller. Figure 7 shows the  $^{26}\text{Al}$  yields ejected by the stellar winds as a function of initial stellar mass for models of solar metallicity predicted by various studies reported in the literature for non-rotating, solar metallicity stars. The highest yields are for stars with initial masses  $>30\text{--}40 M_{\odot}$ . These stars become the so-called WR stars mentioned before, as they lose their entire hydrogen-rich envelope, exposing their helium cores. During the phase where layers that belonged to the core H-burning phase (which are enriched in helium and nitrogen) are exposed at the surface, large amounts of  $^{26}\text{Al}$  are expelled into the ISM by these stars. Massive stars with masses between 10 and  $30 M_{\odot}$  instead do not lose enough mass to expose the layers that have been processed by CNO burning.

Interestingly, most massive stars are found in binary systems (see e.g. [131]) and are close enough to each other to interact. Sana *et al* (2012) [132] found that more than 50% of all O-type stars (stars with initial masses from  $15 M_{\odot}$  and higher) will interact with their companion during their lifetimes. More than 25% of these stars will interact with their companion even before the end of the main sequence [133]. These interactions influence both the evolution of the stars, and the  $^{26}\text{Al}$  yields [125, 134]. The process resulting from binary interaction that mostly influences the yields is the mass-transfer between the two stars due to Roche lobe overflow. The evolution of the primary (i.e. the initially heavier star of the binary) can be strongly affected by this, as compared to their single-star counterparts. For example, the time at which mass loss starts and the amount of mass lost by the star can be influenced by binary interaction. The main effect of the mass-transfer is that more mass is lost from the primary stars, uncovering the layers rich in  $^{26}\text{Al}$  that otherwise would not be uncovered if the star was evolving in isolation (for more details see [125]). The  $^{26}\text{Al}$  injected into the ISM by binary systems is a combination of the  $^{26}\text{Al}$  present in the layers stripped by mass-transfer and

expelled, and the  $^{26}\text{Al}$  present in the deeper layers of the star that are driven off by the stellar winds (see figures 10 and 11 of [125]). The effect of binary interactions can be seen in figure 7 by comparing the red and the blue lines. The yields of the primary stars increase strongly below  $30\text{--}40 M_{\odot}$ , up to a factor of 100 for the least massive stars ( $10\text{--}15 M_{\odot}$ ). Above  $30\text{--}40 M_{\odot}$ , the binary interactions do not increase the yields of the stars anymore, as the winds are already very efficient in ejecting  $^{26}\text{Al}$ .

Aside from massive star binaries and Wolf-Rayet stars, VMSs can also contribute significantly to the  $^{26}\text{Al}$  enrichment of the ISM. The opinion widely held until 2010 was that the most massive stars in the Universe are of an order of  $100\text{--}150 M_{\odot}$ . More recent studies, however, have found evidence for the existence of VMSs of higher masses [135–137]). These stars are thought to dominate the mechanical energy input and ionising radiation [138, 139] of star-forming regions such as the Tarantula nebula. Moreover, the mass-loss rates of VMSs have been shown theoretically [140] and observationally [136] to be larger than previously assumed via mass-loss rates of Vink *et al* 2001 [122]. The discovered upturn in mass loss for the most massive stars occurs at a transition point where optically thin O-star winds transform to becoming optically thick [140, 141]. Recent population synthesis models [142] including stellar evolution models for VMSs [129, 143] with the new higher mass-loss rates [140] need to be constructed to predict the likely dominant contribution of VMSs to the galactic  $^{26}\text{Al}$  emission budget. We expect such contributions to be high because VMSs are nearly homogeneous stars: their convective core during the main sequence phase extends over more than 90% of the total mass of the star. This means that almost all  $^{25}\text{Mg}$  initially present in the star can be converted into  $^{26}\text{Al}$  via proton captures and the reservoir of matter enriched in newly produced  $^{26}\text{Al}$  may correspond to almost the whole star. Furthermore, VMSs are very luminous and are expected to have strong radiation-driven winds. These two factors lead us to predict large amounts of  $^{26}\text{Al}$  to be ejected from these stars. For example, the non-rotating  $500 M_{\odot}$  model by [129] shown in figure 7 loses about  $450 M_{\odot}$  during the main sequence, leading to an  $^{26}\text{Al}$  yield of  $7.6 \times 10^{-3} M_{\odot}$ . This is a factor 100 more  $^{26}\text{Al}$  than for a  $60 M_{\odot}$  star computed with the same code. Of course, these stars are very rare, however, their yields are so large that even a few events can have a strong impact on the galactic  $^{26}\text{Al}$  budget.

The main uncertainties that affect the production of  $^{26}\text{Al}$  in massive stars are of two types: those involving the nuclear reaction rates, in particular the  $^{25}\text{Mg}(p, \gamma)^{26}\text{Al}$  rate and its branching ratio to the ground state of  $^{26}\text{Al}$ , and the  $^{26}\text{Al}(p, \gamma)^{27}\text{Si}$  rate; and those involving the physics input of the stellar models, including: the size of the convective core, the mass-loss rates, either induced by radiative line driven winds or by mass loss due to mass-transfer episodes in close binaries, and the mixing processes in the radiative zones of the stars, such as turbulence induced mixing due to rotation. An increase either in either the size of the convective core, the mass-loss rates, or the mixing in radiative zones, would lead to an increase of the  $^{26}\text{Al}$  yields. See e.g. the discussion in Palacios *et al* [80].

**2.2.2. CCSN from massive stars, hydrostatic and explosive nucleosynthesis.** Several studies have been dedicated to the production of  $^{26}\text{Al}$  in massive stars including their following CCSN explosions [9, 75, 81, 144]. On the one hand, it is expected and shown by theoretical stellar simulations that the H-burning and C-burning ashes are  $^{26}\text{Al}$ -rich, as compared to the rest of the ejecta because these regions are rich in the protons needed to produce  $^{26}\text{Al}$  (protons are produced during C-burning via the  $^{12}\text{C}(^{12}\text{C}, p)^{23}\text{Na}$  reaction). On the other hand, during He-burning there are no protons available to efficiently produce  $^{26}\text{Al}$ , and if there is any  $^{26}\text{Al}$  already present here, it is typically destroyed by neutron captures, with neutrons produced by the  $^{13}\text{C}(\alpha, n)^{16}\text{O}$  and  $^{22}\text{Ne}(\alpha, n)^{25}\text{Mg}$  reactions. In more advanced stages like explosive O-burning and Si-burning, neither  $^{25}\text{Mg}$  or  $^{26}\text{Al}$  are efficiently produced [75].

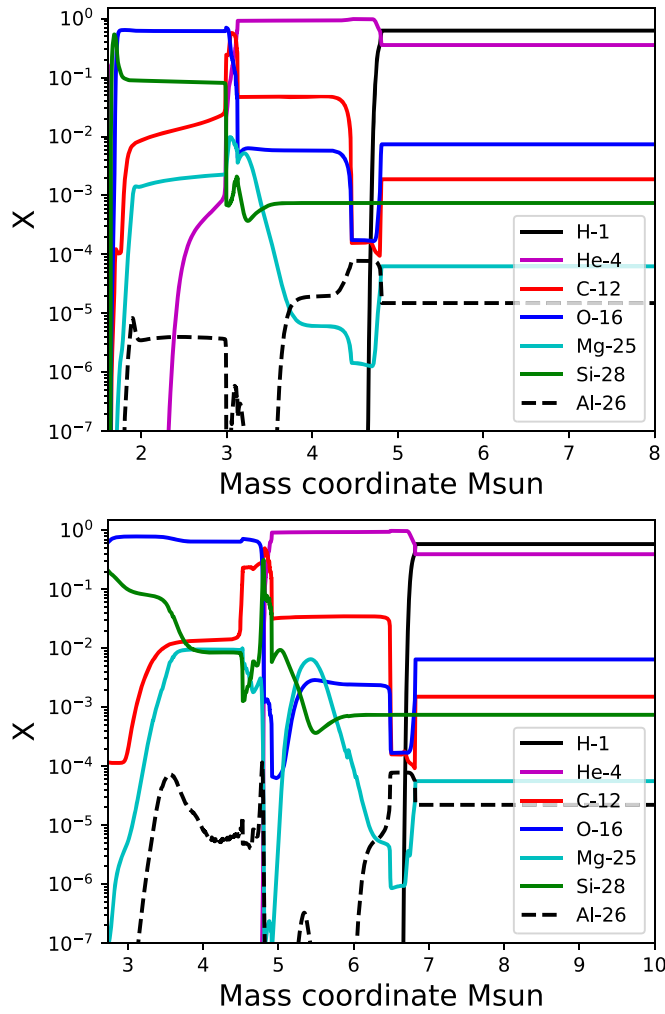


**Figure 8.** Final mass fraction distributions of the isotopes H,  $^4\text{He}$ ,  $^{12}\text{C}$ ,  $^{16}\text{O}$  and  $^{28}\text{Si}$ , indicative of the stellar structure, and of  $^{26}\text{Al}$  and its main seed isotope  $^{25}\text{Mg}$  as function of mass coordinate for the ejecta of CCSN models with initial mass  $M = 15 M_{\odot}$  (top panel) and  $M = 20 M_{\odot}$  (bottom panel) and initial metallicity  $Z = 0.02$  [145].

While these general guidelines are derived from the nuclear astrophysics properties leading to the nucleosynthesis of  $^{26}\text{Al}$ , stellar models show significant variations due to intrinsic properties and simulation parameters. In figure 8 we show the  $^{26}\text{Al}$  mass fraction profile as function of mass coordinate for a  $M = 15 M_{\odot}$  star and a  $M = 20 M_{\odot}$  star model after the explosion [145], together with the profile of other major isotopes indicative of the stellar structure, and of  $^{25}\text{Mg}$ , the seed nucleus for the production of  $^{26}\text{Al}$ . Moving from the outer mass coordinate towards the center of the star, the first  $^{26}\text{Al}$  peak is observed in the H-burning layers for both models, this derives from destruction of most of the initial  $^{25}\text{Mg}$  via proton capture. Just below the H-burning layers, in the upper part of the H-poor, He-rich shell there is a significant amount of  $^{26}\text{Al}$  left from the burning that happened before the CCSN. For the  $15 M_{\odot}$  model, for example, the peak is around a mass fraction of  $2 \times 10^{-5}$ . This peak is due

to either direct mixing of  $^{26}\text{Al}$  from the H-burning region just above, or to mixing of  $^{14}\text{N}$ , which provides protons via the  $^{14}\text{N}(n, p) ^{14}\text{C}$  reaction, using the neutrons produced by  $^{13}\text{C}(\alpha, n)^{16}\text{O}$ . In the  $20 M_{\odot}$  model this peak abundance is much more restricted in mass than in the  $15 M_{\odot}$  model. At the bottom of the He shell, instead,  $^{26}\text{Al}$  is completely destroyed by the neutron captures triggered during the CCSN explosion in this region of the stars (the so-called ‘neutron burst’, or n-process, [146–148]). Further differences between the 15 and the  $20 M_{\odot}$  models are seen in the C-burning ashes. While the  $^{26}\text{Al}$  abundances before the explosion are comparable in the two cases (with a mass fraction of the order of few  $10^{-6}$ ), the  $20 M_{\odot}$  model shows a much stronger explosive production than the  $15 M_{\odot}$  model, visible at a mass coordinate roughly  $3.6 M_{\odot}$ , and comparable to the abundance made by H-burning.

Alternative nucleosynthesis conditions from those described above may also be present and provide a significant contribution to the amount of  $^{26}\text{Al}$  ejected by a CCSN, for instance, these can be related to convective-reactive events during the hydrostatic evolution of the progenitor star. The work of [62] showed that a significant amount of  $^{26}\text{Al}$  can be also produced in the explosive He-burning ejecta, following the ingestion of H in the convective He-shell [149, 150].

Finally, neutrinos from the collapsing stellar core leading to the  $\nu$ -process [151, 152] also affect the production of  $^{26}\text{Al}$  in two ways: directly via the  $^{26}\text{Mg}(\nu_e, e^-)$  reaction, and indirectly by providing additional protons for the  $^{25}\text{Mg}(p, \gamma)$  reaction, mostly from  $^{20}\text{Ne}(\nu_x, \nu_x'/p)$  and spallation from other abundant nuclei. The cross sections for the neutrino-induced reactions are very well constrained [153], in particular, the Gamow–Teller strength for  $^{26}\text{Mg}(\nu_e, e^-)$  has been determined by charge-exchange reactions [154]. The contribution of this process to  $^{26}\text{Al}$ , however, is very sensitive to the rather uncertain neutrino-energy spectrum. Depending on the neutrino energies, the  $\nu$  process may lead to an increase of the  $^{26}\text{Al}$  yields by 10%–40% [75, 153].

### 2.3. Nova outbursts

Classical novae are the stellar explosions that take place in stellar binary systems, consisting of a compact, white dwarf star and a low-mass companion, typically a K or M main sequence star, although observations increasingly reveal more evolved companions. Novae exhibit a sudden rise in optical brightness, with peak luminosity reaching  $10^4$ – $10^5$  solar luminosity. During the explosion, roughly  $10^{-5}$ – $10^{-3} M_{\odot}$  of material is ejected into the interstellar medium, at a speed of several  $10^3 \text{ km s}^{-1}$ . Novae are expected to recur with typical periodicity between 1 and 100 year (recurrent novae) and  $10^4$ – $10^5$  year (classical novae).

The main nuclear reactions involved in the production and destruction of  $^{26}\text{Al}$  in novae, and their associated uncertainties, have been discussed in several papers (e.g. [155, 156]) and are illustrated in figure 6). The synthesis of  $^{26}\text{Al}$  in novae requires the presence of some seed nuclei, such as  $^{24,25}\text{Mg}$ , or to some extent,  $^{23}\text{Na}$ , and  $^{20,22}\text{Ne}$ . Since novae do not achieve high enough temperatures to power CNO-breakout,  $^{26}\text{Al}$  production requires an underlying ONe white dwarf (rather than a CO white dwarf) and some mixing to occur at the interface between the outer layer of the core and the envelope. The main nuclear reaction path leading to  $^{26}\text{Al}$  is  $^{24}\text{Mg}(p, \gamma)^{25}\text{Al}(\beta^+)^{25}\text{Mg}(p, \gamma)^{26g}\text{Al}$ , whereas destruction is dominated by the  $^{26g}\text{Al}(p, \gamma)^{27}\text{Si}$  reaction. The current main source of nuclear uncertainty comes from the rate of the  $^{25}\text{Al}(p, \gamma)^{26}\text{Si}$  reaction: because  $^{26}\text{Si}$  only decays to the isomeric state of  $^{26}\text{Al}$  this reaction determines the fraction of the nuclear path that proceeds through the isomeric  $^{26i}\text{Al}$  state, via the decay of  $^{26}\text{Si}$  thus by-passing  $^{26g}\text{Al}$  synthesis.

Already before the discovery of  $^{26}\text{Al}$  in the interstellar medium by the HEAO-3 satellite through the detection of the 1809 keV  $\gamma$ -ray line [157, 158], Ward [159] suggested that  $^{26}\text{Al}$

could be produced efficiently in astrophysical environments such as classical nova outbursts, characterized by a rapid rise to maximum temperatures around  $T_{\text{peak}} \sim (2-3) \times 10^8$  K, followed by a relatively fast decline. One-zone, explosive H-burning nucleosynthesis studies corroborated this idea (see, e.g. [160, 161]), and concluded that while classical novae might produce sufficient amounts of  $^{26}\text{Al}$  to reproduce some of the observed isotopic anomalies found in meteorites, they would not represent major galactic factories of  $^{26}\text{Al}$ . These calculations, however, assumed solar composition (or CNO-only enhanced) envelopes. With the advent of models of nova explosions on ONeMg white dwarf stars [162], one-zone nova nucleosynthesis models predicted large amounts of radioisotope (such as  $^{22}\text{Na}$  and  $^{26}\text{Al}$ ) in their ejecta [163, 164], suggesting that these novae might represent significant, though still not dominant, sources of the Galactic  $^{26}\text{Al}$ .

The following 1D hydrodynamic simulations [165, 166] stressed the crucial role played by convection in carrying a fraction of the fresh  $^{26}\text{Al}$  synthesized at the base of envelope to the outer, cooler layers where destruction through proton captures could be prevented. Still, the composition adopted for the underlying ONeMg white dwarfs adopted in these models was too crude as it was based on calculations of hydrostatic C-burning nucleosynthesis by Arnett and Truran [167] with mass fraction ratios  $X(^{16}\text{O}):X(^{20}\text{Ne}):X(^{24}\text{Mg})$  of 1.5:2.5:1. Stellar evolution models of intermediate-mass stars [168, 169] revealed that ONe white dwarfs are instead made basically of  $^{16}\text{O}$  and  $^{20}\text{Ne}$ , with above ratios of 10:6:1. The dramatic reduction in the  $^{24}\text{Mg}$  seeds resulted in a significant decrease in the contribution of novae to the galactic  $^{26}\text{Al}$  predicted by the first 1D hydrodynamic simulations from accretion to ejection for a realistic composition of the underlying white dwarf, and with updated nuclear reaction rates [170, 171].

Since the late 1990s, all hydrodynamic 1D nova simulations systematically resulted in some  $^{26}\text{Al}$  production. This includes the most recent *I2321* nova models [172], which include the effect of the inverse energy cascade that characterizes turbulent convection in nova outbursts on the time-dependent amount of mass dredged-up from the outer white dwarf layers, and a time-dependent convective velocity profile throughout the envelope, as computed by 3D simulations [173–175]. While these state-of-the-art models yield more massive envelopes than those previously reported, and result in more violent outbursts characterized by higher peak temperatures and greater ejected masses, their  $^{26}\text{Al}$  yields are similar to previous estimates for ONe novae (see [172] for details).

A crude estimate of the contribution of novae to the amount of  $^{26}\text{Al}$  present in our Galaxy can be obtained from [163, 170]:

$$M(^{26}\text{Al}) \sim \tau(^{26}\text{Al}) f(\text{ONe}) M_{\text{ejec}} X(^{26}\text{Al}) R_{\text{nova}}, \quad (1)$$

where  $M_{\text{ejec}}$  is the mean ejected mass during a nova outburst,  $X(^{26}\text{Al})$  is the mean mass fraction of  $^{26}\text{Al}$  in the ejecta,  $f(\text{ONe})$  is the fraction of ONe novae (typically,  $1/3$ ; see Livio and Truran 1994),  $R_{\text{nova}}$  is the nova rate ( $\sim 50_{-23}^{+31}$  year $^{-1}$  [176]), and  $\tau(^{26}\text{Al})$  is the mean lifetime of  $^{26}\text{Al}$  (1 Myr). From these estimates, and adopting a relatively favorable ONe nova model (e.g.  $M_{\text{ejec}}(^{26}\text{Al}) \sim 2 \times 10^{-8} M_{\odot}$  [171]), we obtain an upper limit to the contribution of novae to the Galactic  $^{26}\text{Al}$  content of  $\leq 0.34 M_{\odot}$ . This corresponds to about 12% of the Galactic  $^{26}\text{Al}$  ( $\sim 2.8 \pm 0.8 M_{\odot}$  [177]) and is in qualitative agreement with the analysis of COMPTEL/CGRO 1.809 MeV  $^{26}\text{Al}$  emission map [177, 178], which favors younger progenitors (i.e. WR stars and CCSN, as discussed in section 2.2). However, it is worth noting that this estimate is affected by large uncertainties, since the mean ejected mass per nova outburst and the variation of the nova rate since the formation of our Galaxy are not well constrained.

### 3. Relevant nuclear reactions

$^{26}\text{Al}$  has two long-living states: the ground state with spin and parity  $J^\pi = 5^+$  and half-life  $T_{1/2} = 0.717(24)$  My, and an isomeric state  $^{26}\text{Al}^m$  at 228 keV with  $J^\pi = 0^+$  and  $T_{1/2} = 6.3460(8)$  s [1]. It is the abundance of the  $^{26}\text{Al}$  ground state that is relevant for the cosmic 1809 keV  $\gamma$ -ray flux. Namely, the  $\beta^+$ -decays from the ground state of  $^{26}\text{Al}$  feed the first excited state in  $^{26}\text{Mg}$ , which de-excites by emitting 1809 keV  $\gamma$ -rays. The isomeric state  $^{26}\text{Al}^m$ , instead, decays via a fast superallowed  $\beta$  decay directly to the  $0^+$  ground state of  $^{26}\text{Mg}$  and hence does not contribute to the cosmic  $\gamma$ -ray flux from  $^{26}\text{Al}$ .

In astrophysical environments (see section 2),  $^{26}\text{Al}$  is mainly produced via radiative proton captures on  $^{25}\text{Mg}$  (see section 3.1). There, de-excitations from the populated states feeding ultimately either the ground or the isomeric state in  $^{26}\text{Al}$  are relevant in order to determine the population ratio between the two states of  $^{26}\text{Al}$ . At lower temperatures, these two states act like separate nuclear species, but at temperatures above 0.4 GK, thermal excitation populating the isomeric state starts to play a role and reduce the effective lifetime of  $^{26}\text{Al}$ , as discussed in section 4. Moreover, at high stellar temperatures and densities, capture of free electrons from the continuum will also affect the lifetime of  $^{26}\text{Al}$  (see section 4). In addition to the production reaction  $^{25}\text{Mg}(p, \gamma)^{26}\text{Al}$ , key reactions to determine the abundance of  $^{26}\text{Al}$  are the destruction p-capture reaction  $^{26}\text{Al}(p, \gamma)^{27}\text{Si}$  (section 3.2), the neutron-induced reactions on  $^{26}\text{Al}$  (see section 3.3) and the bypass route via  $^{26}\text{Si}$  (see section 3.4). Other reactions relevant for the production and destruction of  $^{26}\text{Al}$  are briefly discussed in section 3.5. The reaction network around  $^{26}\text{Al}$  summarizing the relevant nuclear reactions are shown in figures 1 and 6. In summary, in table 7 all the reactions considered here are listed, together with their relevant stellar sites, and corresponding temperatures.

We have recalculated some of the reaction rates presented in the following subsections using the RATESMC code [179] based on the information presented in the tables in each subsection. The resonance energies have been recalculated from the excitation energies, the separation energies and including the corrections for atomic binding as in [180]. Details as to resonance strengths and/or proton widths are provided in each subsection, as needed, together with figures of the new rates. The tabulated data for the rates can be found in tables 8–12.

#### 3.1. The production reaction $^{25}\text{Mg}(p, \gamma)^{26}\text{Al}$

The rate of the  $^{26}\text{Al}$  production reaction is dominated by resonant proton captures to levels above the proton threshold at 6306.33(6) keV [181] in  $^{26}\text{Al}$ . Direct proton captures to bound states in  $^{26}\text{Al}$  and the contribution from the subthreshold ( $3^+$ ) resonance at  $E_{\text{res}} = -24.86(10)$  keV are negligible compared to the resonant captures at temperatures above  $\approx 0.006$  GK [182]. Therefore, we focus here on the resonant proton captures. Table 1 summarises the available data on the excitation energies, spins and parities as well as the resonance energies and strengths for the relevant states in  $^{26}\text{Al}$ . The ground state spin and parity of  $^{25}\text{Mg}$  is  $5/2^+$ , and therefore  $\ell = 0$  proton captures populate states with  $J^\pi = 2^+$  or  $3^+$  in  $^{26}\text{Al}$ ,  $\ell = 1$  proton captures states with  $J^\pi = 1^-, \dots, 4^-$ , and  $\ell = 2$  states with  $J^\pi = 0^+, \dots, 5^+$ . All states, except the  $J^\pi = (7)$  state at 6695 keV, can be populated via  $\ell = 0 - 2$  proton captures, however, many of the spin-parity assignments are still tentative (see table 1) and further studies are needed.

The first studies on excited states above the proton threshold in  $^{26}\text{Al}$  were carried out via  $^{25}\text{Mg}(^3\text{He}, d)$  reactions with the Tandem Van de Graaff accelerator at the University of Pennsylvania in late 1970s [196]. Several states were discovered and angular momenta assigned for the proton transfers based on the angular distribution of the cross sections and distorted-wave Born approximation analysis. Champagne *et al* did a thorough investigation of the  $^{25}\text{Mg}(^3\text{He}, d)$  reaction at the Wright Nuclear Structure Laboratory MP Tandem Van de Graaff accelerator in



**Table 1.** Excitation energies ( $E_x$ ) together with the spins and parities ( $J^\pi$ ) for the excited states above the proton separation energy ( $S_p = 6306.33(6)$  keV [181]) in  $^{26}\text{Al}$ . The excitation energies, spins and parities are from [1] unless stated otherwise. The resonance energies have been recomputed from the excitation energies include a correction for atomic binding of  $\Delta B_e = -1.14$  keV. The resonance energies ( $E_{res}$ ), and experimentally determined resonance strengths  $\omega\gamma$  for the relevant states are given. The resonance strengths are the total resonance strengths—the  $f_0$  factors are the branching of the resonance to the ground state of  $^{26}\text{Al}$ . The  $f_0$  has been recomputed [183] from the listed values in the ENSDF repository including the full cascade to the ground state and the isomer. Only states up to  $E_x = 6800$  keV are listed.

$E_x$ (keV)	$J^\pi$	$E_{res}$ (keV)	$\omega\gamma$ (eV)	$f^a$
6280.33(9)	(3 <sup>+</sup> )	-24.85(11)	$\theta_p^2 = 0.0127(26)^0$	0.770(3)
6343.46(8)	4 <sup>+</sup> [184]	38.29(10)	$4.9(21) \times 10^{-22b}$ [184]	0.79(5)
6363.99(8)	3 <sup>+</sup>	58.81(10)	$2.9(5) \times 10^{-13}$ [185]	0.81(5)
6398.64(21)	2 <sup>-</sup> [186]	93.46(22)	$3.5(4) \times 10^{-10}$ [187, 188]	0.67(4)
				[188, 189]
6414.46(10)	(0 to 2 <sup>+</sup> )	109.28(12)	$2.3(1) \times 10^{-11}$ <sup>c</sup> [190]	0.0042(6) <sup>d</sup>
6436.44(11)	(3 to 5 <sup>+</sup> )	131.26(13)	$\leq 2.5 \times 10^{-10}$ [187]	0.727(3)
6495.94(7)	(3 to 5 <sup>+</sup> )	190.76(9)	$5.2(36) \times 10^{-7}$ <sup>e</sup>	0.75(2) [187]
6550.68(7)	(4 <sup>+</sup> , 5 <sup>-</sup> )	245.50(9)	$55.0(63) \times 10^{-7}$ [179]	0.80(1)
6598.32(16)	(5 <sup>+</sup> )	293.14(17)	$45.0(52) \times 10^{-6}$ [179]	0.71(1)
6610.40(6)	(3 <sup>-</sup> )	305.22(8)	$2.8(3) \times 10^{-2f}$	0.878(10) <sup>g</sup>
6680.45(7)	(2 <sup>+</sup> )	375.27(9)	$6.0(6) \times 10^{-2}$ [191]	0.67(1)
6724.25(7)	(4 <sup>-</sup> )	419.07(9)	$7.4(2) \times 10^{-2}$ [191]	0.96(1)
6783.79(5)	(2 <sup>-</sup> )	478.61(8)	$7.3(11) \times 10^{-2}$ [179]	0.56(1)
6789.30(4)	(3 <sup>-</sup> )	484.12(7)	$60.0(77) \times 10^{-3}$ [179]	0.90(1)

<sup>a</sup> Spectroscopic factor  $C^2S = 0.022$  from Endt and Rolfs [192], single-particle proton width calculated from the parameters given by Iliadis [193]. An uncertainty on the spectroscopic factor of 20% has been assumed.

<sup>b</sup> Expectation and variance of the resonance strength using  $\omega\gamma = 4.5 \times 10^{-22}$  and a factor 1.5 uncertainty in [184].

<sup>c</sup> Expectation and variance of the resonance strength using  $\omega\gamma = 2.1 \times 10^{-11}$  and a factor 1.5 uncertainty in [184].

<sup>d</sup> This resonance is given as  $f_0 = 0.71$  in [182] citing then yet-to-be-published paper by Endt, de Wit and Alderliesten which is presumably [194]. The decay branches listed in [194] give  $f_0 = 0.0041(7)$ . The listed  $\gamma$ -ray branches in the ENSDF database give  $f_0 = 0.0042(6)$ . We adopt  $f_0 = 0.0042(6)$ . This resonance is rather weak for both radiative capture to the ground state and isomeric state and the astrophysical impact of this reassignment is negligible.

<sup>e</sup> Weighted average with additional estimate of systematic uncertainty of  $\omega\gamma = 9.0(6) \times 10^{-7}$  [187] and  $\omega\gamma_g = 1.1(2) \times 10^{-7}$  and  $f_0 = 0.74(1)$  [191].

<sup>f</sup> Weighted average  $3.07(13) \times 10^{-2}$  [195] and  $\omega\gamma = 2.1(2) \times 10^{-2}$  and  $f_0 = 0.87(1)$  [191].

<sup>g</sup>  $f_0 = 0.91(1)$  using ENSDF values.

early 1980s [197, 198]. States at 6343 and 6400 keV were assigned as 3<sup>+</sup>, the latter only tentatively. Proton widths and resonance strengths were deduced for many of the states by scaling from the determined proton width for the 374 keV resonance. The  $^{25}\text{Mg}(^3\text{He},d)$  reaction was revisited at the Princeton AVF cyclotron, and it was found that the 6343 keV state is actually the 6364 keV (3<sup>+</sup>) state and the 6400 keV is a  $J = 2$  state at 6398 keV [199]. The state reported at 6343 keV in [197] was observed using the  $^{27}\text{Al}(^3\text{He},\alpha)^{26}\text{Al}$  but had been misassigned as a  $^{25}\text{Mg}+p$  resonance. It was not populated in the  $^{25}\text{Mg}(^3\text{He},d)$  reaction in [199], suggesting that the 6343 keV state is not a strong single-proton state and therefore does not play a crucial role in the overall reaction rate. The proton width for the 374 keV resonance was re-determined, using the  $\gamma$ -

ray branching ratio together with previous data, in [199], and found to be significantly lower,  $\Gamma_p = 0.82(20)$  eV [199], than the previously determined value  $\Gamma_p = 460(129)$  eV [198]. The calculated resonance strength for the 92 keV resonance ( $\omega\gamma \leq 2.7 \times 10^{-13}$  eV [199]) is significantly lower than the recently measured value, suggesting that the proton width might have been underestimated for the 374 keV resonance in [199]. Indeed, the resonance strength for the 92 keV resonance was revised to  $8.5 \times 10^{-11}$  eV in [200]. This is already much closer to the recently measured value  $\omega\gamma = 2.9(6) \times 10^{-10}$  [187].

The doublet of states at 6343 and 6364 keV was confirmed in [201], where  $J^\pi = 2^-$  was proposed for the 6399 keV state. A spin of  $(1^+, 2)$  for the 6399 keV state has been adopted in the latest Nuclear Data Sheet [1] instead of the previous suggestions of  $3^+$  [197, 198] and  $2^-$  [199, 201]. More recently, angular distribution data, measured with the Gammasphere detector array for the two most intense  $\gamma$ -ray transitions from the 6399 keV state, support a  $J^\pi = 2^-$  assignment for this state [186].

The resonance widths and strengths for the  $^{25}\text{Mg}(p, \gamma)^{26}\text{Al}$  reaction have been studied directly using a low-energy proton beam and  $^{25}\text{Mg}$  target, for example in [202–205]. In addition, spectroscopic factors for proton-unbound levels in  $^{26}\text{Al}$  and their influence on stellar reaction rates have been investigated, e.g. in [206]. For low-energy resonances, the strength is almost entirely determined by the proton width  $\Gamma_p$ :  $\omega\gamma = \omega \frac{\Gamma_p \Gamma_\gamma}{\Gamma} \approx \omega \Gamma_p$ , when  $\Gamma_p \ll \Gamma_\gamma$ . The proton width depends on the spectroscopic factor,  $C^2S$ , and the single-particle width  $\Gamma_{s.p.}$ , as  $\Gamma_p = C^2S \Gamma_{s.p.}$ . For a  $nlj$  proton-transfer, single-particle widths scale with the center-of-mass-energy as shown in figure 2 of [184]. Spectroscopic factors can be obtained from measurements [196, 200, 206], or from shell model calculations. For example, the strength for the 58 keV resonance has been recently extracted based on spectroscopic factors determined in the  $^{25}\text{Mg}(^7\text{Li}, ^6\text{He})^{26}\text{Al}$  reaction at the Q3D magnetic spectrometer of the HI-13 tandem accelerator [185].

Direct underground measurements of several resonances have been reported by the LUNA collaboration. The rate has also been recently measured underground at JUNA [207] and these data are being analysed. Limata *et al* [195] measured the strength for the 304 keV resonance from the emitted  $\gamma$ -rays and found it to be  $30.7 \pm 1.7$  meV, in good agreement with earlier work, with the exception of the AMS work of Arazi *et al* [191]. Limata *et al* also performed an AMS study and could not reproduce the result of Arazi *et al* [191] but instead agreed with their own  $\gamma$ -ray based value. They, therefore, neglected the Arazi *et al* [191] value in their recommended strength of  $30.8 \pm 1.3$  meV, which averaged their result with that of the NACRE compilation [208]. This result was then used as a reference strength for a study of the resonances at 92, 130 and 189.6 keV by Strieder *et al* [187]. Only an upper limit could be determined for the 130 keV resonance and it is not expected to contribute to the astrophysical rate.

Endt *et al* [182] studied the astrophysical aspects of the  $^{25}\text{Mg}(p, \gamma)^{26}\text{Al}$  reaction and made thorough compilations of the excited states in  $^{26}\text{Al}$  [209]. Iliadis *et al* [184] then reinvestigated the previous literature data in 1996, and reported a new suggested rate for the reaction. In particular resonances at  $E_r = 58$  and 92 keV were found to dominate the reaction rate in the temperature region 0.02–0.15 GK [184] relevant for hydrogen burning in stars. At 0.1–1.5 GK, the resonances at 190, 304, 374, and 418 keV, start to dominate the reaction rate as shown in [191].

We have recalculated the reaction rates using the RATESMC code. The resonance energy correction results in an effective increase in the resonance energies of 1.14 keV compared to the existing literature values based on  $E_{\text{res}} = E_x - S_p$ . For resonances with only upper limits for the resonance strengths, the reduced widths are estimated by randomly sampling from a Porter–Thomas distribution using the experimental upper limit as an hard cutoff value. This is not entirely statistically accurate since the experimental upper limits should be quoted to some confidence level with an associated probability density function used to derive the upper limit

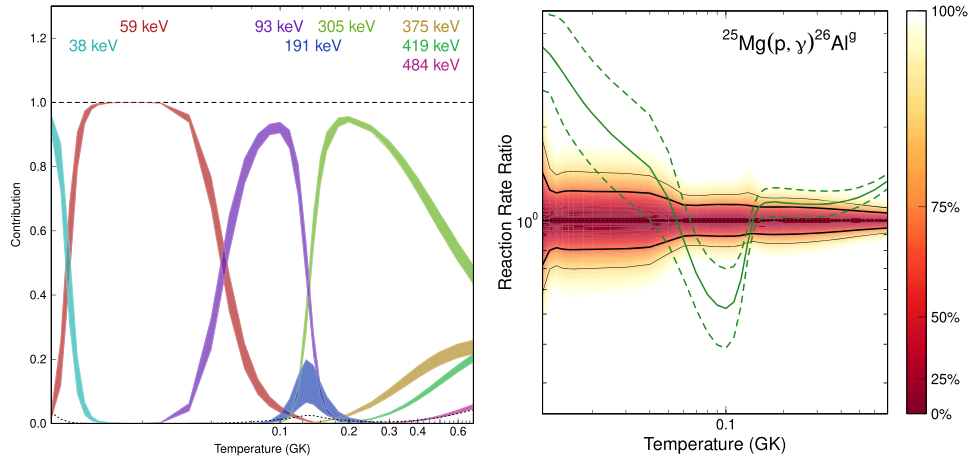


**Figure 9.** (Left) The fractional contribution of each resonance to the  $^{25}\text{Mg}(p, \gamma)^{26}\text{Al}^g$  based on the resonance parameters given in table 1. (Right) Contour heatmap of the current reaction rate uncertainties. The thick (thin) black curves are the 68% (95%) coverage limits. The green curves are median (solid) and 68% coverages (broken) for the  $^{25}\text{Mg}(p, \gamma)^{26}\text{Al}^g$  reaction rate from the compilation of Iliadis *et al* [213]. The decrease in the reaction rate at low temperatures is due to the shifted resonance energy computed, taking the atomic binding into account. The decrease in the reaction rate at  $T \approx 0.1$  GK is due to the updated resonance strength of the 93 keV resonance from LUNA and JUNA [187, 188]. The resonance strength and ground state branching fraction for the  $E_r = 93$  keV resonance are weighted averages of [187, 188] and [188, 189], respectively.

at that confidence level [210] (though these data are frequently lacking in the published studies). However, the effect of this is small (see [210–212] for more details). The corresponding contribution plots for the resonances are shown in figures 9 and 10. The 93- and 305 keV resonances dominate over the astrophysically relevant temperature range and both resonances have been measured directly by LUNA. The 59 keV resonance strength has thus far remained inaccessible for direct measurements. The corresponding re-evaluated reaction rates to the ground state and isomeric state of  $^{26}\text{Al}$  are given in tables 8 and 9. In addition to the proton-capture rate, the de-excitations from the populated states in  $^{26}\text{Al}$  to the ground and isomeric states of  $^{26}\text{Al}$  need to be taken into account. The rates are typically multiplied by the corresponding ground state branching fraction  $f_0$ , see, e.g. [184]. Thermal excitation between the states, discussed in section 4, complicates the situation.

As recently evident in the study of Lotay *et al*, there remains some uncertainty and occasional inconsistencies in the ground state branching fractions ( $f_0$ ) for each resonance. For example, the  $f_0$  value of the  $E_r = 95$  keV resonance was revised from  $f_0 = 0.52 \pm 0.02(\text{stat.}) \pm 0.06(\text{syst.})$  [186] to  $f_0 = 0.76(10)$  [189]. Similarly, on the basis of the  $\gamma$ -ray branching information stored in the ENSDF database, the  $f_0$  value for the astrophysically unimportant  $E_r = 109$  keV resonance has values ranging from  $f_0 = 0.0041(7)$  to  $f_0 = 0.71$  depending on the source. New, independent measurements of these ground state branching fractions are advisable in order to validate the existing results.

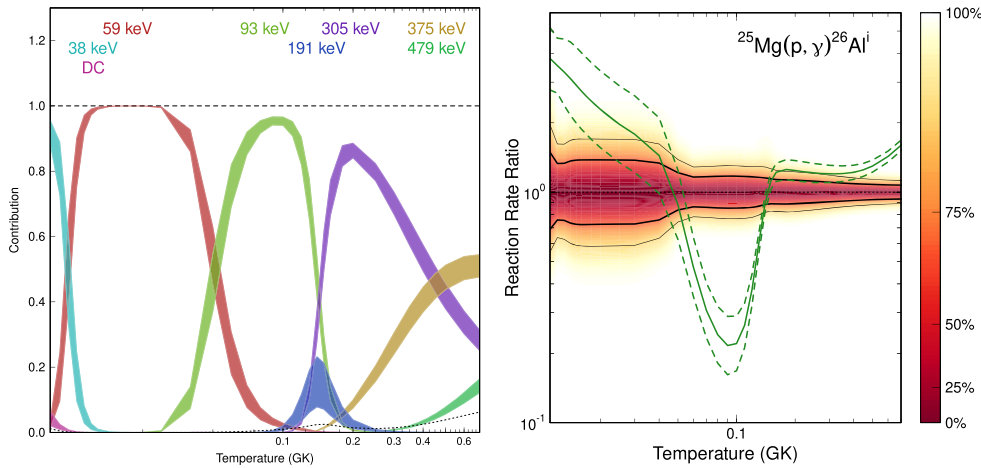


**Figure 10.** Same as figure 9 but for  $^{25}\text{Mg}(p, \gamma)^{26}\text{Al}^m$ . The decrease in the reaction rate at low temperatures is due to the shifted resonance energy computed, taking the atomic binding into account. The difference at  $T \approx 0.1$  GK is due to the updated information on the  $E_r = 93$  keV resonance from [187–189].

### 3.2. The destruction reaction $^{26}\text{Al}(p, \gamma)^{27}\text{Si}$

Proton capture on  $^{26}\text{Al}$  provides the main destruction mechanism for  $^{26}\text{Al}$  in several stellar sites such as classical novae, convective core hydrogen burning in massive stars, and hydrogen burning in intermediate-mass AGB stars. The uncertainties in the  $^{26}\text{Al}(p, \gamma)^{27}\text{Si}$  reaction rate at the temperatures present in these environments can result in large variations in the  $^{26}\text{Al}$  abundance. For example, sensitivity studies show that this uncertainty leads to variations of up to two orders-of-magnitude in AGB calculations [89]. The situation is further complicated by the existence of the 228 keV isomeric state in  $^{26}\text{Al}$ , which must be treated separately from the ground state at temperatures below 0.4 GK, as discussed above [216]. Thus, the  $^{26}\text{Al}^g(p, \gamma)^{27}\text{Si}$  and  $^{26}\text{Al}^m(p, \gamma)^{27}\text{Si}$  reaction rates must be determined independently to understand the destruction of  $^{26}\text{Al}$  in the stellar sites described above. Due to the impact of these reaction rates on the abundance of galactic  $^{26}\text{Al}$ , there have been a wide variety of direct and indirect measurements aimed at determining these rates.

For  $^{26}\text{Al}^g(p, \gamma)^{27}\text{Si}$  resonances at  $E_r > 190$  keV, which have less of an influence on the destruction of  $^{26}\text{Al}$ , the strengths are well constrained by previous direct measurements [217, 218]. The resonance around  $E_r = 184$ – $190$  keV is an important resonance but there is some disagreement in its resonance energy. The most recent direct measurement of  $^{26}\text{Al}^g(p, \gamma)^{27}\text{Si}$  was completed in inverse kinematics at TRIUMF using the DRAGON recoil separator with an intense  $^{26}\text{Al}$  ion beam ( $\sim 2.5 \times 10^9$   $^{26}\text{Al}$   $\text{s}^{-1}$ ). This study determined the energy and strength of the resonance that dominates the rate in classical novae to be  $E_r = 184 \pm 1$  keV and  $\omega\gamma = 35 \pm 7$   $\mu\text{eV}$ , respectively [219], resulting in an increase of 20% in  $^{26}\text{Al}^g$  production in nova models when compared with the previous unpublished values [217]. The properties of this resonance are consistent with a  $p$ -wave assignment for this resonance  $J^\pi = (7 - 13)/2^-$  based on the spectroscopic factor from a  $^{26}\text{Al}(^3\text{He}, d)^{27}\text{Si}$  measurement by Vogelaar *et al* [220]. A subsequent  $\gamma$ -ray spectroscopy study of  $^{27}\text{Si}$  gave a  $J^\pi = 11/2^+$  assignment to a state at  $E_x = 7651.9(6)$  keV [221, 222] based on comparison with the  $E_x = 7948$  keV state in the mirror nucleus,  $^{27}\text{Al}$ , corresponding to an  $\ell_p = 0$  resonance at  $E_r = 188.6(4)$  keV. A later  $^{26}\text{Al}(d, p)^{27}\text{Al}$  study clarified the spin and parity of the mirror state in  $^{27}\text{Al}$  as  $J^\pi = 11/2^-$

[214]. There is now a consensus that the resonance between  $E_r = 184 - 190$  keV has a  $J^\pi = 11/2^-$ ,  $\ell_p = 1$  assignment. The energy of this resonance remains a matter of some disagreement and there is not, at present, any way of resolving this discrepancy. To account for this we have computed the resonance energy with an inflated uncertainty following the procedure set out in [223].

While the measurement of Ruiz *et al* [219] significantly reduced the uncertainty in  $^{26}\text{Al}^g(p, \gamma)^{27}\text{Si}$  for nova nucleosynthesis, lower energy resonances dominate this reaction rate at the lower temperatures found in AGB and massive stars. At these lower energies, direct measurements become unfeasible with currently available  $^{26}\text{Al}$  beam intensities and indirect measurements are required. Specifically, the 127 keV resonance in  $^{27}\text{Si}$  is thought to dominate the reaction rate in these environments as it is the only known  $\ell_p = 0$  proton-capture resonance in this energy regime [224]. This and other resonances have been studied indirectly in a variety of measurements including transfer and  $\gamma$ -ray transition studies (e.g. [220, 221, 225, 226]). More recently, there have been multiple studies in inverse kinematics with unstable  $^{26}\text{Al}$  beams including two measurements of resonances in the mirror  $^{27}\text{Al}$  nucleus in inverse kinematics via the  $^{26}\text{Al}(d, p)^{27}\text{Al}$  reaction [107, 214] and a measurement of states in  $^{27}\text{Si}$  via  $^{26}\text{Al}(d, n)^{27}\text{Si}$  [227]. In these studies, spectroscopic factors of states in  $^{27}\text{Al}$  and  $^{27}\text{Si}$  were measured to determine the resonance strengths of those states. The values of the strength of the 127 keV resonance obtained via the mirror studies [107, 214] are in agreement with each other, but a factor of four higher than the previously accepted value [220]. However, there are worrying discrepancies for this resonance between the resonance information reported in [107] ( $C^2S = 0.0102(21)$  and  $\omega\gamma = 2.6_{-0.9}^{+0.7} \times 10^{-8}$  eV) and [228] ( $C^2S = 0.0093(7)$  and  $\omega\gamma = 5.7(4) \times 10^{-8}$  eV), i.e. a lower spectroscopic factor is calculated to result in a larger partial width and resonance strength. Based on this, some of the discrepancies between these experimental results are likely due to the theoretical treatment of the experimental data. Revisiting the original experimental studies and treating them with consistent experimental methods may help to resolve these discrepancies and will provide better constraints on  $^{26}\text{Al}$  destruction by proton capture. As an example, the later study of [228] notes that the results of [214] has a technical fault in the number of nodes for the computation of the transfer amplitudes. Notwithstanding these concerns, the 127 keV resonance dominates the reaction rate at relevant temperatures for  $^{26}\text{Al}$  nucleosynthesis in massive and AGB stars. While the  $^{26}\text{Al}(d, n)^{27}\text{Si}$  measurement only yielded an upper limit on the spectroscopic factor of this state, the results were consistent with these mirror studies [227]. Clearly, a direct measurement of this resonance strength—one which obviates some of the theoretical inconsistencies of the transfer data is a high priority for future studies once more intense  $^{26}\text{Al}$  beams become available.

As discussed above, at temperatures below around 0.4 GK, the isomer and ground state must be treated as separate nuclei and thus the  $^{26}\text{Al}^m(p, \gamma)^{27}\text{Si}$  reaction rate should be determined independently from proton capture on the ground state. However, previous determinations of this reaction rate were typically scaled from the  $^{26}\text{Al}^g(p, \gamma)^{27}\text{Si}$  rate, despite the large spin difference between the ground ( $5^+$ ) and isomeric ( $0^+$ ) states, as little experimental data for proton capture on the isomer was available [229]. A direct measurement of the strength of the  $E_r = 447$  keV resonance in  $^{26}\text{Al}^m(p, \gamma)^{27}\text{Si}$  is currently the only direct resonance information for this reaction [230]. A measurement of the  $^{27}\text{Al}(^3\text{He}, t)^{27}\text{Si}^*(p)^{26}\text{Al}^{g,m}$  and  $^{28}\text{Si}(^3\text{He}, \alpha)^{27}\text{Si}^*(p)^{26}\text{Al}^{g,m}$  reactions was performed at the Wright Nuclear Structure Laboratory to indirectly determine the  $^{26}\text{Al}^m(p, \gamma)^{27}\text{Si}$  reaction rate based on experimental information [231]. While this study was only able to put a lower limit on the reaction rate, as proton decays from states in  $^{27}\text{Si}$  at energies of  $E_r \geq 445$  keV could be measured, this study confirmed that different resonances in  $^{27}\text{Si}$  dominate the two rates. A similar study of the  $^{27}\text{Al}(^3\text{He}, t)^{27}\text{Si}^*(p)^{26}\text{Al}$  reaction using the same Enge Split-Pole spectrograph, now installed at the John D Fox Accelerator laboratory at Florida State University,

was recently performed detecting proton decays down to  $E_r \simeq 300$  keV in order to further improve the reaction rate determination [232].

Alongside these charge-exchange reaction studies, a complementary investigation of the  $\gamma$ -decaying properties of  $^{26}\text{Al}^m + p$  resonant states was performed at Argonne National Laboratory [222, 233, 234]. In that work [222, 233, 234], a  $^{12}\text{C}(^{16}\text{O}, n)$  fusion-evaporation reaction was used to populate excited states in  $^{27}\text{Si}$ , located above the  $^{26}\text{Al}^m + p$  emission energy of 7691.3(1) keV [235], and the resulting  $\gamma$  decays were recorded with the Gammasphere detector array [236, 237].  $\gamma$  decays were observed from all resonant states with energies  $E_r \leq 500$  keV and spin assignments were obtained from angular distribution measurements. Furthermore, by examining the mirror nucleus  $^{27}\text{Al}$  over a suitable energy range, it was possible to propose parity assignments for key resonances. In [222, 233, 234], it was concluded that a  $J^\pi = 5/2^+$  state at  $E_r = 146.3(3)$  keV is likely to dominate the astrophysical  $^{26}\text{Al}^m(p, \gamma)$  reaction for low stellar temperatures, while a proposed  $J^\pi = 3/2^-$  state at  $E_r = 378.3(30)$  keV governs the rate for temperature,  $T > 0.15$  GK. However, it should be noted that due to the very high excitation energies of  $^{26}\text{Al}^m + p$  resonant states, the accurate matching of mirror states is extremely challenging. In particular, it is very difficult to know how mirror shifts are affected when both the  $^{27}\text{Si}$  and  $^{27}\text{Al}$  systems become particular unbound, which is the case for a number of the proposed analog pairs.

More recently, a measurement of the  $^{26}\text{Al}^m(d, p)^{27}\text{Al}$  reaction in inverse kinematics was performed using an isomeric  $^{26}\text{Al}$  beam produced at the ATLAS facility at Argonne National Laboratory [215]. Similar to the studies of Pain *et al* [107] and Margerin *et al* [214], this measurement aimed to determine spectroscopic factors of states in  $^{26}\text{Al}(d, p)^{27}\text{Al}$  reactions that are mirrors of the  $^{26}\text{Al}^m + p$  resonances in  $^{27}\text{Si}$ . Using this mirror symmetry, an upper limit of the reaction rate was determined, which is dominated by resonances at  $E_r = 146$  and 378 keV over astrophysically relevant temperatures. The  $^{26}\text{Al}^m(p, \gamma)^{27}\text{Si}$  reaction rate determined here is smaller than that for the ground state by an order of magnitude or more at  $T_9 \leq 0.3$  GK, implying that destruction via the isomer is not significant in most stellar sites. However, further study of resonances in  $^{27}\text{Si}$  both directly and indirectly is still warranted.

We have recomputed the  $^{26}\text{Al}(p, \gamma)^{27}\text{Si}$  reaction rates (i.e. for the ground and metastable states) using the RATESMC code [211] and the information in tables 2 and 3. The corresponding contribution plots for the resonances are shown in figures 11 and 12. Resonances for which there is no measured proton width or resonance strength have been treated by assuming that the reduced proton widths are drawn from a Porter–Thomas distribution with mean  $\theta^2 = 0.0045$  with a factor of 3 variation on that mean value. This factor variation is based on the observed scatter in the mean of the Porter–Thomas distribution determined from experimental results of proton capture and scattering reactions. For more details about this assumption including the data upon which this assumption is based, see the discussion in section 5.2.1 of [210] and the experimentally determined spread in the reduced widths reported in figure 4 and section IV.B of [212]. Experimental upper limits are used to truncate the distribution where appropriate. There are a number of different sources for the resonance information for the two reactions which have been discussed in the text above. The sources for different spectroscopic information used in the calculations of the rates are given in tables 2 and 3. Of particular note in the present evaluation is the increased uncertainty in the resonance energy of the  $E_r = 188$  keV resonance due to the disagreement between the resonances energies determined with DRAGON and  $\gamma$ -ray spectroscopy, and the probable need for a reconsideration of the various  $^{26}\text{Al}(d, p)^{27}\text{Al}$  mirror studies to try to account for systematic differences between experiments before a full re-evaluation of the  $^{26}\text{Al}^m(p, \gamma)^{27}\text{Si}$  reaction with realistic uncertainties.

For the  $^{26}\text{Al}^m(p, \gamma)^{27}\text{Si}$  reaction rate, the rate has been recalculated only using known level information. While this information is somewhat lacking in the region of interest, the recent

**Table 2.** Recommended excitation energies ( $E_x$ ) together with the spins and parities ( $J^\pi$ ) for the excited states above the proton separation energy ( $S_p = 7463.34(13)$ ) keV [181] in  $^{27}\text{Si}$  for the  $^{26}\text{Al}^g(p, \gamma)^{27}\text{Si}$  reaction. The resonance energies ( $E_{\text{res}}$ ) and experimentally determined resonance strengths ( $\omega\gamma$ ) for the relevant states are given where available. The atomic shift for this reaction is  $\Delta B_e = -1.27$  keV. The states listed in brackets are tentative resonance states which were included in the evaluation of the reaction rate. As demonstrated in figure 11, the impact of these resonances on the reaction rate is negligible.

$E_x$ (keV)	$J^\pi$	$E_{\text{res}}$ (keV)	$\omega\gamma$ (eV)
7469.2(6)	(1/2, 5/2) <sup>+</sup>	6.8(9)	$< 1.8 \times 10^{-63}$ [226]
(7493.1(40))	(3/2) <sup>+</sup>	(31(4))	$< 1.5 \times 10^{-28a}$
7531.5(5)	5/2 <sup>+</sup>	69.3(7)	$< 3.6 \times 10^{-16}$ [228]
(7557(3)) [226]	(3/2) <sup>+</sup>	(95(3))	$< 3.4 \times 10^{-15}$ [107]
7589.89(12)	9/2 <sup>+</sup>	128.1(9)	$4.2(16) \times 10^{-8b}$
7651.68(11)	11/2 <sup>+</sup>	187.7(23)	$35(7) \times 10^{-6}$ [219]
7693.8(9)	5/2 <sup>+</sup>	231.8(9)	$< 1.0 \times 10^{-5}$ [217]
7704.3(2)	7/2 <sup>+</sup>	242.3(2)	$1.0(5) \times 10^{-5}$ [217]
7739.06(11)	9/2 <sup>+</sup>	277.01(17)	$3.8(10) \times 10^{-3}$ [238]
7831.5(5)	9/2 <sup>-</sup>	369.5(5)	$65(18) \times 10^{-3}$ [238]
8156(2)		694(2)	$51(27) \times 10^{-3}$ [238]
8167.3(12)	(11/2) <sup>+</sup>	705.3(12)	$16(6) \times 10^{-3}$ [238]
8224(2)	(7/2) <sup>+</sup>	762(2)	$35(13) \times 10^{-3}$ [238]
8287(3)	(7/2 <sup>+</sup> to 13/2 <sup>+</sup> )	825(3)	$41(16) \times 10^{-3}$ [238]
8356(2)	(3/2 <sup>+</sup> to 9/2 <sup>+</sup> )	894(2)	$67(28) \times 10^{-3}$ [238]

<sup>a</sup> Resonance strength upper limit obtained using the Wigner limit for the proton width.

<sup>b</sup> Weighted average of [107, 228].

**Table 3.** Recommended excitation energies ( $E_x$ ) together with the spins and parities ( $J^\pi$ ) (taken from [234]) for the excited states above the proton separation energy ( $S_p = 7691.65(13)$ ) keV [181] in  $^{27}\text{Si}$  for the  $^{26}\text{Al}^m(p, \gamma)^{27}\text{Si}$  reaction. The resonance energies ( $E_{\text{res}}$ ) and experimentally determined resonance strengths ( $\omega\gamma$ ) for the relevant states are given where available. The atomic shift for this reaction is  $\Delta B_e = -1.27$  keV.

$E_x$ (keV)	$J^\pi$	$E_{\text{res}}$ (keV)	$\omega\gamma$ (eV)
7693.8(9)	5/2 <sup>+</sup>	3.5(9)	$< 2.90 \times 10^{-86}$ [239]
7704.3(2)	7/2 <sup>+</sup>	14.0(2)	$< 4.61 \times 10^{-44}$ [239]
7739.3(4)	9/2 <sup>+</sup>	49.0(4)	$< 2.69 \times 10^{-22}$ [239]
7794.8(19)	7/2 <sup>+</sup>	104.5(19)	$< 1.92 \times 10^{-14}$ [239]
7831.5(5)	9/2 <sup>-</sup>	141.2(5)	$< 2.39 \times 10^{-14}$ [239]
7837.6(2)	5/2 <sup>+</sup>	147.2(2)	$< 1.5 \times 10^{-8}$ [240]
7899.0(8)	5/2 <sup>+</sup>	208.7(8)	$< 1.61 \times 10^{-5}$ [239]
7909.1(7)	3/2 <sup>+</sup>	218.8(7)	$< 1.4 \times 10^{-6}$ [240]
7966.3(8)	5/2 <sup>+</sup>	276.0(8)	$< 2.08 \times 10^{-4}$ [239]
8031.5(11)	5/2 <sup>+</sup>	341.2(11)	$< 3 \times 10^{-8}$ [215]
8069.6(30)	3/2 <sup>-</sup>	379.3(30)	$< 3.3 \times 10^{-4}$ [240]
8139.3(6)	1/2 <sup>-</sup>	449.3(6)	$434(214) \times 10^{-3}$ [230]
8318(3)	1/2 <sup>+</sup>	626(3)	0.35(7) [231]
8375(3)	1/2 <sup>-</sup> /3/2 <sup>-</sup>	683(3)	0.24(6)/0.48(12) [231]
8446(3)	Assumed 1/2 <sup>+</sup>	754(3)	0.32(5) [231]

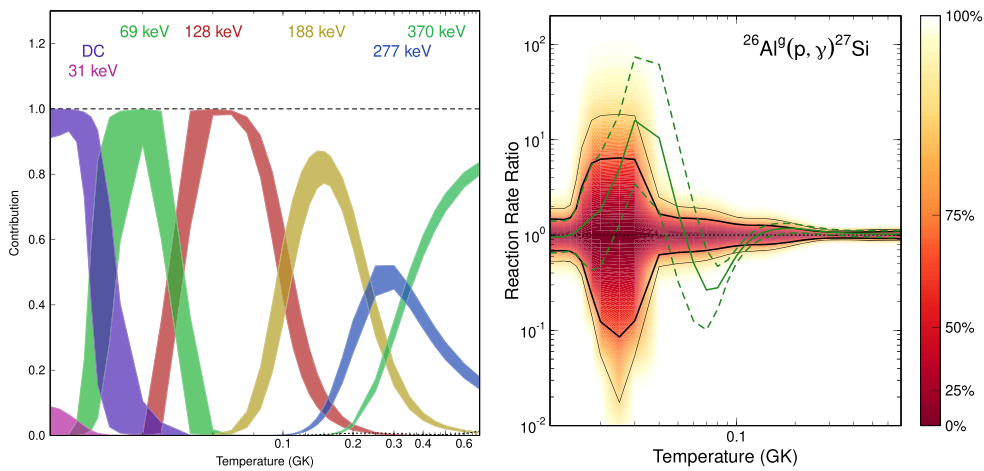


**Figure 11.** Same as figure 9 but for  $^{26}\text{Al}^g(p, \gamma)^{27}\text{Si}$ . The variations in the rates are due to the updated  $\Gamma_p$  proton partial widths derived from the  $^{26}\text{Al}(d, p)^{27}\text{Al}$  experiments of [107, 214, 215].

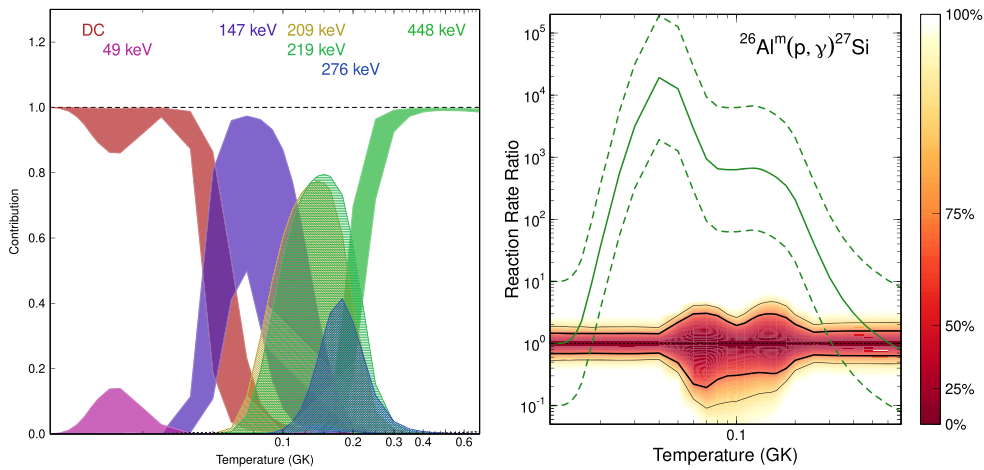


**Figure 12.** Same as figure 9 but for  $^{26}\text{Al}^m(p, \gamma)^{27}\text{Si}$ , except the green lines are for  $^{26}\text{Al}^g(p, \gamma)^{27}\text{Si}$  since [213] suggests using this rate as a proxy for the  $^{26}\text{Al}^m(p, \gamma)^{27}\text{Si}$  reaction rate due to the paucity of spectroscopic information in  $^{27}\text{Si}$ .

direct measurement of the 447 keV resonance strength, which dominates the reaction rate from 0.3 to 2.5 GK [230], now allows for a more accurate reaction rate determination. Nevertheless, some caution is required in the interpretation of the  $^{26}\text{Al}^m(p, \gamma)^{27}\text{Si}$  reaction rate since many of the known states in  $^{27}\text{Si}$  have spins and parities identified from fusion-evaporation reactions [221]; these reactions introduce a large amount of angular momentum and low-spin states may readily be missed in these experiments. Studies of low-spin states are therefore encouraged, especially indirect measurements of the 218 keV resonance, which is likely to dominate the reaction rate at temperatures below 0.3 GK. Comparison with the mirror nucleus,  $^{27}\text{Al}$ , which has been rather well studied may help to rule out the existence of additional states.



### 3.3. Neutron-induced destruction reactions

The sensitivity study by Iliadis *et al* [241] has shown that the  $^{26}\text{Al}(n, p)^{26}\text{Mg}$  and  $^{26}\text{Al}(n, \alpha)^{23}\text{Na}$  reactions are of importance for the determination of  $^{26}\text{Al}$  abundances produced during hydrostatic C-shell and explosive Ne/C-shell burning phases in massive stars. These reactions involve excited states in  $^{27}\text{Al}$  within about 500 keV above the  $^{26}\text{Al} + n$  threshold ( $S_n = 13057.91$  (12) keV) where the level density  $\rho$  is extremely high ( $\rho \equiv dN(E_x)/dE_x > 80 \text{ MeV}^{-1}$  [242]). These states decay by proton or  $\alpha$ -particle emission because of the lower  $^{26}\text{Mg} + p$  and  $^{23}\text{Na} + \alpha$  thresholds ( $S_p = 8271$  keV,  $S_\alpha = 10092$  keV).

At present, only few experimental data on both reactions are available. The first measurement of the  $^{26}\text{Al}(n, p_1)^{38}$  reaction was performed by Trautvetter and Käppeler using a quasi-Maxwellian neutron spectrum at around  $kT = 31$  keV [243]. This was followed by a more comprehensive study in 1984 [244] using neutron spectra around various energies (40 meV, 31 keV, 71 keV, and 310 keV), including also the  $^{26}\text{Al}(n, p_0)$  channel, which is 3-100 times weaker than  $(n, p_1)$ , and providing an upper limit on the  $^{26}\text{Al}(n, p_2)$  channel at 40 meV. Roughly 10 years later, Koehler *et al* [245] determined  $^{26}\text{Al}(n, p_1)$  and  $^{26}\text{Al}(n, \alpha_0)$  cross sections using the neutron time-of-flight technique at the Los Alamos Neutron Science Center (LANSCE). The  $^{26}\text{Al}(n, p_1)$  cross section was found to be in disagreement with the earlier data [244] in the limited neutron energy range of overlap (at around 30 keV), leading to a higher stellar reaction rate by a factor of about two. Roughly 15 years ago, De Smet *et al* reported a measurement of  $^{26}\text{Al}(n, \alpha_{0+1})$  reaction cross sections using the GELINA neutron time-of-flight facility at the Geel Joint Research Centre of the European Commission [246]. The GELINA measurements overlapped in the lower neutron regime with the the LANSCE experimental study (the maximum neutron energy for the  $(n, \alpha_0)$  study was 10 keV [245]) and also data at higher neutron energies were obtained. De Smet *et al* identified several new resonances for the  $^{26}\text{Al}(n, \alpha)$  reaction. Both, Koehler *et al* and De Smet *et al*, provided resonance strengths for a resonance at around 6 keV neutron energy, however, their results disagree by a factor of 1.8. This leads to a large discrepancy of the astrophysical reaction rates deduced from these data.

Additional data on states above the neutron separation threshold and resonance strengths were obtained by Skelton *et al* [247], who performed an experiment using the time-reverse  $^{26}\text{Mg}(p, n)^{26}\text{Al}$  and  $^{23}\text{Na}(\alpha, n)^{26}\text{Al}$  reactions, thereby accessing information on the  $(n, p_0)$  and  $(n, \alpha_0)$  channels. The  $(n, p_1)$  channel is thought to be astrophysically dominant, but it is not accessible in time-reversed experiments.

Recently, there have been new direct measurements of  $^{26}\text{Al}(n, p)^{26}\text{Mg}$  and  $^{26}\text{Al}(n, \alpha)^{23}\text{Na}$  reactions at the new high neutron flux beamline EAR-2 at n\_TOF CERN, and at the GELINA facility [248, 249]. Both reaction cross sections were measured up to about 150 keV neutron energy, extending the previously available experimental range for energy dependent data. Resonance strengths of several resonances were provided for the first time. Astrophysical reaction rates, including all relevant branches could be deduced from the data up to about 0.6 GK stellar temperature. Resonance strengths obtained for the  $^{26}\text{Al}(n, \alpha)^{23}\text{Na}$  reaction in [249] agree well with previous data by De Smet *et al* [246], leading to a good agreement of astrophysical reaction rates at low stellar temperatures. For the  $^{26}\text{Al}(n, p)^{26}\text{Mg}$  channel astrophysical reaction rates are higher in the energy region of overlap compared to Trautvetter *et al* [244], however compatible within 2 standard deviations. Resonance strengths for both reactions are lower than results by Koehler *et al* [245].

<sup>38</sup> The subscript 1 refers to particle emission to the first excited state of  $^{26}\text{Mg}$ .

**Table 4.** Resonance energies  $E_R$  and resonance strengths  $\omega\gamma$  determined in previous direct and time-reversed experiments for  $^{26}\text{Al}(n, \alpha)$  and  $^{26}\text{Al}(n, p_1)$  resonances.

Author	$E_R$ (keV)	$\omega\gamma_\alpha$ (eV)	$\omega\gamma_{\alpha 0}$ (eV)	$\omega\gamma_{p1}$ (eV)
Lederer-Woods <i>et al</i> [248, 249]	$5.9 \pm 0.1$	$4.25 \pm 0.41$	$4.04 \pm 0.39$	$1.28 \pm 0.20$
	$21.9 \pm 0.2$	$1.62 \pm 0.41$	$1.56 \pm 0.40$	$< 0.6$
	$31.4 \pm 0.4$	$1.62 \pm 0.63$		$5.8 \pm 1.5$
	$35.7 \pm 0.4$	$3.7 \pm 1.0$	$< 0.55$	$43.4 \pm 10.7$
	$41.3 \pm 0.4$	$19.1 \pm 3.6$	$9.0 \pm 2.0$	$22.9 \pm 5.3$
	$57 \pm 2$	$1.8 \pm 1.2$		$2.7 \pm 1.8$
	$75 \pm 2$			$8.1 \pm 3.7$
	$86 \pm 4$	$8.9 \pm 7.7$		$85 \pm 23$
	$\approx 105$	$38 \pm 11$		$53 \pm 14$
	$\approx 120$	$34 \pm 10$		$46 \pm 13$
	$\approx 140$	$151 \pm 30$		$71 \pm 23$
De Smet <i>et al</i> [246]	$5.87 \pm 0.02$	$4.23 \pm 0.36$	$3.68 \pm 0.34$	
	$21.98 \pm 0.1$	$1.83 \pm 0.27$	$1.83 \pm 0.27$	
	$34.95 \pm 0.2$	$5.98 \pm 0.86$	only $\alpha_1$	
	$41.3 \pm 0.2$	$20.19 \pm 2.02$	$11.1 \pm 1.5$	
	$85.2 \pm 0.8$			
	$108.5 \pm 1.1$			
Koehler <i>et al</i> [245]	5.578		$6.6 \pm 1.7$	$2.03 \pm 0.51$
	33.7			$128 \pm 22$
Skelton <i>et al</i> [247]	$5.8 \pm 2$		$\leq 6.4$	
	$22.4 \pm 2$		$\leq 2.5$	
	$42 \pm 2$		$14 \pm 1.4$	

A summary of experimental resonance strengths for  $^{26}\text{Al} + n$  resonances is listed in table 4 (note that these data refer to reactions on the experimentally accessible ground state of  $^{26}\text{Al}$ ).

Indirect studies have also been undertaken to determine the properties of  $^{27}\text{Al}$  states above the  $^{26}\text{Al}^g + n$  and the  $^{26}\text{Al}^m + n$  thresholds, e.g. excitation energy, spin/parity, branching ratio.  $^{27}\text{Al}$  states have been populated using proton inelastic scattering at the Tandem-ALTO (Orsay, France) and MLL (Munich, Germany) facilities. Protons were detected using the Enge Split-Pole [250] and Q3D [251] high-resolution magnetic spectrometers as the main detection system, respectively. Energies of more than 30 new  $^{27}\text{Al}$  states have been determined above the neutron threshold up to an excitation energy of 13.8 MeV [250]. Proton inelastic scattering has a very unselective reaction mechanism that is well adapted to populate all excited states [252–254], however, on its own, it does not easily allow to identify low orbital momentum neutron capture resonances. Based on the energy of populated  $^{27}\text{Al}$  states, the first four lowest energy resonances observed by De Smet *et al* [246] were populated [250]. Proton and  $\alpha$ -particle branching ratios have also been determined for these states by coupling a DSSSD (Double-sided Silicon Stripped Detector) array to the Enge Split-Pole spectrometer [251].

At present, the main remaining challenge is to extend our present knowledge of the properties (energy and strength) of the dominating resonances up to about 500 keV above the  $^{26}\text{Al} + n$  threshold. In the alternative approach of indirect measurements it may be interesting

to complete the branching ratio measurement by the study of the  $^{26}\text{Al}(d, p)^{27}\text{Al}$  reaction. This could be used to determine the neutron width, hence providing an indirect determination of the resonance strength. The interest of such transfer reaction is to have the same selectivity as the neutron capture reactions. Such measurements have been reported [107, 214], however, they only cover excitation energies lower than 12 MeV in  $^{27}\text{Al}$ . Extending these studies to higher energies would be interesting, though challenging due to the increasing background, the low proton energies, and the limited  $^{26}\text{Al}$  beam intensity.

### 3.4. The bypass reaction $^{25}\text{Al}(p, \gamma)^{26}\text{Si}$

Understanding the  $^{25}\text{Al}(p, \gamma)^{26}\text{Si}$  astrophysical reaction rate is especially important in higher-temperature environments such as novae, where this reaction becomes faster than the  $^{25}\text{Al}$   $\beta$  decay (7.2 s). If the proton-capture rate on  $^{25}\text{Al}$  is faster than  $\beta$  decay,  $^{26}\text{Si}$  will be produced, which in turn decays to the  $^{26}\text{Al}$  isomer. The isomer subsequently decays ( $t_{1/2} = 6.3$  s) to the ground state of  $^{26}\text{Mg}$ , and production of the long-lived  $^{26}\text{Al}$  ground state is bypassed (figure 6).

As radioactive beams of  $^{25}\text{Al}$  are not currently available at sufficient intensities to directly measure the reaction cross section, estimates of the astrophysical reaction rate have generally been based upon knowledge of the nuclear structure of  $^{26}\text{Si}$ . Of relevance to the rate are nuclear levels near the proton threshold at  $S_p = 5513.8(5)$  keV in  $^{26}\text{Si}$  [255]. Especially important is identifying  $2^+$  or  $3^+$  levels near the threshold that could provide  $s$ -wave resonances for the  $^{25}\text{Al}(p, \gamma)^{26}\text{Si}$  reaction. Shell model calculations and comparisons with the  $^{26}\text{Mg}$  mirror nucleus indicate that levels of interest may include two  $4^+$  states, a  $1^+$  state, a  $3^+$  state, and a  $0^+$  state in the rough excitation energy range  $E_x = 5400\text{--}6200$  keV [184, 256, 257].

Some of the first studies searching for relevant  $^{26}\text{Si}$  states utilized measurements of the  $^{28}\text{Si}(p, t)^{26}\text{Si}$  [258] and  $^{29}\text{Si}(^3\text{He}, ^6\text{He})^{26}\text{Si}$  reactions [259]. Energies for astrophysically-important levels were extracted from extrapolations of lower-lying level energies previously measured with high precision using  $\gamma$  rays [260]. The energies of several levels near threshold were determined with greater precision, and triton angular distributions from the  $^{28}\text{Si}(p, t)^{26}\text{Si}$  reaction provided sensitivity to the angular momentum transfers. In 2004, Parpottas *et al* [261] studied the  $^{24}\text{Mg}(^3\text{He}, n)^{26}\text{Si}$  reaction and largely confirmed the excitation energies extracted previously [258, 259]. More interestingly, however, Parpottas *et al* [261] deduced, from comparisons with statistical model calculations, that the previously-observed level at  $\sim 5916$  keV was actually the important  $3^+$  level providing an  $s$ -wave resonance in the  $^{25}\text{Al}(p, \gamma)^{26}\text{Si}$  reaction. This hypothesis was later deemed to be consistent with the angular distribution measured in the  $^{28}\text{Si}(p, t)^{26}\text{Si}$  reaction [262].

As this  $3^+$  resonance dominates the  $^{25}\text{Al}(p, \gamma)^{26}\text{Si}$  astrophysical reaction rate, the next most important factor, after its energy, to be determined is its resonance strength. Since the proton width is expected to be much larger than the  $\gamma$  width [184], the resonance strength can be determined once the  $\gamma$  width is known. Early estimates simply assumed the width was the same as the mirror  $^{26}\text{Mg}$  level (i.e.  $\Gamma_\gamma = 33 \pm 14$  meV) where the uncertainty comes from the uncertain  $^{26}\text{Mg}$  lifetime and does not account for uncertainties in isospin symmetry [184, 262]. This lifetime was recently remeasured by [263] resulting in  $\Gamma_\gamma = 33 \pm 5$  meV for the mirror level. Other estimates have come from combining the proton width estimated from a  $^{25}\text{Al}(d, n)^{26}\text{Si}$  proton-transfer measurement [264] with subsequent determinations of the  $\gamma$  to proton branching ratios,  $\Gamma_\gamma/\Gamma_p$ , to extract  $\Gamma_\gamma = 39 \pm 21$  meV [265],  $\Gamma_\gamma = 59 \pm 29$  meV [257], and  $\Gamma_\gamma = 71 \pm 32$  meV [266].

The second most important resonance contribution arises from the  $1^+$  state at  $\sim 5675$  keV [255]. The resonance is expected to dominate at lower nova temperatures ( $T < 0.2$  GK). The existence of this state was first identified by Caggiano *et al* [259], and was later verified in

**Table 5.** Recommended excitation energies ( $E_x$ ) together with the spins and parities ( $J^\pi$ ) for the excited states above the proton separation energy ( $S_p = 5513.98(13)$  keV [181]) in  $^{26}\text{Si}$ . The resonance energies ( $E_{\text{res}}$ ), proton widths ( $\Gamma_p$ ), and experimentally determined resonance strengths ( $\omega\gamma$ ) for the relevant states are given. The atomic shift for this reaction is  $\Delta B_e = -1.27$  keV. Only states producing resonances below  $E_{\text{res}} = 500$  keV are listed.

$E_x$ (keV)	$J^\pi$	$E_{\text{res}}$ (keV)	$\Gamma_p$ (eV)	$\omega\gamma$ (eV)
5675.2(14) [255]	$1^+$ [269]	162.5(14)	$<1 \times 10^{-8}$ [270]	$<2.6 \times 10^{-9}$ [270]
5890.0(8) [255]	$0^+$ [269]	377.3(8)	$4.2(13) \times 10^{-3}$ [270] <sup>a</sup>	$2.4(7) \times 10^{-4}$ [270] <sup>a</sup>
5928(1) [255]	$3^+$ [261]	415(1)	$2.9(10)$ [264]	$2.3(13) \times 10^{-2}$ [265]
5950(5) [255]	$(4^+)$ [257]	437(5)	$7.8(39) \times 10^{-3}$ [257] <sup>b</sup>	$4.5(23) \times 10^{-3}$ [257] <sup>b</sup>

<sup>a</sup> A 30% uncertainty was assumed for properties extrapolated from the mirror [272].

<sup>b</sup> A 50% uncertainty was assumed for properties calculated with the shell model [256].

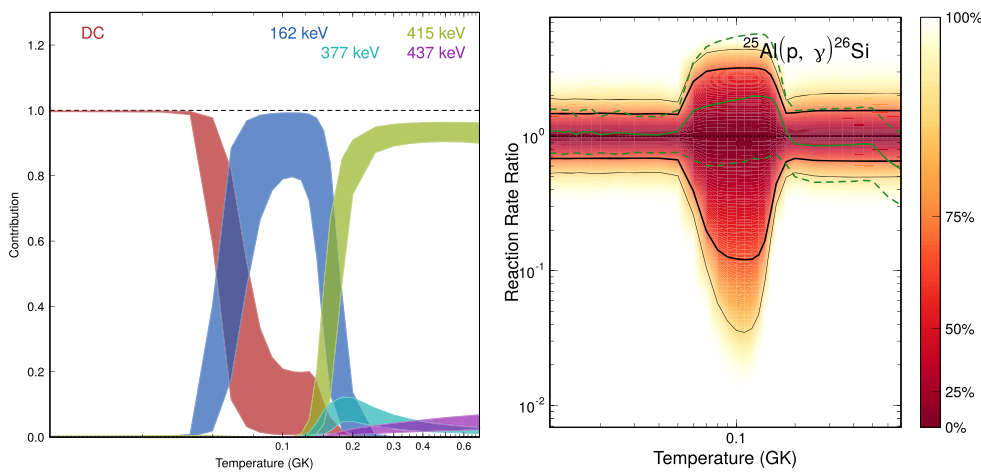


**Figure 13.** Same as figure 9 but for  $^{25}\text{Al}(p, \gamma)^{26}\text{Si}$ . The main difference here is that the  $E_r = 162$  keV resonance is treated as an upper limit rather than as having a measured resonance strength.

$^{24}\text{Mg}(^3\text{He}, n)^{26}\text{Si}$  studies detecting neutrons [261] and  $\gamma$  rays [267–269]. The strength of this resonance is determined by its proton width and estimates currently rely on shell model calculations [256] as only upper limits have been obtained for the strength of the mirror level in  $^{25}\text{Mg}(d, p)^{26}\text{Mg}$  studies [270].

An additional open question has been recently highlighted by studies of the  $^{24}\text{Mg}(^3\text{He}, n\gamma)^{26}\text{Si}$  reaction [268, 269, 271]. Population of a new level at 5890 keV has been observed and conclusively identified as a  $0^+$  state [269]. This seemingly presents an open issue since the 5949 keV level had previously been assigned as  $0^+$  by Parpottas *et al* [261], and shell model calculations indicate that there should only be one  $0^+$  state in this energy range [241, 256, 257]. Various authors have speculated that the 5949 keV may in fact be the expected  $4^+$  level [255, 257], but this would be at odds with the cross section comparison made by Parpottas *et al* [261].

Recommended resonance values are displayed in table 5 and our newly calculated rate in figure 13. Considering the current state of our knowledge, it appears that the astrophysical

**Table 6.** Maxwellian-averaged capture cross sections of  $^{24}\text{Mg}(n, \gamma)$  at temperatures higher than those reported in [286]. The contributions from the unresolved resonance region and the direct radiative capture are given separately. The uncertainty on the DRC contribution is mainly related to the uncertainty on the spectroscopic factors of the low-lying states populated by the direct transitions and is estimated to be approximately 20%.

Temperature		MACS				Reaction Rate $\text{cm}^3 \text{mol}^{-1} \text{s}^{-1}$
$kT$ (keV)	$T_9$ (K)	RRR (mb)	URR (mb)	DRC (mb)	Total (mb)	
120	1.4	$2.3 \pm 0.2$	0.0	0.3	$2.6 \pm 0.3$	$7.48 \times 10^{+05}$
140	1.6	$2.0 \pm 0.2$	0.0	0.3	$2.3 \pm 0.3$	$7.40 \times 10^{+05}$
160	1.9	$1.8 \pm 0.2$	0.0	0.3	$2.1 \pm 0.2$	$7.29 \times 10^{+05}$
180	2.1	$1.6 \pm 0.2$	0.0	0.3	$2.0 \pm 0.2$	$7.18 \times 10^{+05}$
200	2.3	$1.4 \pm 0.1$	0.0	0.4	$1.8 \pm 0.2$	$7.06 \times 10^{+05}$
220	2.6	$1.3 \pm 0.1$	0.1	0.4	$1.7 \pm 0.2$	$6.94 \times 10^{+05}$
240	2.8	$1.2 \pm 0.1$	0.1	0.4	$1.6 \pm 0.2$	$6.82 \times 10^{+05}$
260	3.0	$1.1 \pm 0.1$	0.1	0.4	$1.5 \pm 0.2$	$6.71 \times 10^{+05}$
280	3.2	$1.0 \pm 0.1$	0.1	0.4	$1.5 \pm 0.2$	$6.60 \times 10^{+05}$
300	3.5	$0.9 \pm 0.1$	0.1	0.4	$1.4 \pm 0.2$	$6.51 \times 10^{+05}$

$^{25}\text{Al}(p, \gamma)^{26}\text{Si}$  reaction rate is uncertain by roughly a factor of 3 at nova temperatures, primarily due to the uncertain  $\Gamma_\gamma$  of the  $J^\pi = 3^+$  resonance. Perhaps this could be improved by directly measuring the lifetime of the  $^{26}\text{Si}$   $3^+$  level. Measurements of the neutron spectroscopic factor of the  $^{26}\text{Mg}$   $J^\pi = 1^+$  mirror state would also be useful to constrain the contribution of this state to the reaction rate. A repetition of the  $^{25}\text{Mg}(d, p)^{26}\text{Mg}$  reaction study [270] at higher energies may be useful to improve the direct to compound nuclear component of the cross section.

This discussion of the reaction rate uncertainties assumes that we have a good understanding of the  $^{26}\text{Si}$  level structure. There are a number of open questions, however, that stretch our ability to make this claim. For instance if the 5928/5890 keV states are indeed a  $3^+/0^+$  doublet, why was the 5928 keV state populated so strongly in the  $^{28}\text{Si}(p, t)^{26}\text{Si}$  reaction [258], while the  $0^+$  state was populated so weakly? One would expect natural parity states to be populated much more strongly. Note that in [258], the 5928 keV state was labeled as 5916 keV as a result of the uncertain calibration of lower-lying levels [273], and it would be worthwhile to revisit the data from that measurement in light of the more precise energy measurements currently available. Another question is why is the 5890 keV  $0^+$  state so readily observable in the  $^{24}\text{Mg}(^3\text{He}, n\gamma)^{26}\text{Si}$  studies [266, 268, 269, 271], but no neutrons were observed populating the state in the  $^{24}\text{Mg}(^3\text{He}, n)^{26}\text{Si}$  measurement [261], which seemingly had the resolution to observe it? Finally, the question as to whether we are seeing too many  $0^+$  levels and the assertion in [263] of a missing  $1^-$  level clearly strains our ability to claim complete knowledge of the relevant  $^{26}\text{Si}$  level structure.

### 3.5. Other reactions affecting the $^{26}\text{Al}$ abundance

The sensitivity study by Iliadis *et al* [241] identified a number of other reactions that, while not direct producing or destroying  $^{26}\text{Al}$ , do affect its final abundance in massive stars. The most influential are the  $^{25}\text{Mg}(\alpha, n)^{28}\text{Si}$ , the  $^{23}\text{Na}(\alpha, p)^{26}\text{Mg}$ , and the neutron capture reactions

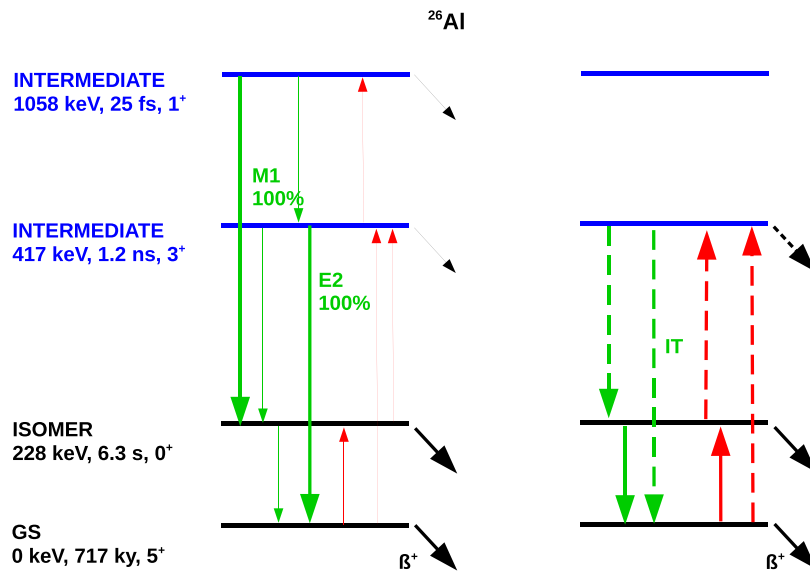


**Figure 14.** The large number of transitions to and from short-lived, intermediate states that become available in stellar environments (left side) are being simplified by only explicitly calculating the coupling rates between all long-lived states, but including the effect the short-lived states have on them (right side). The dashed lines indicate the additionally calculated rates if the  $3^+$  state is considered as long-lived as well, which might be relevant in certain scenarios.

$^{24}\text{Mg}(n, \gamma)^{25}\text{Mg}$  and  $^{25}\text{Mg}(n, \gamma)^{26}\text{Mg}$ . We discuss these reactions separately in the sections below.

**3.5.1.  $^{25}\text{Mg}(\alpha, n)^{28}\text{Si}$ .** The  $^{25}\text{Mg}(\alpha, n)^{28}\text{Si}$  reaction is most influential during explosive Ne/C-shell burning, at a temperature around 2.3 GK ( $E_{\text{cm}} = 1.8\text{--}3.5$  MeV). It acts as a neutron source for the neutron-induced reactions described above, as well as reducing the  $^{25}\text{Mg}$  available for proton capture to  $^{26}\text{Al}$ .

The reaction rate currently reported in REACLIB [274] comes from the NACRE compilation [229]. Above 2 GK, the rate comes from Hauser–Feshbach calculations and below this temperature it is based on the direct measurements of Van der Zwan and Geiger [275], Anderson *et al* [276] and Wieland [277]. Between 0.86 and 3 MeV, only the Wieland data are used, even though this work is unpublished. However, Iliadis *et al* [241] questioned both the decision to use HF rates above 2 GK, as experimental data are available, and the exclusion of the Anderson *et al* [276] data. They further recommended a reanalysis of the available data as well as a new measurement. Several new measurements have been made at both Notre Dame and Argonne, and these data are currently under analysis.

**3.5.2.  $^{23}\text{Na}(\alpha, p)^{26}\text{Mg}$ .** The  $^{23}\text{Na}(\alpha, p)^{26}\text{Mg}$  reaction is thought to be influential during convective shell carbon/neon burning at temperatures around 1.4 GK [278]. It is the second most important reaction after  $^{12}\text{C}(^{12}\text{C}, p)^{23}\text{Na}$  for production of protons, which are subsequently captured by  $^{25}\text{Mg}$ .

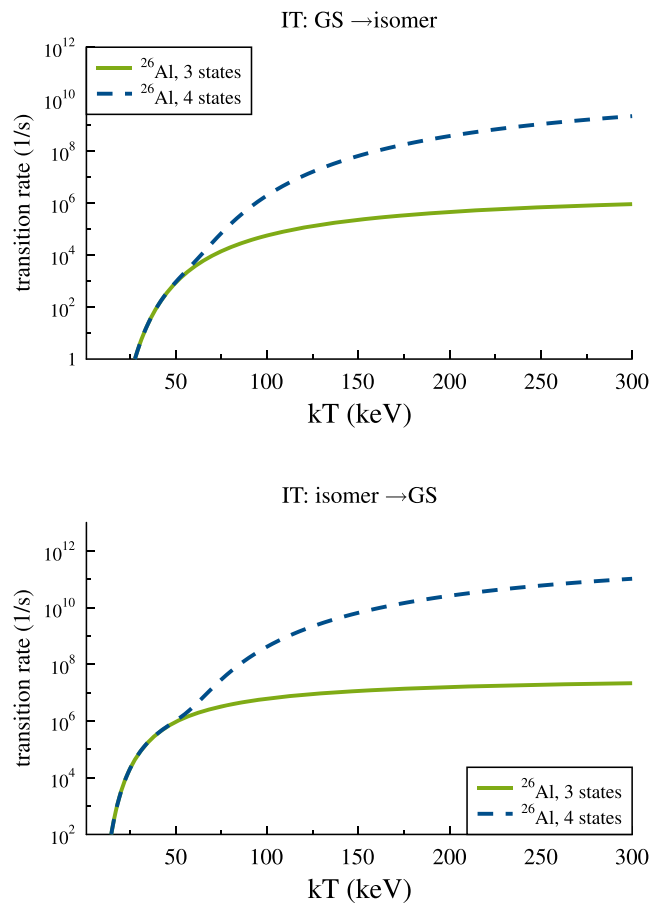


**Figure 15.** Effective coupling rates between the two long-lived states of  $^{26}\text{Al}$  under stellar conditions. Increasing the number of states above the isomer to be considered in the calculation as possible bypass paths from one (green) to two (blue) shows good agreement for the transition rates from ground state to isomer (top panel) and isomer to ground state (bottom panel) at lower energies. At  $\sim 50$  keV, the calculated rates start to diverge.

Four direct measurements of this reaction cross section have recently been performed, three in inverse kinematics [239, 279, 280] and one in forward kinematics [281]. The work of Almaraz-Calderon *et al* [239] used a  $^{23}\text{Na}$  beam on a cryogenic  $^4\text{He}$  target, and detected protons between 6.8 and 13.5 deg in the laboratory. Angle-integrated cross sections were reported for the  $p_0$  and  $p_1$  channels. Tomlinson *et al* [279] also utilised a  $^{23}\text{Na}$  beam on a  $^4\text{He}$  target, this time at room temperature. Angle-integrated cross sections were given for the  $p_0$ – $p_2$  channels. Avila *et al* [280] used the active target detector, MUSIC, to determine total cross sections. Finally, the forward kinematics measurement of Howard *et al* [281] extracted angular distributions for the  $p_0$  and  $p_1$  proton channels. All measurements were consistent with the Non-Smoker [282] cross sections above 1.75 MeV in the centre of mass. Finally, Hubbard *et al* [283] corrected the cross sections from Almaraz-Calderon *et al* [239] and

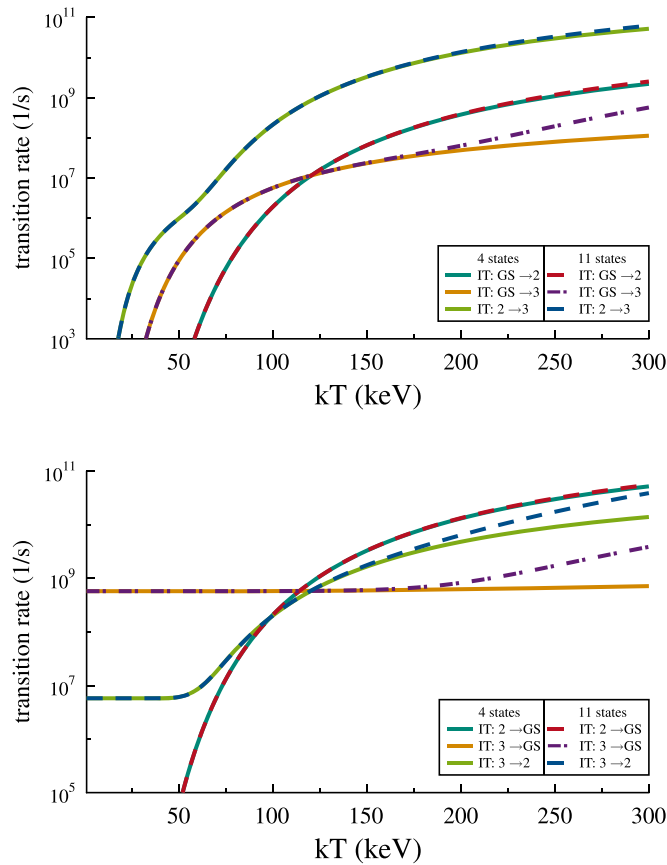


**Figure 16.** Effective coupling rates between the two long-lived states and the short-lived isomer (third level in figure 14) for upward (top panel) and downward (bottom panel) transitions between the long-lived states. The differences in calculated rates are much smaller and occur at higher temperatures.

Tomlinson *et al* [279] to account for the proton angular distributions measured by Howard *et al* [281] and calculated a new combined rate with a total uncertainty of 30% for temperatures relevant to  $^{26}\text{Al}$  production. This reaction rate is now considered to be sufficiently well constrained for this purpose.

**3.5.3.  $^{24}\text{Mg}(n, \gamma)^{25}\text{Mg}$  and  $^{25}\text{Mg}(n, \gamma)^{26}\text{Mg}$ .** Iliadis *et al* [278] identified the  $^{24}\text{Mg}(n, \gamma)$  reaction as the most important radiative neutron capture reaction impacting  $^{26}\text{Al}$  abundances. For example, during explosive C/Ne burning a 2 times higher  $^{24}\text{Mg}(n, \gamma)$  rate is predicted to yield a change in  $^{26}\text{Al}$  abundance by a factor 1.6. Moreover, a correct interpretation of isotopic ratios in stardust spinel grains, which contain both Mg and Al (section 1.4), requires an accurate  $^{25}\text{Mg}(n, \gamma)^{26}\text{Mg}$  reaction cross section as both this reaction and the  $^{26}\text{Al}$  decay lead to the production of  $^{26}\text{Mg}$ .

The Maxwellian-averaged cross sections (MACS) for these reactions were recommended by the Karlsruhe Astrophysical Database of Nucleosynthesis in Stars



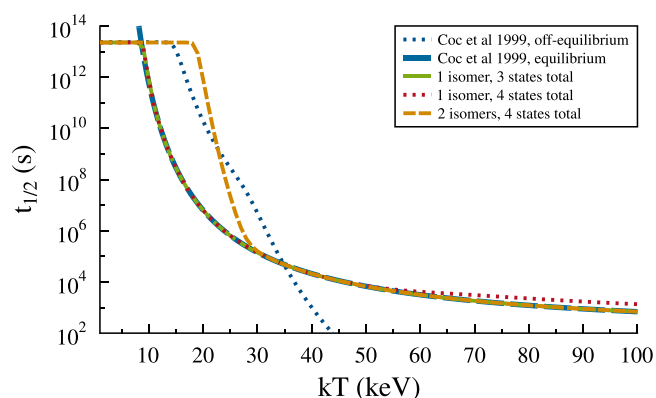


**Figure 17.** Effective half-lives of  $^{26}\text{Al}$  for different numbers of isomeric states and total states. Setting the cutoff time for which to explicitly treat a state as an isomer to  $1\text{ns}$  adds a short-lived isomeric state (third level in figure 14) to the network.

(KADoNiS) [284], quoting Maxwellian-averaged neutron capture cross sections with large uncertainties. These MACS values are based on one measurement from the 1970s [285]. Recently, high precision measurements of neutron capture on Mg isotopes have been performed at the n\_TOF facility at CERN [286, 287]. In [286], resonance energies, spins and partial widths are presented for resonances in the  $^{24}\text{Mg}(n, \gamma)$  reaction up to neutron energies of about 660 keV. By using the cross section reconstructed from these resonance parameters obtained in the resolved resonance region (RRR) and the small contribution to the cross section data from evaluations at higher energy, i.e. in the unresolved resonance region (URR) [288], it was possible to determine a reliable MACS up to about  $kT = 300$  keV, which corresponds to stellar temperatures of 3.6 GK, covering the neutron energy range of interest for  $^{26}\text{Al}$  synthesis. The results for different temperatures not given in [286] are listed in table 6, including the contribution of p-wave direct radiative capture [289].

#### 4. Decay rate of $^{26}\text{Al}$ in stellar environments

While the reaction rates for the production and destruction of both  $^{26g}\text{Al}$  and  $^{26m}\text{Al}$  can be experimentally determined in terrestrial settings (section 3), they do not adequately reflect the interplay of the two states in a stellar environment. The Maxwellian temperature distribution in these scenarios leads to possible shifts in the isomeric and ground state abundance distribution via thermally excited, short-lived states (figure 14). Such a change in the final abundances would, among other effects, have direct implications for  $\gamma$ -ray observations as described in section 1.1. As alluded to in section 3, stellar nucleosynthesis codes can reproduce this behavior by treating the ground and isomeric states as two independent species, and modifying their respective transition, reaction and decay rates. The exact calculation of the rates shown in this work is explained in further detail in [290].

The distribution into the excited states, and thus the calculated transition and decay rates, are highly temperature dependent. This applies to both the rates themselves, and to the

number of short-lived states that need to be considered depending on the maximum temperature of the specific astrophysical scenario. Figure 15 compares the cases of calculating the transition rates between the ground state and isomeric state by considering either just the short-lived state at 417 keV (system of 3 states), or both states at 417 and 1058 keV (see figure 14). While the transition rates agree for lower energies, a noticeable difference can be seen above temperatures of  $\sim 50$  keV. This illustrates the importance of considering the specific case for which such a rate will be used, and the upper temperature limits of achieving accurate rates with less complex systems of considered states. *However, as a rule of thumb, the more complex system will never be less accurate in itself, given accurate input parameters.*

Additionally, and probably less obviously, the categorization into long- and short-lived states is not static, either, but depends on the stellar scenario and average time-stepping of the nucleosynthesis code describing it. In the case of  $^{26}\text{Al}$ , there is the established isomeric  $0^+$  state at 228 keV; but for extreme cases, the  $3^+$  state at 417 keV with  $t_{1/2} = 1.2$  ns could be considered as an isomeric state as well and be treated explicitly, changing the resulting reaction and transition rates, as illustrated in figure 16. Note that the two systems being compared contain four and eleven states here, since the case of three states in figure 15 would now not contain any short-lived states as bypass paths, but rather be just a static system. While there are branchings in the calculated rates here as well, those occur at much higher temperatures, are smaller in magnitude, and are based on an extreme case to begin with. One can therefore assume that the system with just one isomeric state and four states in total already leads to accurate rates for most scenarios.

Both ground and isomeric states of  $^{26}\text{Al}$  decay almost exclusively to  $^{26}\text{Mg}$  via positron emission. Their individual decay rates are not affected by temperature, however, the average lifetime of the nucleus is influenced by the changes in distribution between energetic states with different decay rates. Coc *et al* [291] compared the *effective half-life*, derived from the same general approach as the one described above, with the half-life calculated from analytical off-equilibrium and equilibrium decay rates, see figure 17.

Note that these *effective half-lives* are only a theoretical concept and do not correlate with actual transition rates that might be usable in a stellar model. In order to generate those, one would have to first set the correct parameters for the specific stellar model, mainly the cutoff energy as determined by the maximum temperature of the star, and the time cutoff leading to the number of states to be considered long-lived, which is based on the shortest time-step of the model in question.

The difference in *effective half-life* in the temperature region between 10 and 30 keV, depending on the exact set of input parameters chosen, underlines the importance of considering both the temperature regime and time-stepping of the stellar scenario to produce and use the appropriate rates.

## 5. Summary and conclusions

We have reviewed the astrophysical importance of  $^{26}\text{Al}$ , as demonstrated by the many different types of astrophysical problems that sprang from the variety of  $^{26}\text{Al}$  observations. We have described how  $^{26}\text{Al}$  is produced by proton captures on the stable  $^{25}\text{Mg}$  in a variety of different astrophysical environments, where destruction paths via proton and neutron captures as well as by-passes can also be activated hindering its production. Finally, we have detailed the nuclear properties of  $^{26}\text{Al}$  and the nuclear reactions that affect its production in the

**Table 7.** Summary of reactions and relevant sites. Temperatures refer to the site listed and do not necessarily represent the optimum temperature for  $^{26}\text{Al}$  production.

Reaction	Relevant sites	$T$ (GK)
$^{25}\text{Mg}(p, \gamma)^{26}\text{Al}$	Low- and intermediate-mass AGB stars	0.06–0.1
	Hydrostatic H-core burning in massive stars	0.03–0.08
	Hydrostatic C-shell burning in massive stars	0.8–1.2
	Explosive Ne/C-shell burning in massive stars	1.9–2.8
	Novae	0.2–0.4
$^{26}\text{Al}(p, \gamma)^{27}\text{Si}$	Intermediate-mass AGB stars	0.06–0.1
	Hydrostatic H-core burning in massive stars	0.03–0.08
	Novae	0.2–0.4
$^{26}\text{Al} + n$	Low- and intermediate-mass AGB stars	0.2–0.4
	Hydrostatic C-shell burning in massive stars	0.8–1.2
	Explosive Ne/C-shell burning in massive stars	1.9–2.8
$^{25}\text{Al}(p, \gamma)^{26}\text{Si}$	Novae	0.2–0.4
$^{25}\text{Mg}(\alpha, n)^{28}\text{Si}$	Explosive Ne/C-shell burning in massive stars	1.9–2.8
$^{23}\text{Na}(\alpha, p)^{26}\text{Mg}$	Hydrostatic C-shell burning in massive stars	0.8–1.2
$^{24}\text{Mg}(n, \gamma)^{25}\text{Mg}$	Hydrostatic C-shell burning in massive stars	0.8–1.2
$^{25}\text{Mg}(n, \gamma)^{26}\text{Mg}$	Explosive Ne/C-shell burning in massive stars	1.9–2.8

different stellar sites. In table 7 we collect the relevant reactions, their sites and the temperatures.

In summary, astrophysical observations of live  $^{26}\text{Al}$  include its presence in the Milky Way Galaxy, observed by satellite telescopes using  $\gamma$ -ray spectrometers that can detect the 1.8 MeV photons produced by its decay, and potentially in terrestrial archives. The latter is, however, difficult to disentangle from the  $^{26}\text{Al}$  produced locally via spallation reactions. It is expected that future MeV  $\gamma$ -ray missions based on more advanced detector technology with unprecedented line sensitivity [2] will provide us further unique constraints from  $^{26}\text{Al}$  on the physics of CCSNe and how material is distributed in star-forming regions and transported in the Galaxy. Astrophysical observations of extinct  $^{26}\text{Al}$  come from meteoritic inclusions via measuring in the laboratory excesses in its daughter nucleus  $^{26}\text{Mg}$ . These samples include both stardust grains, which formed in stars and supernovae, and the first solids that formed in the early Solar System (the calcium-aluminum-rich inclusions, CAIs). The presence of  $^{26}\text{Al}$  in the first few Myr of the Solar System's life made an impact on the evolution of the planetesimals from which the terrestrial planets formed. However, we still do not know the origin of such  $^{26}\text{Al}$ , nor if it is a common radioactive nucleus in planet-forming discs in the Galaxy.

Astrophysical observations and their wide implications can only be addressed by understanding how stars and supernovae produce  $^{26}\text{Al}$ . Specifically, massive stars are the most relevant sites to be investigated to interpret the live galactic abundance of  $^{26}\text{Al}$  and its extinct abundance in the early Solar System, given that they are present in star-forming regions. These massive stars eject  $^{26}\text{Al}$  both via winds and by their final CCSN explosions. Stellar rotation and binarity add complexity to the modelling of  $^{26}\text{Al}$  production in these stars and we are still in the process of exploring using 3D modelling nucleosynthetic patterns that move beyond standard current 1D modelling. These range from proton-ingestion episodes to the merger of regions of different composition. AGB stars and novae, instead, produce roughly <10% each of the total amount of  $^{26}\text{Al}$  in the Galaxy, and they are of relevance

**Table 8.** The  $^{25}\text{Mg}(p, \gamma)^{26}\text{Al}$  reaction rate in units of  $\text{cm}^3 \text{mol}^{-1} \text{s}^{-1}$  calculated with the resonance information from table 1. The lower, median and upper rates correspond to the 32%, 50%, and 68% percentiles.

$T$ [GK]	Lower limit	Median rate	Upper limit
0.010	$2.10 \times 10^{-33}$	$3.10 \times 10^{-33}$	$4.67 \times 10^{-33}$
0.011	$1.29 \times 10^{-31}$	$1.79 \times 10^{-31}$	$2.55 \times 10^{-31}$
0.012	$7.04 \times 10^{-30}$	$8.77 \times 10^{-30}$	$1.10 \times 10^{-29}$
0.013	$3.31 \times 10^{-28}$	$4.06 \times 10^{-28}$	$4.98 \times 10^{-28}$
0.014	$1.11 \times 10^{-26}$	$1.37 \times 10^{-26}$	$1.70 \times 10^{-26}$
0.015	$2.49 \times 10^{-25}$	$3.09 \times 10^{-25}$	$3.85 \times 10^{-25}$
0.016	$3.85 \times 10^{-24}$	$4.77 \times 10^{-24}$	$5.94 \times 10^{-24}$
0.018	$3.68 \times 10^{-22}$	$4.55 \times 10^{-22}$	$5.66 \times 10^{-22}$
0.020	$1.39 \times 10^{-20}$	$1.72 \times 10^{-20}$	$2.14 \times 10^{-20}$
0.025	$9.18 \times 10^{-18}$	$1.13 \times 10^{-17}$	$1.40 \times 10^{-17}$
0.030	$6.63 \times 10^{-16}$	$8.17 \times 10^{-16}$	$1.01 \times 10^{-15}$
0.040	$1.35 \times 10^{-13}$	$1.65 \times 10^{-13}$	$2.02 \times 10^{-13}$
0.050	$4.05 \times 10^{-12}$	$4.72 \times 10^{-12}$	$5.54 \times 10^{-12}$
0.060	$5.58 \times 10^{-11}$	$6.26 \times 10^{-11}$	$7.03 \times 10^{-11}$
0.070	$4.42 \times 10^{-10}$	$4.93 \times 10^{-10}$	$5.52 \times 10^{-10}$
0.080	$2.24 \times 10^{-09}$	$2.51 \times 10^{-09}$	$2.82 \times 10^{-09}$
0.090	$8.09 \times 10^{-09}$	$9.08 \times 10^{-09}$	$1.02 \times 10^{-08}$
0.100	$2.29 \times 10^{-08}$	$2.57 \times 10^{-08}$	$2.90 \times 10^{-08}$
0.110	$5.55 \times 10^{-08}$	$6.22 \times 10^{-08}$	$7.00 \times 10^{-08}$
0.120	$1.29 \times 10^{-07}$	$1.45 \times 10^{-07}$	$1.63 \times 10^{-07}$
0.130	$3.47 \times 10^{-07}$	$3.84 \times 10^{-07}$	$4.30 \times 10^{-07}$
0.140	$1.17 \times 10^{-06}$	$1.29 \times 10^{-06}$	$1.43 \times 10^{-06}$
0.150	$4.34 \times 10^{-06}$	$4.80 \times 10^{-06}$	$5.31 \times 10^{-06}$
0.160	$1.54 \times 10^{-05}$	$1.71 \times 10^{-05}$	$1.89 \times 10^{-05}$
0.180	$1.41 \times 10^{-04}$	$1.57 \times 10^{-04}$	$1.73 \times 10^{-04}$
0.200	$8.55 \times 10^{-04}$	$9.48 \times 10^{-04}$	$1.05 \times 10^{-03}$
0.250	$2.19 \times 10^{-02}$	$2.41 \times 10^{-02}$	$2.66 \times 10^{-02}$
0.300	$1.88 \times 10^{-01}$	$2.07 \times 10^{-01}$	$2.27 \times 10^{-01}$
0.350	$8.75 \times 10^{-01}$	$9.54 \times 10^{-01}$	$1.04 \times 10^{+00}$
0.400	$2.77 \times 10^{+00}$	$3.00 \times 10^{+00}$	$3.26 \times 10^{+00}$
0.450	$6.80 \times 10^{+00}$	$7.33 \times 10^{+00}$	$7.90 \times 10^{+00}$
0.500	$1.40 \times 10^{+01}$	$1.50 \times 10^{+01}$	$1.60 \times 10^{+01}$
0.600	$4.09 \times 10^{+01}$	$4.35 \times 10^{+01}$	$4.63 \times 10^{+01}$
0.700	$8.75 \times 10^{+01}$	$9.25 \times 10^{+01}$	$9.78 \times 10^{+01}$

predominantly for the study of the origin of extinct  $^{26}\text{Al}$  in stardust grains. Mixing and mass loss are the major uncertainties related to their modelling. In all the sites we discussed here, nuclear reaction uncertainties play a major role in the final estimate of the  $^{26}\text{Al}$  yields.

Significant progress has been made experimentally in constraining the nuclear reaction rates that determine the abundance of  $^{26}\text{Al}$  in the astrophysical sites discussed in this review. The  $^{25}\text{Mg}(p, \gamma)^{26}\text{Al}$  reaction is the main production reaction in all the sites discussed. The key resonances at 93, 191, and 305 keV have been measured directly, but confirmation of the 93 keV strength would be useful. The 59 keV resonance dominates at temperatures below 0.05 GK (core H-burning in massive stars), but has remained inaccessible to direct measurements. The destruction route of the  $^{26}\text{Al}$  ground state via proton capture has also been studied

**Table 9.** The  $^{25}\text{Mg}(p, \gamma)^{26}\text{Al}_m$  reaction rate in units of  $\text{cm}^3 \text{mol}^{-1} \text{s}^{-1}$  calculated with the resonance information from table 1. The lower, median and upper rates correspond to the 32%, 50%, and 68% percentiles.

$T$ [GK]	Lower limit	Median rate	Upper limit
0.010	$5.35 \times 10^{-34}$	$8.21 \times 10^{-34}$	$1.28 \times 10^{-33}$
0.011	$3.17 \times 10^{-32}$	$4.60 \times 10^{-32}$	$6.86 \times 10^{-32}$
0.012	$1.62 \times 10^{-30}$	$2.14 \times 10^{-30}$	$2.86 \times 10^{-30}$
0.013	$7.11 \times 10^{-29}$	$9.42 \times 10^{-29}$	$1.26 \times 10^{-28}$
0.014	$2.30 \times 10^{-27}$	$3.13 \times 10^{-27}$	$4.27 \times 10^{-27}$
0.015	$5.08 \times 10^{-26}$	$7.01 \times 10^{-26}$	$9.65 \times 10^{-26}$
0.016	$7.82 \times 10^{-25}$	$1.08 \times 10^{-24}$	$1.49 \times 10^{-24}$
0.018	$7.46 \times 10^{-23}$	$1.03 \times 10^{-22}$	$1.42 \times 10^{-22}$
0.020	$2.82 \times 10^{-21}$	$3.89 \times 10^{-21}$	$5.37 \times 10^{-21}$
0.025	$1.86 \times 10^{-18}$	$2.56 \times 10^{-18}$	$3.53 \times 10^{-18}$
0.030	$1.35 \times 10^{-16}$	$1.85 \times 10^{-16}$	$2.55 \times 10^{-16}$
0.040	$2.98 \times 10^{-14}$	$3.94 \times 10^{-14}$	$5.27 \times 10^{-14}$
0.050	$1.20 \times 10^{-12}$	$1.43 \times 10^{-12}$	$1.74 \times 10^{-12}$
0.060	$2.10 \times 10^{-11}$	$2.43 \times 10^{-11}$	$2.83 \times 10^{-11}$
0.070	$1.87 \times 10^{-10}$	$2.17 \times 10^{-10}$	$2.54 \times 10^{-10}$
0.080	$9.97 \times 10^{-10}$	$1.17 \times 10^{-09}$	$1.37 \times 10^{-09}$
0.090	$3.69 \times 10^{-09}$	$4.33 \times 10^{-09}$	$5.08 \times 10^{-09}$
0.100	$1.05 \times 10^{-08}$	$1.23 \times 10^{-08}$	$1.45 \times 10^{-08}$
0.110	$2.52 \times 10^{-08}$	$2.94 \times 10^{-08}$	$3.44 \times 10^{-08}$
0.120	$5.45 \times 10^{-08}$	$6.34 \times 10^{-08}$	$7.39 \times 10^{-08}$
0.130	$1.18 \times 10^{-07}$	$1.36 \times 10^{-07}$	$1.58 \times 10^{-07}$
0.140	$2.91 \times 10^{-07}$	$3.30 \times 10^{-07}$	$3.80 \times 10^{-07}$
0.150	$8.37 \times 10^{-07}$	$9.40 \times 10^{-07}$	$1.07 \times 10^{-06}$
0.160	$2.57 \times 10^{-06}$	$2.89 \times 10^{-06}$	$3.28 \times 10^{-06}$
0.180	$2.14 \times 10^{-05}$	$2.41 \times 10^{-05}$	$2.72 \times 10^{-05}$
0.200	$1.28 \times 10^{-04}$	$1.44 \times 10^{-04}$	$1.63 \times 10^{-04}$
0.250	$3.47 \times 10^{-03}$	$3.86 \times 10^{-03}$	$4.31 \times 10^{-03}$
0.300	$3.22 \times 10^{-02}$	$3.54 \times 10^{-02}$	$3.91 \times 10^{-02}$
0.350	$1.60 \times 10^{-01}$	$1.74 \times 10^{-01}$	$1.91 \times 10^{-01}$
0.400	$5.34 \times 10^{-01}$	$5.79 \times 10^{-01}$	$6.31 \times 10^{-01}$
0.450	$1.37 \times 10^{+00}$	$1.48 \times 10^{+00}$	$1.60 \times 10^{+00}$
0.500	$2.90 \times 10^{+00}$	$3.13 \times 10^{+00}$	$3.38 \times 10^{+00}$
0.600	$8.94 \times 10^{+00}$	$9.59 \times 10^{+00}$	$1.03 \times 10^{+01}$
0.700	$1.98 \times 10^{+01}$	$2.12 \times 10^{+01}$	$2.27 \times 10^{+01}$

directly at temperatures above around 0.1 GK. However, the strength of the 128 keV resonance, which dominates at lower temperatures, is still not well known and represents a high priority for future direct measurements. Proton capture on the  $^{26}\text{Al}$  isomeric state is much weaker than on the ground state and not considered significant in most stellar sites. For the destruction reactions through neutron capture, discrepancies between existing data at low neutron energy have been largely resolved. Additional data at higher neutron energies up to about 500 keV, relevant for  $^{26}\text{Al}$  destruction in massive stars are still needed. The  $^{25}\text{Al}(p, \gamma)$  by-pass reaction has been constrained through transfer studies of the relevant level

**Table 10.** The  $^{26}\text{Al}(p, \gamma)^{27}\text{Si}$  reaction rate in units of  $\text{cm}^3 \text{mol}^{-1} \text{s}^{-1}$  calculated with the resonance information from table 2. The lower, median and upper rates correspond to the 32%, 50%, and 68% percentiles.

$T$ [GK]	Lower limit	Median rate	Upper limit
0.010	$2.96 \times 10^{-37}$	$4.35 \times 10^{-37}$	$6.38 \times 10^{-37}$
0.011	$8.04 \times 10^{-36}$	$1.18 \times 10^{-35}$	$1.74 \times 10^{-35}$
0.012	$1.51 \times 10^{-34}$	$2.20 \times 10^{-34}$	$3.22 \times 10^{-34}$
0.013	$2.11 \times 10^{-33}$	$3.08 \times 10^{-33}$	$4.49 \times 10^{-33}$
0.014	$2.42 \times 10^{-32}$	$3.58 \times 10^{-32}$	$5.44 \times 10^{-32}$
0.015	$2.35 \times 10^{-31}$	$3.75 \times 10^{-31}$	$7.13 \times 10^{-31}$
0.016	$1.97 \times 10^{-30}$	$3.74 \times 10^{-30}$	$1.19 \times 10^{-29}$
0.018	$9.41 \times 10^{-29}$	$3.97 \times 10^{-28}$	$2.25 \times 10^{-27}$
0.020	$3.22 \times 10^{-27}$	$2.61 \times 10^{-26}$	$1.63 \times 10^{-25}$
0.025	$4.74 \times 10^{-24}$	$5.55 \times 10^{-23}$	$3.58 \times 10^{-22}$
0.030	$1.18 \times 10^{-21}$	$9.34 \times 10^{-21}$	$5.80 \times 10^{-20}$
0.040	$4.37 \times 10^{-17}$	$7.03 \times 10^{-17}$	$1.17 \times 10^{-16}$
0.050	$4.62 \times 10^{-14}$	$7.04 \times 10^{-14}$	$1.07 \times 10^{-13}$
0.060	$5.08 \times 10^{-12}$	$7.58 \times 10^{-12}$	$1.13 \times 10^{-11}$
0.070	$1.48 \times 10^{-10}$	$2.15 \times 10^{-10}$	$3.14 \times 10^{-10}$
0.080	$2.00 \times 10^{-09}$	$2.78 \times 10^{-09}$	$3.92 \times 10^{-09}$
0.090	$1.69 \times 10^{-08}$	$2.26 \times 10^{-08}$	$3.03 \times 10^{-08}$
0.100	$1.04 \times 10^{-07}$	$1.35 \times 10^{-07}$	$1.75 \times 10^{-07}$
0.110	$4.98 \times 10^{-07}$	$6.35 \times 10^{-07}$	$8.11 \times 10^{-07}$
0.120	$1.94 \times 10^{-06}$	$2.45 \times 10^{-06}$	$3.12 \times 10^{-06}$
0.130	$6.34 \times 10^{-06}$	$8.00 \times 10^{-06}$	$1.02 \times 10^{-05}$
0.140	$1.80 \times 10^{-05}$	$2.27 \times 10^{-05}$	$2.86 \times 10^{-05}$
0.150	$4.58 \times 10^{-05}$	$5.70 \times 10^{-05}$	$7.15 \times 10^{-05}$
0.160	$1.06 \times 10^{-04}$	$1.30 \times 10^{-04}$	$1.61 \times 10^{-04}$
0.180	$4.53 \times 10^{-04}$	$5.43 \times 10^{-04}$	$6.55 \times 10^{-04}$
0.200	$1.57 \times 10^{-03}$	$1.82 \times 10^{-03}$	$2.13 \times 10^{-03}$
0.250	$1.87 \times 10^{-02}$	$2.05 \times 10^{-02}$	$2.27 \times 10^{-02}$
0.300	$1.21 \times 10^{-01}$	$1.30 \times 10^{-01}$	$1.40 \times 10^{-01}$
0.350	$5.07 \times 10^{-01}$	$5.44 \times 10^{-01}$	$5.82 \times 10^{-01}$
0.400	$1.55 \times 10^{+00}$	$1.67 \times 10^{+00}$	$1.79 \times 10^{+00}$
0.450	$3.76 \times 10^{+00}$	$4.05 \times 10^{+00}$	$4.36 \times 10^{+00}$
0.500	$7.65 \times 10^{+00}$	$8.26 \times 10^{+00}$	$8.93 \times 10^{+00}$
0.600	$2.20 \times 10^{+01}$	$2.39 \times 10^{+01}$	$2.60 \times 10^{+01}$
0.700	$4.64 \times 10^{+01}$	$5.05 \times 10^{+01}$	$5.50 \times 10^{+01}$

information, and the remaining uncertainty is dominated by that of the radiative width of the 415 keV resonance. In relation to the main reactions that indirectly affect the abundance of  $^{26}\text{Al}$ , for the  $^{25}\text{Mg}(\alpha, n)^{28}\text{Si}$  reaction, new measurements have been performed and it is not yet clear whether further data will be needed. Finally, both the  $^{23}\text{Na}(\alpha, p)^{26}\text{Mg}$  and  $^{24}\text{Mg}(n, \gamma)^{25}\text{Mg}$  reactions are now considered sufficiently well constrained across temperatures relevant in massive stars.

**Table 11.** The  $^{26}\text{Al}^m(p, \gamma)^{27}\text{Si}$  reaction rate in units of  $\text{cm}^3 \text{mol}^{-1} \text{s}^{-1}$  calculated with the resonance information from table 3.

$T$ [GK]	Lower limit	Median rate	Upper limit
0.010	$2.81 \times 10^{-37}$	$4.09 \times 10^{-37}$	$6.02 \times 10^{-37}$
0.011	$7.71 \times 10^{-36}$	$1.13 \times 10^{-35}$	$1.64 \times 10^{-35}$
0.012	$1.45 \times 10^{-34}$	$2.12 \times 10^{-34}$	$3.09 \times 10^{-34}$
0.013	$2.01 \times 10^{-33}$	$2.93 \times 10^{-33}$	$4.25 \times 10^{-33}$
0.014	$2.16 \times 10^{-32}$	$3.16 \times 10^{-32}$	$4.55 \times 10^{-32}$
0.015	$1.89 \times 10^{-31}$	$2.74 \times 10^{-31}$	$3.95 \times 10^{-31}$
0.016	$1.37 \times 10^{-30}$	$1.98 \times 10^{-30}$	$2.87 \times 10^{-30}$
0.018	$4.51 \times 10^{-29}$	$6.51 \times 10^{-29}$	$9.37 \times 10^{-29}$
0.020	$8.95 \times 10^{-28}$	$1.30 \times 10^{-27}$	$1.87 \times 10^{-27}$
0.025	$3.42 \times 10^{-25}$	$4.99 \times 10^{-25}$	$7.20 \times 10^{-25}$
0.030	$3.22 \times 10^{-23}$	$4.71 \times 10^{-23}$	$6.82 \times 10^{-23}$
0.040	$2.69 \times 10^{-20}$	$3.84 \times 10^{-20}$	$5.50 \times 10^{-20}$
0.050	$4.82 \times 10^{-18}$	$9.89 \times 10^{-18}$	$2.16 \times 10^{-17}$
0.060	$3.00 \times 10^{-16}$	$1.35 \times 10^{-15}$	$4.04 \times 10^{-15}$
0.070	$1.18 \times 10^{-14}$	$6.09 \times 10^{-14}$	$1.86 \times 10^{-13}$
0.080	$3.16 \times 10^{-13}$	$1.20 \times 10^{-12}$	$3.36 \times 10^{-12}$
0.090	$4.56 \times 10^{-12}$	$1.52 \times 10^{-11}$	$3.41 \times 10^{-11}$
0.100	$3.97 \times 10^{-11}$	$1.30 \times 10^{-10}$	$2.52 \times 10^{-10}$
0.110	$2.41 \times 10^{-10}$	$7.58 \times 10^{-10}$	$1.60 \times 10^{-09}$
0.120	$1.11 \times 10^{-09}$	$3.36 \times 10^{-09}$	$8.34 \times 10^{-09}$
0.130	$4.23 \times 10^{-09}$	$1.25 \times 10^{-08}$	$3.50 \times 10^{-08}$
0.140	$1.37 \times 10^{-08}$	$4.08 \times 10^{-08}$	$1.21 \times 10^{-07}$
0.150	$3.91 \times 10^{-08}$	$1.19 \times 10^{-07}$	$3.58 \times 10^{-07}$
0.160	$1.04 \times 10^{-07}$	$3.16 \times 10^{-07}$	$9.29 \times 10^{-07}$
0.180	$7.30 \times 10^{-07}$	$1.84 \times 10^{-06}$	$4.79 \times 10^{-06}$
0.200	$5.50 \times 10^{-06}$	$1.03 \times 10^{-05}$	$2.09 \times 10^{-05}$
0.250	$3.74 \times 10^{-04}$	$5.71 \times 10^{-04}$	$8.63 \times 10^{-04}$
0.300	$7.70 \times 10^{-03}$	$1.20 \times 10^{-02}$	$1.88 \times 10^{-02}$
0.350	$6.99 \times 10^{-02}$	$1.10 \times 10^{-01}$	$1.74 \times 10^{-01}$
0.400	$3.63 \times 10^{-01}$	$5.71 \times 10^{-01}$	$9.06 \times 10^{-01}$
0.450	$1.28 \times 10^{+00}$	$2.02 \times 10^{+00}$	$3.21 \times 10^{+00}$
0.500	$3.47 \times 10^{+00}$	$5.48 \times 10^{+00}$	$8.70 \times 10^{+00}$
0.600	$1.49 \times 10^{+01}$	$2.36 \times 10^{+01}$	$3.74 \times 10^{+01}$
0.700	$4.10 \times 10^{+01}$	$6.47 \times 10^{+01}$	$1.03 \times 10^{+02}$

In conclusion, the radioisotope  $^{26}\text{Al}$  provides us with a wealth of information about the Galaxy, its stars and supernovae as well as the early Solar System. Many of the influential reactions are, or will shortly be, sufficiently constrained and we have summarised above the remaining experimental priorities. Further sensitivity studies, based on the latest rates, such as those newly calculated rates here and using up-to-date stellar models, are required to evaluate the impact of these remaining uncertainties. Future work will also need to investigate if more reactions than those considered here may have an impact on the production of  $^{26}\text{Al}$  in CCSN explosions.

**Table 12.** The  $^{25}\text{Al}(p, \gamma)^{26}\text{Si}$  reaction rate in units of  $\text{cm}^3 \text{mol}^{-1} \text{s}^{-1}$  calculated with the resonance information from table 5.

$T$ [GK]	Lower limit	Median rate	Upper limit
0.010	$9.91 \times 10^{-38}$	$1.46 \times 10^{-37}$	$2.13 \times 10^{-37}$
0.011	$2.72 \times 10^{-36}$	$3.99 \times 10^{-36}$	$5.87 \times 10^{-36}$
0.012	$5.11 \times 10^{-35}$	$7.48 \times 10^{-35}$	$1.10 \times 10^{-34}$
0.013	$7.04 \times 10^{-34}$	$1.03 \times 10^{-33}$	$1.51 \times 10^{-33}$
0.014	$7.42 \times 10^{-33}$	$1.09 \times 10^{-32}$	$1.60 \times 10^{-32}$
0.015	$6.38 \times 10^{-32}$	$9.32 \times 10^{-32}$	$1.37 \times 10^{-31}$
0.016	$4.57 \times 10^{-31}$	$6.68 \times 10^{-31}$	$9.79 \times 10^{-31}$
0.018	$1.46 \times 10^{-29}$	$2.13 \times 10^{-29}$	$3.13 \times 10^{-29}$
0.020	$2.90 \times 10^{-28}$	$4.24 \times 10^{-28}$	$6.29 \times 10^{-28}$
0.025	$1.16 \times 10^{-25}$	$1.69 \times 10^{-25}$	$2.48 \times 10^{-25}$
0.030	$1.12 \times 10^{-23}$	$1.62 \times 10^{-23}$	$2.37 \times 10^{-23}$
0.040	$8.59 \times 10^{-21}$	$1.25 \times 10^{-20}$	$1.84 \times 10^{-20}$
0.050	$1.23 \times 10^{-18}$	$1.85 \times 10^{-18}$	$2.68 \times 10^{-18}$
0.060	$6.79 \times 10^{-17}$	$1.73 \times 10^{-16}$	$4.42 \times 10^{-16}$
0.070	$1.84 \times 10^{-15}$	$9.33 \times 10^{-15}$	$2.83 \times 10^{-14}$
0.080	$3.01 \times 10^{-14}$	$2.10 \times 10^{-13}$	$6.58 \times 10^{-13}$
0.090	$3.00 \times 10^{-13}$	$2.37 \times 10^{-12}$	$7.53 \times 10^{-12}$
0.100	$1.99 \times 10^{-12}$	$1.63 \times 10^{-11}$	$5.22 \times 10^{-11}$
0.110	$9.48 \times 10^{-12}$	$7.85 \times 10^{-11}$	$2.52 \times 10^{-10}$
0.120	$3.50 \times 10^{-11}$	$2.87 \times 10^{-10}$	$9.23 \times 10^{-10}$
0.130	$1.13 \times 10^{-10}$	$8.62 \times 10^{-10}$	$2.75 \times 10^{-09}$
0.140	$3.78 \times 10^{-10}$	$2.26 \times 10^{-09}$	$7.02 \times 10^{-09}$
0.150	$1.55 \times 10^{-09}$	$5.68 \times 10^{-09}$	$1.62 \times 10^{-08}$
0.160	$6.90 \times 10^{-09}$	$1.56 \times 10^{-08}$	$3.65 \times 10^{-08}$
0.180	$1.07 \times 10^{-07}$	$1.65 \times 10^{-07}$	$2.45 \times 10^{-07}$
0.200	$1.07 \times 10^{-06}$	$1.56 \times 10^{-06}$	$2.33 \times 10^{-06}$
0.250	$8.26 \times 10^{-05}$	$1.25 \times 10^{-04}$	$1.93 \times 10^{-04}$
0.300	$1.52 \times 10^{-03}$	$2.32 \times 10^{-03}$	$3.60 \times 10^{-03}$
0.350	$1.19 \times 10^{-02}$	$1.82 \times 10^{-02}$	$2.82 \times 10^{-02}$
0.400	$5.41 \times 10^{-02}$	$8.30 \times 10^{-02}$	$1.29 \times 10^{-01}$
0.450	$1.73 \times 10^{-01}$	$2.65 \times 10^{-01}$	$4.10 \times 10^{-01}$
0.500	$4.30 \times 10^{-01}$	$6.59 \times 10^{-01}$	$1.02 \times 10^{+00}$
0.600	$1.63 \times 10^{+00}$	$2.49 \times 10^{+00}$	$3.86 \times 10^{+00}$
0.700	$4.08 \times 10^{+00}$	$6.25 \times 10^{+00}$	$9.66 \times 10^{+00}$

## Acknowledgments

This paper is based upon work from the ‘ChETEC’ COST Action (CA16117), supported by COST (European Cooperation in Science and Technology) and the National Science Foundation under Grant No. OISE-1927130 (IReNA). AML also acknowledges support from STFC (Science and Technology Facilities Council). PA thanks the trustees and staff of the Claude Leon Foundation for support in the form of a postdoctoral fellowship. MP acknowledges the support of NuGrid, JINA-CEE (NSF Grant PHY-1430152) and STFC (through the University of Hulls Consolidated Grant ST/R000840/1), and ongoing access to *viper*, the University of Hull High Performance Computing Facility. MP acknowledges the support from the ‘Lendület-2014’ Programme of the Hungarian Academy of Sciences










(Hungary). BC acknowledges the support from the ERC Consolidator Grant (Hungary) funding scheme (Project RADIOSTAR, G.A. n. 724 560), the Hungarian Academy of Sciences via the Lendület project LP2014-17, and the National Science Foundation (NSF, USA) under Grant No. PHY-1430152 (JINA Center for the Evolution of the Elements). RR and DK are thankful for support from BMBF 05P19RFFN1 and the European Research Council under the European Unions's Seventh Framework Programme (FP/2007-2013)/ERC Grant Agreement N. 615126. AK acknowledges the funding from the European Unions Horizon 2020 research and innovation program under grant agreement No. 771036 (ERC CoG MAIDEN). DB acknowledges support from the National Science Foundation under grants PHY-2011890 (University of Notre Dame), PHY-1430152 (JINA Center for the Evolution of the Elements), and OISE-1927130 (International Research Network for Nuclear Astrophysics). CLW acknowledges support from the UK Science and Technologies Facilities Council (STFC), projects ST/P004008/1 and ST/M006085/1, and the European Research Council ERC-2015-STG Nr. 677 497. AS acknowledges support from the U.S. Department of Energy through grant DE-FG02-87ER40328 (UM). JJ acknowledges support by the Spanish MINECO Grant PID2020-117252GB-I00, by the E.U. FEDER funds, and by the AGAUR/Generalitat de Catalunya grant SGR-661/2017. Finally, we thank the ChETEC-INFRA project funded from the European Unions Horizon 2020 research and innovation programme under Grant agreement No 101008324.

### Data availability statement

The data that support the findings of this study are available upon reasonable request from the authors.

### ORCID iDs

A M Laird  <https://orcid.org/0000-0003-0423-363X>  
A Kankainen  <https://orcid.org/0000-0003-1082-7602>  
P Adsley  <https://orcid.org/0000-0003-1373-679X>  
R Diehl  <https://orcid.org/0000-0002-8337-9022>  
A Sieverding  <https://orcid.org/0000-0001-8235-5910>  
R J Stancliffe  <https://orcid.org/0000-0002-6972-9655>  
C Massimi  <https://orcid.org/0000-0003-2499-5586>

### References

- [1] Basunia M S and Hurst A M 2016 Nuclear data sheets for  $A = 26$  *Nucl. Data Sheets* **134** 1–148
- [2] Timmes F *et al* 2019 Catching element formation in the act ; the case for a new MeV gamma-ray mission: radionuclide astronomy in the 2020s *BAAS* **51** 2 (<https://arxiv.org/pdf/1902.02915.pdf>)
- [3] Feige J, Wallner A, Altmeyer R, Fifield L K, Golser R, Merchel S, Rugel G, Steier P, Tims S G and Winkler S R 2018 Limits on supernova-associated  $^{60}\text{Fe}/^{26}\text{Al}$  nucleosynthesis ratios from accelerator mass spectrometry measurements of deep-sea sediments *Phys. Rev. Lett.* **121** 221103
- [4] Adams F C 2010 The birth environment of the solar system *ARA&A* **48** 47–85

- [5] Diehl R, Siegert T, Greiner J, Krause M, Kretschmer K, Lang M, Pleintinger M, Strong A W, Weinberger C and Zhang X 2018 INTEGRAL/SPI  $\gamma$ -ray line spectroscopy. Response and background characteristics *A&A* **611** A12
- [6] Lugaro M, Ott U and Kereszturi Á 2018 Radioactive nuclei from cosmochronology to habitability *Progr. Part. Nucl. Phys.* **102** 1–47
- [7] Lugaro M *et al* 2017 Origin of meteoritic stardust unveiled by a revised proton-capture rate of  $^{17}\text{O}$  *Nat. Astron.* **1** 0027
- [8] Adsley P *et al* 2021 Reevaluation of the  $^{22}\text{Ne}(\alpha, \gamma)^{26}\text{Mg}$  and  $^{22}\text{Ne}(\alpha, n)^{25}\text{Mg}$  reaction rates *Phys. Rev. C* **103** 015805
- [9] Iliadis C, Champagne A, Chieffi A and Limongi M 2011 The effects of thermonuclear reaction rate variations on  $^{26}\text{Al}$  production in massive stars: a sensitivity study *Astrophys. J. Suppl. Ser.* **193** 16
- [10] Diehl R *et al* 2021 The radioactive nuclei  $^{26}\text{Al}$  and  $^{60}\text{Fe}$  in the Cosmos and in the solar system *PASA* **38** e062
- [11] Merrill S P W 1952 Spectroscopic observations of stars of class S *Astrophys. J.* **116** 21–6
- [12] Lingenfelter R E and Ramaty R 1978 Gamma-ray lines—a new window to the Universe *Phys. Today* **31** 40–7
- [13] Mahoney W A, Ling J C, Jacobson A S and Lingenfelter R E 1982 Diffuse galactic gamma-ray line emission from nucleosynthetic Fe-60, Al-26, and Na-22—preliminary limits from HEAO 3 *Astrophys. J.* **262** 742–48
- [14] Plüschke S *et al* 2001 The COMPTEL 1.809 MeV survey *Exploring the Gamma-Ray Universe* ed A Gimenez *et al* vol 459 (ESA Special Publication) pp 55–8
- [15] Prantzos N and Diehl R 1996 Radioactive  $^{26}\text{Al}$  in the galaxy: observations versus theory *Phys. Rep.* **267** 1–69
- [16] Diehl R *et al* 1995 COMPTEL observations of Galactic  $^{26}\text{Al}$  emission *Astronomy & Astrophysics* **298** 445–460
- [17] Diehl R, Bennett K, Collmar W, Connors A, Denherder J W, Hermsen W, Lichti G G, Lockwood J A, Macri J and McConnell M 1992 Data analysis of the COMPTEL instrument on the NASA gamma ray observatory *NASA Conf. Publ.* **3137** 95–101
- [18] Strong A W *et al* 1992 Maximum entropy imaging and spectral deconvolution for COMPTEL *Data Analysis in Astronomy* ed V di Gesu *et al* (Boston: Springer) pp 251–60
- [19] Knödlseher J, Dixon D, Bennett K, Bloemen H, Diehl R, Hermsen W, Oberlack U, Ryan J, Schönfelder V and von Ballmoos P 1999 Image reconstruction of COMPTEL 1.8 MeV ( $^{26}\text{Al}$ ) AL line data *Astronomy & Astrophysics* **345** 813–25
- [20] Diehl R *et al* 2006 Radioactive  $^{26}\text{Al}$  from massive stars in the Galaxy *Nature* **439** 45–7
- [21] Diehl R, Krause M G H, Kretschmer K, Lang M, Pleintinger M M M, Siegert T, Wang W, Bouchet L and Martin P 2021 Steady-state nucleosynthesis throughout the Galaxy *New Astron. Rev.* **92** 101608
- [22] Krause M G H *et al* 2020 The physics of star cluster formation and evolution *Space Sci. Rev.* **216** 64
- [23] Voss R, Diehl R, Vink J S and Hartmann D H 2010 Probing the evolving massive star population in Orion with kinematic and radioactive tracers *A&A* **520** A51+
- [24] Krause M G H, Burkert A, Diehl R, Fierlinger K, Gaczkowski B, Kroell D, Ngoumou J, Roccatagliata V, Siegert T and Preibisch T 2018 Surround and Squash: the impact of superbubbles on the interstellar medium in Scorpius–Centaurus OB2 *A&A* **619** A120
- [25] Siegert T 2017 Positron-annihilation spectroscopy throughout the milky way *PhD Thesis* TU Munich
- [26] Wallner A *et al* 2016 Recent near-Earth supernovae probed by global deposition of interstellar radioactive  $^{60}\text{Fe}$  *Nature* **532** 69–72
- [27] Breitschwerdt D, Feige J, Schulreich M M, Avillez M A D, Dettbarn C and Fuchs B 2016 The locations of recent supernovae near the Sun from modelling  $^{60}\text{Fe}$  transport *Nature* **532** 73–6
- [28] Wallner A *et al* 2021  $^{60}\text{Fe}$  and  $^{244}\text{Pu}$  deposited on Earth constrain the r-process yields of recent nearby supernovae *Science* **372** 742–5
- [29] Wang W, Siegert T, Dai Z G, Diehl R, Greiner J, Heger A, Krause M, Lang M, Pleintinger M M M and Zhang X L 2020 Gamma-ray emission of  $^{60}\text{Fe}$  and  $^{26}\text{Al}$  radioactivity in our Galaxy *Astrophys. J.* **889** 169
- [30] Sukhbold T, Ertl T, Woosley S E, Brown J M and Janka H T 2016 Core-collapse Supernovae from 9 to 120 solar masses based on neutrino-powered explosions *Astrophys. J.* **821** 38

- [31] Austin S M, West C and Heger A 2017 Reducing uncertainties in the production of the gamma-emitting nuclei  $^{26}\text{Al}$ ,  $^{44}\text{Ti}$ , and  $^{60}\text{Fe}$  in Core-collapse supernovae by using effective helium burning rates *Astrophys. J.* **839** L9
- [32] Jones S W, Möller H, Fryer C L, Fontes C J, Trappitsch R, Even W P, Couture A, Mumpower M R and Safi-Harb S 2019  $^{60}\text{Fe}$  in core-collapse supernovae and prospects for X-ray and gamma-ray detection in supernova remnants *MNRAS* **485** 4287–310
- [33] Lee T, Papanastassiou D A and Wasserburg G J 1977 Aluminum-26 in the early solar system: fossil or fuel? *Astrophys. J.* **211** L107–10
- [34] Wasserburg G J, Busso M, Gallino R and Nollett K M 2006 Short-lived nuclei in the early Solar System: possible AGB sources *Nucl. Phys. A* **777** 5–69
- [35] Vescovi D, Busso M, Palmerini S, Trippella O, Cristallo S, Piersanti L, Chieffi A, Limongi M, Hoppe P and Kratz K L 2018 On the origin of early solar system radioactivities: problems with the asymptotic giant branch and massive star scenarios *Astrophys. J.* **863** 115
- [36] Urey H C 1955 The cosmic abundances of potassium, uranium, and thorium and the heat balances of the earth, the moon, and mars *Proc. Natl Acad. Sci.* **41** 127–44
- [37] Lichtenberg T, Golabek G J, Burn R, Meyer M R, Alibert Y, Gerya T V and Mordasini C 2019 A water budget dichotomy of rocky protoplanets from  $^{26}\text{Al}$ -heating *Nat. Astron.* **3** 307–13
- [38] Duprat J and Tatischeff V 2007 Energetic constraints on in situ production of short-lived radionuclides in the early solar system *Astrophys. J.* **671** L69–72
- [39] Cameron A G W and Truran J W 1977 The supernova trigger for formation of the solar system *Icarus* **30** 447–61
- [40] Boss A P, Ipatov S I, Keiser S A, Myhill E A and Vanhala H A T 2008 Simultaneous triggered collapse of the presolar dense cloud core and injection of short-lived radioisotopes by a supernova shock wave *Astrophys. J.* **686** L119
- [41] Boss A P, Keiser S A, Ipatov S I, Myhill E A and Vanhala H A T 2010 Triggering collapse of the presolar dense cloud core and injecting short-lived radioisotopes with a shock wave: I. Varied shock speeds *Astrophys. J.* **708** 1268–80
- [42] Gritschneider M, Lin D N C, Murray S D, Yin Q Z and Gong M N 2012 The supernova triggered formation and enrichment of our solar system *Astrophys. J.* **745** 22
- [43] Ouellette N, Desch S J and Hester J J 2010 Injection of supernova dust in nearby protoplanetary disks *Astrophys. J.* **711** 597–612
- [44] Pan L, Desch S J, Scannapieco E and Timmes F X 2012 Mixing of clumpy supernova ejecta into molecular clouds *Astrophys. J.* **756** 102
- [45] Goodson M D, Luebbers I, Heitsch F and Frazer C C 2016 Chemical enrichment of the pre-solar cloud by supernova dust grains *MNRAS* **462** 2777–91
- [46] Gaidos E, Krot A N, Williams J P and Raymond S N 2009  $^{26}\text{Al}$  and the formation of the solar system from a molecular cloud contaminated by Wolf-Rayet winds *Astrophys. J.* **696** 1854–63
- [47] Young E D 2014 Inheritance of solar short- and long-lived radionuclides from molecular clouds and the unexceptional nature of the solar system *Earth Planet. Sci. Lett.* **392** 16–27
- [48] Vasileiadis A, Nordlund Å and Bizzarro M 2013 Abundance of  $^{26}\text{Al}$  and  $^{60}\text{Fe}$  in evolving giant molecular clouds *Astrophys. J.* **769** L8
- [49] Adams F C, Fatuzzo M and Holden L 2014 Distributions of short-lived radioactive nuclei produced by young embedded star clusters *Astrophys. J.* **789** 86
- [50] Lacki B C 2014 Starbursts and high-redshift galaxies are radioactive: high abundances of  $^{26}\text{Al}$  and other short-lived radionuclides *MNRAS* **440** 3738–48
- [51] Fujimoto Y, Krumholz M R and Tachibana S 2018 Short-lived radioisotopes in meteorites from Galactic-scale correlated star formation *MNRAS* **480** 4025–39
- [52] Gounelle M and Meynet G 2012 Solar system genealogy revealed by extinct short-lived radionuclides in meteorites *A&A* **545** A4
- [53] Gounelle M 2015 The abundance of  $^{26}\text{Al}$ -rich planetary systems in the Galaxy *A&A* **582** A26
- [54] Brinkman H E, Doherty C L, Pols O R, Li E T, Côté B and Lugaro M 2019 Aluminium-26 from massive binary stars: I. nonrotating models *Astrophys. J.* **884** 38
- [55] Busso M, Gallino R and Wasserburg G J 1999 Nucleosynthesis in asymptotic giant branch stars: relevance for galactic enrichment and solar system formation *ARA&A* **37** 239–309
- [56] Kastner J H and Myers P C 1994 An observational estimate of the probability of encounters between mass-losing evolved stars and molecular clouds *Astrophys. J.* **421** 605
- [57] Lugaro M 2005 *Stardust From Meteorites (World Scientific Series in Astronomy and Astrophysics)*

- [58] Zinner E 2014 Presolar Grains *Meteorites and Cosmochemical Processes* **1** 181–213
- [59] Gropman E, Zinner E, Amari S, Gyngard F, Hoppe P, Jadhav M, Lin Y, Xu Y, Marhas K and Nittler L R 2015 Inferred initial  $^{26}\text{Al}/^{27}\text{Al}$  ratios in presolar stardust grains from supernovae are higher than previously estimated *Astrophys. J.* **809** 31
- [60] Gropman E, Zinner E, Amari S, Gyngard F, Hoppe P, Jadhav M, Lin Y, Xu Y, Marhas K and Nittler L R 2015 Inferred initial  $^{26}\text{Al}/^{27}\text{Al}$  ratios in presolar stardust grains from supernovae are higher than previously estimated *Astrophys. J.* **809** 31
- [61] Gyngard F, Zinner E, Nittler L R, Morgand A, Stadermann F J and Mairin Hynes K 2010 Automated NanoSIMS measurements of spinel stardust from the Murray meteorite *Astrophys. J.* **717** 107–20
- [62] Pignatari M, Zinner E, Hoppe P, Jordan C J, Gibson B K, Trappitsch R, Herwig F, Fryer C, Hirschi R and Timmes F X 2015 Carbon-rich presolar grains from massive stars: subsolar  $^{12}\text{C}/^{13}\text{C}$  and  $^{14}\text{N}/^{15}\text{N}$  ratios and the mystery of  $^{15}\text{N}$  *Astrophys. J.* **808** L43
- [63] van Raai M A, Lugaro M, Karakas A I and Iliadis C 2008 Reaction rate uncertainties and  $^{26}\text{Al}$  in AGB silicon carbide stardust *A&A* **478** 521–6
- [64] Palmerini S, La Cognata M, Cristallo S and Busso M 2011 Deep Mixing in Evolved Stars: I. The effect of reaction rate revisions from C to Al *Astrophys. J.* **729** 3
- [65] Palmerini S, Trippella O and Busso M 2017 A deep mixing solution to the aluminum and oxygen isotope puzzles in pre-solar grains *Monthly Notices of the Royal Astronomical Society* **467** 1193–201
- [66] José J, Hernanz M, Amari S, Lodders K and Zinner E 2004 The imprint of nova nucleosynthesis in presolar grains *Astrophysical Journal* **612** 414–28
- [67] Bose M and Starrfield S 2019 Condensation of SiC stardust in co nova outbursts *Astrophys. J.* **873** 14
- [68] Côté B, Yagüe A, Világos B and Lugaro M 2019 Stochastic chemical evolution of radioactive isotopes with a monte carlo approach *Astrophys. J.* **887** 213
- [69] Kaur T and Sahijpal S 2019 Heterogeneous evolution of the Galaxy and the origin of the short-lived nuclides in the early solar system *MNRAS* **490** 1620–37
- [70] Pleintinger M M M, Siegert T, Diehl R, Fujimoto Y, Greiner J, Krause M G H and Krumholz M R 2019 Comparing simulated  $^{26}\text{Al}$  maps to gamma-ray measurements *A&A* **632** A73
- [71] Fujimoto Y, Krumholz M R, Inutsuka S-I, Boss A P and Nittler L R 2020 Formation and evolution of the local interstellar environment: combined constraints from nucleosynthetic and X-ray data *MNRAS* **498** 5532–40
- [72] Krause M G H, Burkert A, Diehl R, Fierlinger K, Gaczkowski B, Kroell D, Ngoumou J, Roccatagliata V, Siegert T and Preibisch T 2018 Surround and Squash: the impact of superbubbles on the interstellar medium in Scorpius–Centaurus OB2 *A&A* **619** A120
- [73] Krause M G H, Rodgers-Lee D, Dale J E, Diehl R and Kobayashi C 2021 Galactic  $^{26}\text{Al}$  traces metal loss through hot chimneys *MNRAS* **501** 210–8
- [74] Clayton D D 1984 Al-26 in the interstellar medium *Astrophys. J.* **280** 144–9
- [75] Timmes F X, Woosley S E, Hartmann D H, Hoffman R D, Weaver T A and Matteucci F 1995  $^{26}\text{Al}$  and  $^{60}\text{Fe}$  from supernova explosions **449** 204
- [76] Huss G R, Meyer B S, Srinivasan G, Goswami J N and Sahijpal S 2009 Stellar sources of the short-lived radionuclides in the early solar system *Geochim. Cosmochim. Acta* **73** 4922–45
- [77] Côté B, Lugaro M, Reifarth R, Pignatari M, Világos B, Yagüe A and Gibson B K 2019 Galactic chemical evolution of radioactive isotopes *Astrophys. J.* **878** 156
- [78] López A Y, Côté B and Lugaro M 2021 Monte Carlo investigation of the ratios of short-lived radioactive isotopes in the interstellar medium *Astrophys. J.* **915** 128
- [79] Vasileiadis A, Nordlund Å and Bizzarro M 2013 Abundance of  $^{26}\text{Al}$  and  $^{60}\text{Fe}$  in evolving giant molecular clouds *Astrophys. J.* **769** L8
- [80] Palacios A, Meynet G, Vuissoz C, Knödseder J, Schaerer D, Cerviño M and Mowlavi N 2005 New estimates of the contribution of Wolf–Rayet stellar winds to the Galactic  $^{26}\text{Al}$  *A&A* **429** 613–24
- [81] Limongi M and Chieffi A 2006 The Nucleosynthesis of  $^{26}\text{Al}$  and  $^{60}\text{Fe}$  in solar metallicity stars extending in mass from 11 to 120  $M_{\text{solar}}$ : the hydrostatic and explosive contributions *Astrophys. J.* **647** 483–500
- [82] Woosley S E and Heger A 2007 Nucleosynthesis and remnants in massive stars of solar metallicity *Phys. Rep.* **442** 269–83

- [83] Pignatari M *et al* 2016 NuGrid stellar data set: I. Stellar yields from h to bi for stars with metallicities  $Z = 0.02$  and  $Z = 0.01$  *Astrophys. J. Suppl. Ser.* **225** 24
- [84] Herwig F 2005 Evolution of asymptotic giant branch stars *ARA&A* **43** 435–79
- [85] Karakas A I and Lattanzio J C 2014 The dawes review: II. Nucleosynthesis and stellar yields of low- and intermediate-mass single stars *PASA* **31** e030
- [86] Palmerini S and Busso M 2008  $^{26}\text{Al}$  production from magnetically induced extramixing in AGB stars *New Astron. Rev.* **52** 412–5
- [87] Wasserburg G J, Karakas A I and Lugaro M 2017 Intermediate-mass asymptotic giant branch stars and sources of  $^{26}\text{Al}$ ,  $^{60}\text{Fe}$ ,  $^{107}\text{Pd}$ , and  $^{182}\text{Hf}$  in the solar system *Astrophys. J.* **836** 126
- [88] Mowlavi N and Meynet G 2000 Aluminum 26 production in asymptotic giant branch stars *Astron. Astrophysics* **361** 959–76 (<https://adsabs.harvard.edu/pdf/2000A%26A...361..959M>)
- [89] Izzard R G, Lugaro M, Karakas A I, Iliadis C and van Raai M 2007 Reaction rate uncertainties and the operation of the NeNa and MgAl chains during HBB in intermediate-mass AGB stars *A&A* **466** 641–8
- [90] Siess L and Arnould M 2008 Production of  $^{26}\text{Al}$  by super-AGB stars *A&A* **489** 395–402
- [91] Mowlavi N 1999 On the third dredge-up phenomenon in asymptotic giant branch stars *A&A* **344** 617–31
- [92] Stancliffe R J and Jeffery C S 2007 Mass loss and yield uncertainty in low-mass asymptotic giant branch stars *MNRAS* **375** 1280–90
- [93] Ventura P and D’Antona F 2005 Full computation of massive AGB evolution: I. The large impact of convection on nucleosynthesis *A&A* **431** 279–88
- [94] Doherty C L, Gil-Pons P, Lau H H B, Lattanzio J C and Siess L 2014 Super and massive AGB stars—II. Nucleosynthesis and yields— $Z = 0.02, 0.008$  and  $0.004$  *MNRAS* **437** 195–214
- [95] Wasserburg G J, Boothroyd A I and Sackmann I J 1995 Deep circulation in red giant stars: a solution to the carbon and oxygen isotope puzzles? *Astrophys. J.* **447** L37
- [96] Nollett K M, Busso M and Wasserburg G J 2003 Cool bottom processes on the thermally pulsing asymptotic giant branch and the isotopic composition of circumstellar dust grains *Astrophys. J.* **582** 1036–58
- [97] Charbonnel C and Lagarde N 2010 Thermohaline instability and rotation-induced mixing: I. Low- and intermediate-mass solar metallicity stars up to the end of the AGB *Astron. Astrophys.* **522** A10
- [98] Eggleton P P, Dearborn D S P and Lattanzio J C 2006 Deep mixing of  $^3\text{He}$ : reconciling big bang and stellar nucleosynthesis *Science* **314** 1580
- [99] Fuller J, Lecoanet D, Cantiello M and Brown B 2014 Angular momentum transport via internal gravity waves in evolving stars *Astrophys. J.* **796** 17
- [100] Busso M, Wasserburg G J, Nollett K M and Calandra A 2007 Can extra mixing in rgb and agb stars be attributed to magnetic mechanisms? *Astrophys. J.* **671** 802–10
- [101] Stancliffe R J 2010 The effects of thermohaline mixing on low-metallicity asymptotic giant branch stars *Mon. Not. R Astron. Soc.* **403** 505–15
- [102] Denissenkov P A, Pinsonneault M and MacGregor K B 2009 Magneto-thermohaline mixing in red giants *Astrophys. J.* **696** 1823–33
- [103] Palmerini S, Cristallo S, Busso M, Abia C, Utenthaler S, Gialanella L and Maiorca E 2011 Deep mixing in evolved stars: II. Interpreting li abundances in red giant branch and asymptotic giant branch stars *Astrophys. J.* **741** 26
- [104] Nucci M C and Busso M 2014 Magnetohydrodynamics and deep mixing in evolved stars: I. Two- and three-dimensional analytical models for the asymptotic giant branch *Astrophys. J.* **787** 141
- [105] Nittler L R, Alexander O’D, Gao X, Walker R M and Zinner E 1997 Stellar sapphires: the properties and origins of presolar  $\text{Al}_2\text{O}_3$  in meteorites *Astrophys. J.* **483** 475–95
- [106] Straniero O *et al* 2013 Impact of a Revised  $^{25}\text{Mg}(p, \gamma)^{26}\text{Al}$  reaction rate on the operation of the Mg–Al Cycle *Astrophys. J.* **763** 100
- [107] Pain S D *et al* 2015 Constraint of the astrophysical  $^{26}\text{gAl}(p, \gamma)^{27}\text{Si}$  destruction rate at stellar temperatures *Phys. Rev. Lett.* **114** 212501
- [108] Iliadis C, Longland R, Champagne A E, Coc A and Fitzgerald R 2010 Charged-particle thermonuclear reaction rates: II. Tables and graphs of reaction rates and probability density functions *Nucl. Phys. A* **841** 31–250
- [109] Palmerini S, Cristallo S, Piersanti L, Vescovi D and Busso M 2021 Group II oxide grains: how massive are their agb star progenitors? *Universe* **7** 175

- [110] Diehl R 2013 Nuclear astrophysics lessons from INTEGRAL *Rep. Prog. Phys.* **76** 026301
- [111] Martin P, Knödlseeder J, Diehl R and Meynet G 2009 New estimates of the gamma-ray line emission of the Cygnus region from INTEGRAL/SPI observations *A&A* **506** 703–10
- [112] Diehl R, Lang M G, Martin P, Ohlendorf H, Preibisch T, Voss R, Jean P, Roques J-P, von Ballmoos P and Wang W 2010 Radioactive  $^{26}\text{Al}$  from the Scorpius–Centaurus association *A&A* **522** A51+
- [113] Voss R, Martin P, Diehl R, Vink J S, Hartmann D H and Preibisch T 2012 Energetic feedback and  $^{26}\text{Al}$  from massive stars and their supernovae in the Carina region *A&A* **539** A66
- [114] Walborn N R 1973 The space distribution of the O stars in the solar neighborhood *AJ* **78** 1067–83
- [115] Martins F, Schaerer D and Hillier D J 2005 A new calibration of stellar parameters of Galactic O stars *A&A* **436** 1049–65
- [116] Diehl R, Prantzos N and von Ballmoos P 2006 Astrophysical constraints from gamma-ray spectroscopy *Nucl. Phys. A* **777** 70–97
- [117] Cerviño M, Knödlseeder J, Schaerer D, von Ballmoos P and Meynet G 2000 Gamma-ray line emission from OB associations and young open clusters: I. Evolutionary synthesis models *A&A* **363** 970–83
- [118] Vink J S *et al* 2015 Very massive stars in the local universe *Highlights Astron.* **16** 51–79
- [119] Limongi M and Chieffi A 2006 The nucleosynthesis of  $^{26}\text{Al}$  and  $^{60}\text{Fe}$  in solar metallicity stars extending in mass from 11 to  $120 M_{\odot}$ : the hydrostatic and explosive contributions *Astrophys. J.* **647** 483–500
- [120] Nieuwenhuijzen H and de Jager C 1990 Parametrization of stellar rates of mass loss as functions of the fundamental stellar parameters M, L, and R *A&A* **231** 134–6
- [121] Vink J S, de Koter A and Lamers H J G L M 2000 New theoretical mass-loss rates of O and B stars *A&A* **362** 295–309
- [122] Vink J S, de Koter A and Lamers H J G L M 2001 Mass-loss predictions for O and B stars as a function of metallicity *A&A* **369** 574–88
- [123] Hamann F and Ferland G 1999 Elemental abundances in quasistellar objects: star formation and galactic nuclear evolution at high redshifts *ARA&A* **37** 487–531
- [124] Nugis T and Lamers H J G L M 2000 Mass-loss rates of Wolf–Rayet stars as a function of stellar parameters *A&A* **360** 227–44
- [125] Brinkman H E, Doherty C L, Pols O R, Li E T, Côté B and Lugaro M 2019 Aluminium-26 from massive binary stars: II. Nonrotating models *Astrophys. J.* **884** 38
- [126] Ekström S *et al* 2012 Grids of stellar models with rotation: I. Models from 0.8 to  $120 M_{\odot}$  at solar metallicity ( $Z = 0.014$ ) *A&A* **537** A146
- [127] Limongi M and Chieffi A 2018 Presupernova evolution and explosive nucleosynthesis of rotating massive stars in the metallicity range  $-3 \leq [\text{Fe}/\text{H}] \leq 0$  *Astrophys. J. Suppl. Ser.* **237** 13
- [128] Woosley S E, Kasen D, Blinnikov S and Sorokina E 2007 Type Ia supernova light curves *Astrophys. J.* **662** 487–503
- [129] Yusof N, Hirschi R, Meynet G, Crowther P A, Ekström S, Frischknecht U, Georgy C, Abu Kassim H and Schnurr O 2013 Evolution and fate of very massive stars *MNRAS* **433** 1114–32
- [130] Brinkman H E, Doherty C L, Pols O R, Li E T, Côté B and Lugaro M 2019 Aluminium-26 from massive binary stars: I. Nonrotating Models *Astrophys. J.* **884** 38
- [131] Duchêne G and Kraus A 2013 Stellar multiplicity *ARA&A* **51** 269–310
- [132] Sana H, de Mink S E, de Koter A, Langer N, Evans C J, Gieles M, Gosset E, Izzard R G, Le Bouquin J-B and Schneider F R N 2012 Binary interaction dominates the evolution of massive stars *Science* **337** 444
- [133] de Mink S E, Sana H, Langer N, Izzard R G and Schneider F R N 2014 The incidence of stellar mergers and mass gainers among massive stars *Astrophys. J.* **782** 7
- [134] Braun H and Langer N 1995 New massive close binary models and the  $^{26}\text{Al}$  yield of the WR component of gamma Vel *Wolf–Rayet Stars: Binaries; Colliding Winds; Evolution* ed K A van der Hucht and P M Williams vol 163 (Dordrecht: Springer) p 305
- [135] Crowther P A, Schnurr O, Hirschi R, Yusof N, Parker R J, Goodwin S P and Kassim H A 2010 The R136 star cluster hosts several stars whose individual masses greatly exceed the accepted  $150 M_{\text{solar}}$  stellar mass limit *MNRAS* **408** 731–51
- [136] Bestenlehner J M *et al* 2014 The VLT-FLAMES Tarantula Survey: XVII. Physical and wind properties of massive stars at the top of the main sequence *A&A* **570** A38

- [137] Martins F 2015 Mass loss of massive stars *SF2A-2015: Proc. of the Annual meeting of the French Society of Astronomy and Astrophysics* pp 343–8
- [138] Crowther P A *et al* 2016 The R136 star cluster dissected with Hubble Space Telescope/STIS. I. Far-ultraviolet spectroscopic census and the origin of He II  $\lambda$  1640 in young star clusters *MNRAS* **458** 624–59
- [139] Bestenlehner J M *et al* 2020 The R136 star cluster dissected with Hubble Space Telescope/STIS: II. Physical properties of the most massive stars in R136 *MNRAS* **499** 1918–36
- [140] Vink J S, Muijres L E, Anthonisse B, de Koter A, Gräfener G and Langer N 2011 Wind modelling of very massive stars up to 300 solar masses *A&A* **531** A132
- [141] Vink J S and Gräfener G 2012 The transition mass-loss rate: calibrating the role of line-driven winds in massive star evolution *Astrophys. J.* **751** L34
- [142] Voss R, Diehl R, Hartmann D H, Cerviño M, Vink J S, Meynet G, Limongi M and Chieffi A 2009 Using population synthesis of massive stars to study the interstellar medium near OB associations *A&A* **504** 531–42
- [143] Köhler K *et al* 2015 The evolution of rotating very massive stars with LMC composition *A&A* **573** A71
- [144] Gasques L R, Brown E F, Chieffi A, Jiang C L, Limongi M, Rolfs C, Wiescher M and Yakovlev D G 2007 Implications of low-energy fusion hindrance on stellar burning and nucleosynthesis *Phys. Rev. C* **76** 035802
- [145] Ritter C, Herwig F, Jones S, Pignatari M, Fryer C and Hirschi R 2018 NuGrid stellar data set—II. Stellar yields from H to Bi for stellar models with  $M_{\text{ZAMS}} = 1\text{--}25 M_{\odot}$  and  $Z = 0.0001\text{--}0.02$  *MNRAS* **480** 538–71
- [146] Blake J B and Schramm D N 1976 A possible alternative to the r-process *Astrophys. J.* **209** 846–9
- [147] Meyer B S, Clayton D D and The L S 2000 Molybdenum and zirconium isotopes from a supernova neutron burst *Astrophys. J.* **540** L49–52
- [148] Pignatari M, Hoppe P, Trappitsch R, Fryer C, Timmes F X, Herwig F and Hirschi R 2018 The neutron capture process in the He shell in core-collapse supernovae: presolar silicon carbide grains as a diagnostic tool for nuclear astrophysics *Geochim. Cosmochim. Acta* **221** 37–46
- [149] Herwig F, Woodward P R, Lin P-H, Knox M and Fryer C 2014 Global Non-spherical oscillations in three-dimensional  $4\pi$  simulations of the H-ingestion flash *Astrophys. J.* **792** L3
- [150] Clarkson O and Herwig F 2020 Convective H–He interactions in massive population III stellar evolution models *Monthly Notices of the RAS* **500** 2685–2703 arXiv:2005.07748
- [151] Woosley S E, Hartmann D H, Hoffman R D and Haxton W C 1990 The  $\nu$ -process *Astrophysical Journal* **356** 272–301 (<https://adsabs.harvard.edu/pdf/1990ApJ...356..272W>)
- [152] Domogatskij G V and Nadezhin D K 1980 Neutrino-induced production of radioactive aluminum-26 *Soviet Astron. Lett.* **6** 127
- [153] Sieverding A, Martínez-Pinedo G, Huther L, Langanke K and Heger A 2018 The  $\nu$ -process in the light of an improved understanding of supernova neutrino spectra *Astrophysical Journal* **865** 143
- [154] Zegers R G T *et al* 2006 The (t,He3) and (He3, t) reactions as probes of Gamow–Teller strength *Phys. Rev. C* **74** 024309
- [155] Coc A, Mochkovitch R, Oberto Y, Thibaud J P and Vangioni-Flam E 1995 ONeMg novae: nuclear uncertainties on the  $^{26}\text{Al}$  and  $^{22}\text{Ne}$  yields *A&A* **299** 479
- [156] José J, Coc A and Hernanz M 1999 Nuclear uncertainties in the NeNa–MgAl cycles and production of  $^{22}\text{Na}$  and  $^{26}\text{Al}$  during nova outbursts *Astrophys. J.* **520** 347–60
- [157] Mahoney W A, Ling J C, Jacobson A S and Lingenfelter R E 1982 Diffuse galactic gamma-ray line emission from nucleosynthetic Fe-60, Al-26, and Na-22—Preliminary limits from HEAO 3 *Astrophys. J.* **262** 742–8
- [158] Mahoney W A, Ling J C, Wheaton W A and Jacobson A S 1984 HEAO 3 discovery of Al-26 in the interstellar medium *Astrophys. J.* **286** 578–85
- [159] Ward R A and Fowler W A 1980 Thermalization of long-lived nuclear isomeric states under stellar conditions *Astrophys. J.* **238** 266–86
- [160] Hillebrandt W and Thielemann F K 1982 Nucleosynthesis in novae—a source of Ne-E and Al-26 *Astrophys. J.* **255** 617–23
- [161] Wiescher M, Gorres J, Thielemann F K and Ritter H 1986 Explosive hydrogen burning in novae *A&A* **160** 56–72
- [162] Starrfield S, Sparks W M and Truran J W 1986 Hydrodynamic models for novae with ejecta rich in oxygen, neon, and magnesium *Astrophys. J.* **303** L5

- [163] Weiss A and Truran J W 1990 Na-22 and Al-26 production and nucleosynthesis in novae explosions *A&A* **238** 178–86
- [164] Nofar I, Shaviv G and Starrfield S 1991 The formation of  $^{26}\text{Al}$  nova explosions *Astrophys. J.* **369** 440
- [165] Starrfield S, Truran J W, Politano M, Sparks W M, Nofar I and Shaviv G 1993  $^{22}\text{Na}$  and  $^{26}\text{Al}$  production in nova outbursts *Phys. Rep.* **227** 223–34
- [166] Politano M, Starrfield S, Truran J W, Weiss A and Sparks W M 1995 Hydrodynamic studies of accretion onto massive white dwarfs: onemg-enriched nova outbursts: I. Dependence on white dwarf mass *Astrophys. J.* **448** 807
- [167] Arnett W D and Truran J W 1969 Carbon-burning nucleosynthesis at constant temperature *Astrophys. J.* **157** 339
- [168] Dominguez I, Tornambe A and Isern J 1993 On the formation of O-Ne white dwarfs in metal-rich close binary systems *Astrophys. J.* **419** 268
- [169] Ritossa C, Garcia-Berro E and Icko I Jr. 1996 On the evolution of stars that form electron-degenerate cores processed by carbon burning: II. Isotope abundances and thermal pulses in a  $10 M_{\text{sun}}$  model with an one core and applications to long-period variables, classical novae, and accretion-induced collapse *Astrophys. J.* **460** 489
- [170] José J, Hernanz M and Coc A 1997 New results on  $^{26}\text{Al}$  production in classical novae *Astrophys. J.* **479** L55–8
- [171] José J and Hernanz M 1998 Nucleosynthesis in classical novae: CO versus ONe white dwarfs *Astrophys. J.* **494** 680–90
- [172] José J, Shore S N and Casanova J 2020 123-321 models of classical novae *A&A* **634** A5
- [173] Casanova J, José J, García-Berro E, Shore S N and Calder A C 2011 Kelvin–Helmholtz instabilities as the source of inhomogeneous mixing in nova explosions *Nature* **478** 490–2
- [174] Casanova J, José J, García-Berro E and Shore S N 2016 Three-dimensional simulations of turbulent convective mixing in ONe and CO classical nova explosions *A&A* **595** A28
- [175] Casanova J, José J and Shore S N 2018 Two-dimensional simulations of mixing in classical novae: the effect of white dwarf composition and mass *A&A* **619** A121
- [176] Shafter A W 2017 The galactic nova rate revisited *Astrophys. J.* **834** 196
- [177] Diehl R *et al* 2006 Radioactive  $^{26}\text{Al}$  from massive stars in the Galaxy *Nature* **439** 45–7
- [178] Diehl R *et al* 1995 COMPTEL observations of Galactic  $^{26}\text{Al}$  emission *A&A* **298** 445
- [179] Iliadis C, Longland R, Champagne A E and Coc A 2010 Charged-particle thermonuclear reaction rates: III. Nuclear physics input *Nucl. Phys. A* **841** 251–322
- [180] Iliadis C 2019 Calculation of resonance energies from Q values *Phys. Rev. C* **99** 065809
- [181] Wang M, Huang W J, Kondev F G, Audi G and Naimi S 2021 The AME 2020 atomic mass evaluation (II). Tables, graphs and references *Chin. Phys. C* **45** 030003
- [182] Endt P M and Rolfs C 1987 Astrophysical aspects of the  $^{25}\text{Mg}(p, \gamma)^{26}\text{Al}$  reaction *Nucl. Phys. A* **467** 272
- [183] RadCapFraction. (<https://github.com/padsley/RadCapFraction>)
- [184] Iliadis C, Buchmann L, Endt P M, Herndl H and Wiescher M 1996 New stellar reaction rates for  $^{25}\text{Mg}(p, \gamma)^{26}\text{Al}$  and  $^{25}\text{Al}(p, \gamma)^{26}\text{Si}$  *Phys. Rev. C* **53** 475–96
- [185] Li Y J *et al* 2020 Indirect measurement of the 57.7 keV resonance strength for the astrophysical  $\gamma$ -ray source of the  $^{25}\text{Mg}(p, \gamma)^{26}\text{Al}$  reaction *Phys. Rev. C* **102** 025804
- [186] Kankainen A *et al* 2021 Decay of the key 92 keV resonance in the  $^{25}\text{Mg}(p, \gamma)$  reaction to the ground and isomeric states of the cosmic  $\gamma$ -ray emitter  $^{26}\text{Al}$  *Phys. Lett. B* **813** 136033
- [187] Strieder F *et al* 2012  $^{25}\text{Mg}(p, \gamma)^{26}\text{Al}$  reaction at low astrophysical energies *Phys. Lett. B* **707** 60–5
- [188] Su J *et al* 2022 First result from the Jinping underground nuclear astrophysics experiment juna: precise measurement of the 92-keV  $^{25}\text{Mg}(p, \gamma)^{26}\text{Al}$  resonance *Sci. Bull.* **67** 125–32
- [189] Lotay G *et al* 2022 Revised decay properties of the key 93-keV resonance in the  $^{25}\text{Mg}(p, \gamma)$  reaction and its influence on the mgal cycle in astrophysical environments *Phys. Rev. C* **105** L042801
- [190] Iliadis C, D’Auria J M, Starrfield S, Thompson W J and Wiescher M 2001 Proton-induced thermonuclear reaction rates for  $A = 20$ –40 nuclei *Astrophys. J. Suppl. Ser.* **134** 151–71
- [191] Arazi A, Faestermann T, Niello J O F, Knie K, Korschinek G, Poutivtsev M, Richter E, Rugel G and Wallner A 2006 Measurement of  $^{25}\text{Mg}(p, \gamma)^{26}\text{Al}^g$  resonance strengths via accelerator mass spectrometry *Phys. Rev. C* **74** 025802



- [192] Endt P M and Rolfs C 1987 Astrophysical aspects of the  $^{25}\text{Mg}(p, \gamma)^{26}\text{Al}$  reaction *Nucl. Phys. A* **467** 261–72
- [193] Iliadis C 1997 Proton single-particle reduced widths for unbound states *Nucl. Phys. A* **618** 166–75
- [194] Endt P M, de Wit P, Alderliesten C and Wildenthal B H 1988 Spins, parities and isospins of  $^{26}\text{Al}$  levels: Shell-model aspects *Nucl. Phys. A* **487** 221–50
- [195] Limata B *et al* 2010 New experimental study of low-energy  $(p, \gamma)$  resonances in magnesium isotopes *Phys. Rev. C* **82** 015801
- [196] Betts R R, Fortune H T and Pullen D J 1978 A study of  $^{26}\text{Al}$  by the  $^{25}\text{Mg}(^3\text{He}, d)$  reaction *Nucl. Phys. A* **299** 412–28
- [197] Champagne A E, Howard A J and Parker P D 1983 Threshold states in  $^{26}\text{Al}$ : (I). Experimental investigations *Nucl. Phys. A* **402** 159–78
- [198] Champagne A E, Howard A J and Parker P D 1983 Threshold states in  $^{26}\text{Al}$  *Nucl. Phys. A* **402** 179–88
- [199] Champagne A E, McDonald A B, Wang T F, Howard A J, Magnus P V and Parker P D 1986 Threshold states in  $^{26}\text{Al}$  revisited *Nucl. Phys. A* **451** 498–508
- [200] Champagne A E, Howard A J, Smith M S, Magnus P V and Parker P D 1989 The effect of weak resonances on the  $^{25}\text{Mg}(p, \gamma)^{26}\text{Al}$  reaction rate *Nucl. Phys. A* **505** 384–96
- [201] Wijekumar V, Schmalbrock P, Hausman H J, Donoghue T R, Wiescher M, Suiter H R, Browne C P, Rollefson A A and Tarara R W 1985 Proton threshold states in  $^{26}\text{Al}$  *Nucl. Phys. A* **436** 561–72
- [202] Bergmeister F J, Lieb K P, Pampus K and Uhrmacher M 1985 Note on Stellar  $^{26}\text{Al}$  Production via the  $^{25}\text{Mg}(p, \gamma)$  Process *Z. Phys. A* **320** 693
- [203] Endt P M, de Wit P and Alderliesten C 1986 The  $^{25}\text{Mg}(p, \gamma)^{26}\text{Al}$  and  $^{25}\text{Mg}(p, p')$  resonances for  $E_p = 0.31\text{--}1.84$  MeV *Nucl. Phys. A* **459** 61–76
- [204] Iliadis C *et al* 1990 Low-energy resonances in  $^{25}\text{Mg}(p, \gamma)^{26}\text{Al}$ ,  $^{26}\text{Mg}(p, \gamma)^{27}\text{Al}$  and  $^{27}\text{Al}(p, \gamma)^{28}\text{Si}$  *Nucl. Phys. A* **512** 509–30
- [205] Powell D C, Iliadis C, Champagne A E, Hale S E, Hansper V Y, Surman R A and Veal K D 1998 Low-energy resonance strengths for proton capture on Mg and Al nuclei *Nucl. Phys. A* **644** 276
- [206] Rollefson A A, Wijekumar V, Browne C P, Wiescher M, Hausman H J, Kim W Y and Schmalbrock P 1990 Spectroscopic factors for proton unbound levels in  $^{26}\text{Al}$  and their influence on stellar reaction rates *Nucl. Phys. A* **507** 425
- [207] Liu W P *et al* 2016 Progress of jinping underground laboratory for nuclear astrophysics (JUNA) *Sci. China Phys., Mech., Astron.* **59** 5785
- [208] Angulo C *et al* 1999 A compilation of charged-particle induced thermonuclear reaction rates *Nucl. Phys. A* **656** 3–183
- [209] Endt P M 1990 Energy levels of  $A = 21\text{--}44$  nuclei (VII) *Nucl. Phys. A* **521** 1–400
- [210] Longland R, Iliadis C, Champagne A E, Newton J R, Ugalde C, Coc A and Fitzgerald R 2010 Charged-particle thermonuclear reaction rates: I. Monte Carlo method and statistical distributions *Nucl. Phys. A* **841** 1–30
- [211] Sallaska A L, Iliadis C, Champagne A E, Goriely S, Starrfield S and Timmes F X 2013 Starlib: a next-generation reaction-rate library for nuclear astrophysics *Astrophys. J. Suppl. Ser.* **207** 18
- [212] Pogrebnyak I, Howard C, Iliadis C, Longland R and Mitchell G E 2013 Mean proton and  $\alpha$ -particle reduced widths of the Porter–Thomas distribution and astrophysical applications *Phys. Rev. C* **88** 015808
- [213] Iliadis C, Longland R, Champagne A E, Coc A and Fitzgerald R 2010 Charged-particle thermonuclear reaction rates: II. tables and graphs of reaction rates and probability density functions *Nucl. Phys. A* **841** 31–250
- [214] Margerin V *et al* 2015 Inverse kinematic study of the  $^{26}\text{Al}(d, p)^{27}\text{Al}$  reaction and implications for destruction of  $^{26}\text{Al}$  in Wolf–Rayet and asymptotic giant branch stars *Phys. Rev. Lett.* **115** 062701
- [215] Almaraz-Calderon S *et al* 2017 Study of the  $^{26}\text{Al}^m(d, p)^{27}\text{Al}$  Reaction and the Influence of the  $^{26}\text{Al}$   $0^+$  Isomer on the Destruction of  $^{26}\text{Al}$  in the Galaxy *Phys. Rev. Lett.* **119** 072701
- [216] Runkle R C, Champagne A E and Engel J 2001 Thermal equilibration of  $^{26}\text{Al}$  *Astrophys. J.* **556** 970–8
- [217] Vogelaar R B 1989 The  $^{26}\text{Al}(p, \gamma)^{27}\text{Si}$  reaction: stellar origins of galactic  $^{26}\text{Al}$  *PhD Thesis* California Institute of Technology

- [218] Buchmann L, Hilgemeier M, Krauss A, Redder A, Rolfs C, Trautvetter H P and Donoghue T R 1984 The abundance of  $^{26}\text{Al}$  in the MgAl cycle *Nucl. Phys. A* **415** 93–113
- [219] Ruiz C *et al* 2006 Measurement of the  $E_{\text{c.m.}} = 184$  keV resonance strength in the  $^{26}\text{gAl}(p, \gamma)^{27}\text{Si}$  reaction *Phys. Rev. Lett.* **96** 252501
- [220] Vogelaar R B, Mitchell L W, Kavanagh R W, Champagne A E, Magnus P V, Smith M S, Howard A J, Parker P D and O'Brien H A 1996 Constraining  $^{26}\text{Al}+p$  resonances using  $^{26}\text{Al}(\text{he,d})^{27}\text{Si}$  *Phys. Rev. C* **53** 1945–9
- [221] Lotay G, Woods P J, Seweryniak D, Carpenter M P, Janssens R V F and Zhu S 2009 Identification of key astrophysical resonances relevant for the  $^{26}\text{gAl}(p, \gamma)^{27}\text{Si}$  reaction in Wolf-Rayet stars, agb stars, and classical novae *Phys. Rev. Lett.* **102** 162502
- [222] Lotay G, Woods P J, Seweryniak D, Carpenter M P, Janssens R V F and Zhu S 2009  $\gamma$ -ray spectroscopy study of states in  $^{27}\text{Si}$  relevant for the  $^{26}\text{Al}^m(p, \gamma)^{27}\text{Si}$  reaction in novae and supernovae *Phys. Rev. C* **80** 055802
- [223] Longland R, Iliadis C and Karakas A I 2012 Reaction rates for the s-process neutron source  $^{22}\text{Ne} + \alpha$  *Phys. Rev. C* **85** 065809
- [224] Parikh A, José J, Karakas A, Ruiz C and Wimmer K 2014 Strength of the  $E_R = 127$  keV,  $^{26}\text{Al}(p, \gamma)^{27}\text{Si}$  resonance *Phys. Rev. C* **90** 038801
- [225] Schmalbrock P, Donoghue T R, Wiescher M, Wijekumar V, Browne C P, Rollefson A A, Rolfs C and Vlieks A 1986 Proton threshold states in  $^{27}\text{Si}$  and their implications on hydrogen burning of  $^{26}\text{Al}$  *Nucl. Phys. A* **457** 182–8
- [226] Wang T F, Champagne A E, Hadden J D, Magnus P V, Smith M S, Howard A J and Parker P D 1989 Proton threshold states in  $^{27}\text{Si}$  and the destruction of  $^{26}\text{Al}$  at low stellar temperatures *Nucl. Phys. A* **499** 546–64
- [227] Kankainen A *et al* 2016 Angle-integrated measurements of the  $^{26}\text{Al}(d,n)^{27}\text{Si}$  reaction cross section: a probe of spectroscopic factors and astrophysical resonance strengths *Eur. Phys. J. A* **52** 6
- [228] Lotay G *et al* 2020 High-resolution radioactive beam study of the  $^{26}\text{Al}(d, p)$  reaction and measurements of single-particle spectroscopic factors *Eur. Phys. J. A* **56** 1–6
- [229] Angulo C *et al* 1999 A compilation of charged-particle induced thermonuclear reaction rates *Nucl. Phys. A* **656** 3–183
- [230] Lotay G *et al* 2022 Radiative capture on nuclear isomers: direct measurement of the  $^{26m}\text{Al}(p, \gamma)^{27}\text{Si}$  reaction *Phys. Rev. Lett.* **128** 042701
- [231] Deibel C M, Clark J A, Lewis R, Parikh A, Parker P D and Wrede C 2009 Toward an experimentally determined  $^{26}\text{Al}^m(p, \gamma)^{27}\text{Si}$  reaction rate in ONe novae *Phys. Rev. C* **80** 035806
- [232] Good E C *et al* in preparation
- [233] Lotay G, Woods P J, Seweryniak D, Carpenter M P, Janssens R V F and Zhu S 2010  $\gamma$ -ray spectroscopy study of states in  $^{27}\text{Si}$  relevant for the  $^{26}\text{Al}^m(p, \gamma)^{27}\text{Si}$  reaction in novae and supernovae *Phys. Rev. C* **81** 029903
- Lotay G, Woods P J, Seweryniak D, Carpenter M P, Janssens R V F and Zhu S 2009  $\gamma$ -ray spectroscopy study of states in  $^{27}\text{Si}$  relevant for the  $^{26}\text{Al}^m(p, \gamma)^{27}\text{Si}$  reaction in novae and supernovae *Phys. Rev. C* **80** 055802
- [234] Lotay G, Woods P J, Seweryniak D, Carpenter M P, David H M, Janssens R V F and Zhu S 2011 Identification of analog states in the  $T = 1/2$   $A = 27$  mirror system from low excitation energies to the region of hydrogen burning in the  $^{26}\text{Al}^{g,m}(p, \gamma)^{27}\text{Si}$  reactions *Phys. Rev. C* **84** 035802
- [235] Wang M, Audi G, Kondev F G, Huang W J, Naimi S and Xu X 2017 The AME2016 atomic mass evaluation (II). Tables, graphs and references *Chin. Phys. C* **41** 030003
- [236] Lee I-Y 1990 The GAMMASPHERE *Nucl. Phys. A* **520** c641–55
- [237] Janssens R V F and Stephens F S 1996 *Nucl. Phys. News* **6** 9
- [238] Buchmann L, Hilgemeier M, Krauss A, Redder A, Rolfs C, Trautvetter H P and Donoghue T R 1984 The abundance of  $^{26}\text{Al}$  in the MgAl cycle *Nucl. Phys. A* **415** 93–113
- [239] Almaraz-Calderon S, Bertone P F, Alcorta M, Albers M, Deibel C M, Hoffman C R, Jiang C L, Marley S T, Rehm K E and Ugalde C 2015 Direct measurement of the  $^{23}\text{Na}(\alpha, p)^{26}\text{Mg}$  reaction cross section at energies relevant for the production of galactic  $^{26}\text{Al}$  *Phys. Rev. Lett.* **115** 179901
- Almaraz-Calderon S *et al* 2017 Study of the  $^{26}\text{Al}^m(d, p)^{27}\text{Al}$  Reaction and the Influence of the  $^{26}\text{Al}$   $0^+$  Isomer on the Destruction of  $^{26}\text{Al}$  in the Galaxy *Phys. Rev. Lett.* **119** 072701
- Almaraz-Calderon S, Bertone P F, Alcorta M, Albers M, Deibel C M, Hoffman C R, Jiang C L, Marley S T, Rehm K E and Ugalde C 2014 Direct measurement of the  $^{23}\text{Na}(\alpha, p)^{26}\text{Mg}$

- reaction cross section at energies relevant for the production of galactic  $^{26}\text{Al}$  *Phys. Rev. Lett.* **112** 152701
- [240] Hallam S *et al* 2021 Exploiting isospin symmetry to study the role of isomers in stellar environments *Phys. Rev. Lett.* **126** 042701
- [241] Iliadis C, Champagne A, Chieffi A and Limongi M 2011 The effects of thermonuclear reaction rate variations on  $^{26}\text{Al}$  production in massive stars: a sensitivity study *Astrophys. J. Suppl. Ser.* **193** 16
- [242] Shamsuzzoha Basunia M 2011 Nuclear Data Sheets for  $A = 27$  *Nucl. Data Sheets* **112** 1875–948
- [243] Trautvetter H P and Käppeler F 1984 Destruction of  $^{26}\text{Al}$  via the  $^{26}\text{Al}(n,p)^{26}\text{Mg}$ -reaction *Z. Phys. A* **318** 121–2
- [244] Trautvetter H P *et al* 1986 Destruction of  $^{26}\text{Al}$  in explosive nucleosynthesis. *Z. Phys. A* **323** 1–11
- [245] Koehler P E, Kavanagh R W, Vogelaar R B, Gledenov Yu M and Popov Y P 1997  $^{26}\text{Al}(n, p_1)$  and  $(n, \alpha_0)$  cross sections from thermal energy to 70 keV and the nucleosynthesis of  $^{26}\text{Al}$  *Phys. Rev. C* **56** 1138–43
- [246] De Smet L, Wagemans C, Wagemans J, Heyse J and Van Gils J 2007 Experimental determination of the  $^{26}\text{Al}(n, \alpha)^{23}\text{Na}$  reaction cross section and calculation of the Maxwellian averaged cross section at stellar temperatures *Phys. Rev. C* **76** 045804
- [247] Skelton R T, Kavanagh R W and Sargood D G 1987  $^{26}\text{Mg}(p,n)^{26}\text{Al}$  and  $^{23}(\alpha, n)^{26}\text{Al}$  reactions *Phys. Rev. C* **35** 45–54
- [248] Lederer-Woods C *et al* 2021 Destruction of the cosmic  $\gamma$ -ray emitter  $^{26}\text{Al}$  in massive stars: study of the key  $^{26}\text{Al}(n, p)$  reaction *Phys. Rev. C* **104** L022803
- [249] Lederer-Woods C *et al* 2021 Destruction of the cosmic  $\gamma$ -ray emitter  $^{26}\text{Al}$  in massive stars: study of the key  $^{26}\text{Al}(n, \alpha)$  reaction *Phys. Rev. C* **104** L032803
- [250] Benamara S *et al* 2014 Nucleosynthesis of  $^{26}\text{Al}$  in massive stars: new  $^{27}\text{Al}$  states above  $\alpha$  and neutron emission thresholds *Phys. Rev. C* **89** 065805
- [251] Adsley P *et al* in preparation
- [252] Moss C E and Sherman J D 1976 Excitation energies of levels in  $^{27}\text{Al}$  and  $^{28}\text{Si}$  *Nucl. Phys. A* **259** 413–22
- [253] Moss C E 1976 Excitation energies of levels in  $^{23}\text{Na}$ ,  $^{24}\text{Mg}$  and  $^{26}\text{Mg}$  *Nucl. Phys. A* **269** 429–42
- [254] Adsley P, Laird A M and Meisel Z 2020 Status of the  $^{24}\text{Mg}(\alpha, \gamma)^{28}\text{Si}$  reaction rate at stellar temperatures *Phys. Rev. C* **102** 015801
- [255] Chipps K A 2016 Resonances above the proton threshold in  $^{26}\text{Si}$  *Phys. Rev. C* **93** 035801
- [256] Richter W A, Alex Brown B, Signoracci A and Wiescher M 2011 Properties of  $^{26}\text{Mg}$  and  $^{26}\text{Si}$  in the  $sd$  shell model and the determination of the  $^{25}\text{Al}(p, \gamma)^{26}\text{Si}$  reaction rate *Phys. Rev. C* **83** 065803
- [257] Liang P F *et al* 2020 Simultaneous measurement of beta -delayed proton and  $\gamma$  emission of  $^{26}\text{P}$  for the  $^{25}\text{Al}(p, \gamma)^{26}\text{Si}$  reaction rate *Phys. Rev. C* **101** 024305
- [258] Bardayan D W *et al* 2002 Astrophysically important  $^{26}\text{Si}$  states studied with the  $^{28}\text{Si}(p, t)^{26}\text{Si}$  reaction *Phys. Rev. C* **65** 032801
- [259] Caggiano J A, Bradfield-Smith W, Lewis R, Parker P D, Visser D W, Greene J P, Rehm K E, Bardayan D W and Champagne A E 2002 Identification of new states in  $^{26}\text{Si}$  using the  $^{29}\text{Si}(^3\text{He}, ^6\text{He})^{26}\text{Si}$  reaction and consequences for the  $^{25}\text{Al}(p, \gamma)^{26}\text{Si}$  reaction rate in explosive hydrogen burning environments *Phys. Rev. C* **65** 055801
- [260] Bell R A I, L'Ecuyer J, Gill R D, Robertson B C, Towner I S and Rose H J 1969 Excitation energies and lifetimes of levels in  $^{26}\text{Si}$  *Nucl. Phys. A* **133** 337–56
- [261] Parpottas Y, Grimes S M, Al-Quraishi S, Brune C R, Massey T N, Oldendick J E, Salas A and Wheeler R T 2004 Astrophysically important  $^{26}\text{Si}$  states studied with the  $(^3\text{He}, n)$  reaction and the  $^{25}\text{Al}(p, \gamma)^{26}\text{Si}$  reaction rates in explosive hydrogen burning environments *Phys. Rev. C* **70** 065805
- [262] Bardayan D W *et al* 2006 Astrophysically important  $^{26}\text{Si}$  states studied with the  $^{28}\text{Si}(p, t)^{26}\text{Si}$  reaction. II. Spin of the 5.914-MeV  $^{26}\text{Si}$  level and galactic  $^{26}\text{Al}$  production *Phys. Rev. C* **74** 045804
- [263] Canete L *et al* 2021 New constraints on the  $^{25}\text{Al}(p, \gamma)$  reaction and its influence on the flux of cosmic  $\gamma$  rays from classical nova explosions *Phys. Rev. C* **104** L022802
- [264] Peplowski P N *et al* 2009 Lowest  $l=0$  proton resonance in  $^{26}\text{Si}$  and implications for nucleosynthesis of  $^{26}\text{Al}$  *Phys. Rev. C* **79** 032801
- [265] Bennett M B *et al* 2013 Classical-nova contribution to the milky way's  $^{26}\text{Al}$  abundance: exit channel of the key  $^{25}\text{Al}(p, \gamma)^{26}\text{Si}$  resonance *Phys. Rev. Lett.* **111** 232503

- [266] Perello J F *et al* 2022 Low-lying resonances in  $^{26}\text{Si}$  relevant for the determination of the astrophysical  $^{25}\text{Al}(p, \gamma)^{26}\text{Si}$  reaction rate *Phys. Rev. C* **105** 035805
- [267] Seweryniak D *et al* 2007 Level structure of  $^{26}\text{Si}$  and its implications for the astrophysical reaction rate of  $^{25}\text{Al}(p, \gamma)^{26}\text{Si}$  *Phys. Rev. C* **75** 062801
- [268] Komatsubara T *et al* 2014 Excited states above the proton threshold in  $^{26}\text{Si}$  *Eur. Phys. J. A* **50** 136
- [269] Doherty D T *et al* 2015 Structure of resonances in the Gamow burning window for the  $^{25}\text{Al}(p, \gamma)^{26}\text{Si}$  reaction in novae *Phys. Rev. C* **92** 035808
- [270] Hamill C B, Woods P J, Kahl D, Longland R, Greene J P, Marshall C, Portillo F and Setoodehnia K 2020 Study of the  $^{25}\text{Mg}(d,p)^{26}\text{Mg}$  reaction to constrain the  $^{25}\text{Al}(p, \gamma)^{26}\text{Si}$  resonant reaction rates in nova burning conditions *Eur. Phys. J. A* **56** 36
- [271] de Séréville N *et al* 2011 Spectroscopic study of  $^{26}\text{Si}$  for application to nova gamma-ray emission *Proceedings of Science NIC XI* 212
- [272] Timofeyuk N K, Descouvemont P and Johnson R C 2006 Relation between proton and neutron asymptotic normalization coefficients for light mirror nuclei and its relevance for nuclear astrophysics *Eur. Phys. J. A* **27** 269–76
- [273] Wrede C 2009 Thermonuclear  $^{25}\text{Al}(p, \gamma)^{26}\text{Si}$  reaction rate in classical novae and Galactic  $^{26}\text{Al}$  *Phys. Rev. C* **79** 035803
- [274] Cyburt R H *et al* 2010 the jina reaclib database: its recent updates and impact on type-i x-ray bursts *Astrophys. J. Suppl. Ser.* **189** 240–52
- [275] Van der Zwan L and Geiger K W 1981 Cross Sections for the  $^{25}\text{Mg}(\alpha, n)^{28}\text{Si}$  Reaction for  $E_\alpha < 4.8$  MeV *Nucl. Sci. Eng.* **79** 197–201
- [276] Anderson M R, Mitchell L W, Sevier M E and Sargood D G 1983  $^{25}\text{Mg}(\alpha, n)^{28}\text{Si}$  and  $^{26}\text{Mg}(\alpha, n)^{29}\text{Si}$  as neutron sources in explosive neon burning *Nucl. Phys. A* **405** 170–8
- [277] Wieland O 1995 *Diploma Thesis*
- [278] Iliadis C, Champagne A, Chieffi A and Limongi M 2011 The effects of thermonuclear reaction rate variations on  $^{26}\text{Al}$  production in massive stars: a sensitivity study *Astrophysical Journal Supplement* **193** 16
- [279] Tomlinson J R *et al* 2015 Measurement of  $^{23}\text{Na}(\alpha, p)^{26}\text{Mg}$  at energies relevant to  $^{26}\text{Al}$  production in massive stars *Phys. Rev. Lett.* **115** 052702
- [280] Avila M L *et al* 2016 Experimental study of the astrophysically important  $^{23}\text{Na}(\alpha, p)^{26}\text{Mg}$  and  $^{23}\text{Na}(\alpha, n)^{26}\text{Al}$  reactions *Phys. Rev. C* **94** 065804
- [281] Howard A M, Munch M, Fynbo H O U, Kirsebom O S, Laursen K L, Diget C A and Hubbard N J 2015  $^{23}\text{Na}(\alpha, p)^{26}\text{Mg}$  reaction rate at astrophysically relevant energies *Phys. Rev. Lett.* **115** 052701
- [282] Rauscher T, Thielemann F-K, Görres J and Wiescher M 2000 Capture of  $\alpha$  particles by isospin-symmetric nuclei *Nucl. Phys. A* **675** 695–721
- [283] Hubbard N J *et al* 2021 New experimental  $^{23}\text{Na}(\alpha, p)^{26}\text{Mg}$  reaction rate for massive star and type ia supernova models *Astrophys. J.* **912** 59
- [284] Dillmann I, Heil M, Käppeler F and Plag F K 2006 R und Thielemann. KADoNiS—the karlsruhe astrophysical database of nucleosynthesis in stars *AIP Conf. Proc.* **819** 123
- [285] Weigmann H, Macklin R L and Harvey J A 1976 Isobaric analog impurities from neutron capture and transmission by magnesium *Phys. Rev. C* **14** 1328–35
- [286] Massimi C *et al* 2012 Resonance neutron-capture cross sections of stable magnesium isotopes and their astrophysical implications *Phys. Rev. C* **85** 044615
- [287] Massimi C *et al* 2017 Neutron spectroscopy of  $^{26}\text{Mg}$  states: constraining the stellar neutron source  $^{22}\text{Ne}(\alpha, n)^{25}\text{Mg}$  *Phys. Lett. B* **768** 1–6
- [288] Koning A J, Rochman D, Sublet J-C, Dzysiuk N, Fleming M and van der Marck S 2019 Tendl: complete nuclear data library for innovative nuclear science and technology *Nucl. Data Sheets* **155** 1–55
- [289] Mengoni A, Otsuka T and Ishihara M 1995 Direct radiative capture of p-wave neutrons *Phys. Rev. C* **52** R2334–8
- [290] Reifarh R, Fiebiger S, Göbel K, Heftrich T, Kausch T, Köppchen C, Kurtulgil D, Langer C, Thomas B and Weigand M 2018 Treatment of isomers in nucleosynthesis codes *Int. J. Mod. Phys. A* **33** 1843011
- [291] Coc A, Porquet M-G and Nowacki F 1999 Lifetimes of  $^{26}\text{Al}$  and  $^{34}\text{Cl}$  in an astrophysical plasma *Phys. Rev. C* **61** 015801